

Hierarchical Formulations for Numerical Flow Simulations

by

Essam Moustafa Wahba

B.Sc. (Alexandria University, Egypt) 1997

M.Sc. (Alexandria University, Egypt) 2000

Dissertation

Submitted in partial satisfaction of the requirements for the degree of

Doctor of Philosophy

in

Mechanical and Aeronautical Engineering

in the

Office of Graduate Studies

of the

University of California

Davis

Approved :

Committee in Charge

2004

INFORMATION TO USERS

The quality of this reproduction is dependent upon the quality of the copy submitted. Broken or indistinct print, colored or poor quality illustrations and photographs, print bleed-through, substandard margins, and improper alignment can adversely affect reproduction.

In the unlikely event that the author did not send a complete manuscript and there are missing pages, these will be noted. Also, if unauthorized copyright material had to be removed, a note will indicate the deletion.



UMI Microform 3148511

Copyright 2004 by ProQuest Information and Learning Company.
All rights reserved. This microform edition is protected against
unauthorized copying under Title 17, United States Code.

ProQuest Information and Learning Company
300 North Zeeb Road
P.O. Box 1346
Ann Arbor, MI 48106-1346

ABSTRACT

A new hierarchical formulation for the equations of fluid motion is developed. The hierarchical nature of the new formulation is due to its ability to simulate all levels of fluid flow approximations, namely, inviscid irrotational isentropic flows (potential flow formulation), inviscid rotational non-isentropic flows (Euler formulation) and viscous heat conducting flows (Navier-Stokes formulation). The new formulation uses a potential flow solver as a base solver which is evaluated everywhere in the flow field, while convection/diffusion equations for entropy, vorticity and total enthalpy are only evaluated within limited domains of the flow field where rotational effects are present such as in regions containing shocks, boundary layers and/or wakes. This is accomplished by using a Helmholtz decomposition of the velocity vector into the gradient of a potential function plus a rotational component. The density and pressure are reformulated in terms of the speed and entropy. The new formulation identifies an acoustic mode, governed by the potential equation, from the convection/diffusion mode governing the entropy, vorticity and total enthalpy. This identification of modes together with the ability to restrict the evaluation of entropy, vorticity and total enthalpy to relatively small domains within the flow field offers several advantages over the traditional Euler and Navier-Stokes formulations from the point of view of upwinding, multigrid and the incompressible flow limit. To test the robustness, efficiency and

accuracy of this new approach, several flow problems are simulated. These problems include 2-D shock wave/boundary layer interaction, 2-D inviscid and viscous flows over cylinders, 2-D inviscid and viscous flows over airfoils and 3-D inviscid and viscous flows over wings. The results obtained using the new formulation agree well with both experimental results and numerical results obtained from traditional Euler and Navier-Stokes formulations. Fast convergence rates are also achieved through the implementation of multigrid to the augmented potential equation which results in an order of magnitude reduction in work units as compared to single grid computations.

ACKNOWLEDGEMENTS

I would like to express my deepest gratitude to my advisor Prof. Mohamed Hafez for his continuous support and encouragement throughout my PhD study. His mentoring and guidance throughout the past years is what made this work possible, while his dedication and enthusiasm towards the field of computational fluid dynamics was a great inspiration for me which helped further enhance my appreciation and commitment towards this great field of study.

I would also like to thank Prof. Jean-Jacques Chattot and Prof. Bruce White for their valuable suggestions and comments during the preparation and revision of this dissertation.

Last, but certainly not least, I wish to dedicate this dissertation to my mother and father in recognition of their everlasting support and love. Thanks Mom and Dad !!

TABLE OF CONTENTS

ABSTRACT	ii
ACKNOWLEDGEMENTS	iv
LIST OF FIGURES	xiv
CHAPTER 1 INTRODUCTION	1
1.1 Scope of Aerodynamics	1
1.2 Hierarchy of Fluid Flow Models	4
1.3 History and Development of CFD	8
1.4 Problems with current Euler solvers	10
1.5 Problems with current Navier-Stokes solvers	12
1.6 Boundary Layer Theory and Viscous/Inviscid Interaction	12
1.7 Zonal Formulations	16
1.8 Scope of the Present Work	18
CHAPTER 2 THE HIERARCHICAL FORMULATION	20
2.1 Traditional Euler and Navier-Stokes Formulations	20
2.2 The Hierarchical Formulation	22
2.3 Evaluation of Entropy and Vorticity	25
2.3.1 Potential Flow Regions	26
2.3.2 Inviscid Rotational Flow Regions	27
2.3.3 Viscous Flow Regions	29
2.4 The Incompressible Flow Limit	32
CHAPTER 3 NUMERICAL METHODS	35
3.1 The Finite Volume Method	35
3.2 The Potential Flow Solver	43
3.2.1 Upwinding	43
3.2.2 The Iterative Solver (SLOR)	45
3.3 Convection/Diffusion Equations	45
3.3.1 Upwinding	46
3.3.2 The Iterative Solver (SLOR)	48
3.4 Boundary Conditions	49
3.4.1 Solid Surface Boundary Condition	49
3.4.2 Farfield Boundary Condition	53

CHAPTER 4 FLOW OVER A FLAT PLATE	56
4.1 Incompressible Flow	56
4.1.1 Flow over a Semi-Infinite Flat Plate with and without Suction ..	56
4.1.2 Flow over a Finite Flat Plate: The Trailing-Edge Problem	57
4.2 Compressible Flow	59
4.2.1 Inviscid Flow over a Wedge	62
4.2.2 Shock Wave/Boundary Layer Interaction	62
CHAPTER 5 INVISCID AND VISCOUS FLOWS OVER A CYLINDER	66
5.1 Inviscid Flows Over a Cylinder	67
5.1.1 Incompressible Shear Flow	68
5.1.2 Transonic Flow	70
5.1.3 Supersonic Flow	72
5.2 Viscous Incompressible Flows Over a Cylinder	72
5.2.1 Flow over a stationary cylinder	76
5.2.2 Flow over a rotating cylinder	76
5.2.3 Flow over a cylinder with suction	77
5.2.4 Flow over a rotating cylinder with suction	78
CHAPTER 6 INVISCID AND VISCOUS FLOWS OVER AIRFOILS	88
6.1 Inviscid Flows Over an Airfoil	88
6.2 Viscous Flows Over an Airfoil.....	95
6.2.1 Evaluation of vorticity using first approach	95
6.2.2 Evaluation of vorticity using second approach	97
6.3 The Kutta Condition	106
CHAPTER 7 INVISCID AND VISCOUS FLOWS OVER WINGS	114
7.1 Three Dimensional Farfield Boundary Condition.....	116
7.2 Inviscid Flows Over NACA0012 Wing.....	117
7.3 Viscous Flows Over NACA0012 Wing	117
7.3.1 Evaluation of vorticity using first approach	125
7.3.2 Evaluation of vorticity using second approach	125
CHAPTER 8 MULTIGRID METHODS	133
8.1 The Correction Storage (CS) Scheme.....	134
8.2 The Full Approximation Storage (FAS) Scheme	135
8.3 The Full Multigrid (FMG) Procedure	137
8.4 Multigrid procedure for the Augmented Potential Equation	138
8.5 Inviscid Flows over an airfoil.....	139
8.6 Viscous Flows over an airfoil	139
CHAPTER 9 CONCLUDING REMARKS	152
9.1 Concluding Remarks	152
9.1.1 Domain Decomposition	152

9.1.2	Multigrid	153
9.1.3	Upwinding	154
9.1.4	The Incompressible Flow Limit	154
9.2	Recommendations for Future Work	155
	BIBLIOGRAPHY	156
	VITA	165

LIST OF FIGURES

1.1	Hierarchy of Fluid Flow Models	7
1.2	Direct Method for Viscous/Inviscid Interaction	15
1.3	Semi-Inverse Coupling for Viscous/Inviscid Interaction.....	16
1.4	Zonal Methods	17
2.1	Flow Field Decomposition for Compressible Flows	26
2.2	Entropy Generation in Inviscid and Viscous Flow Regions	27
2.3	Flow Field Decomposition for Incompressible Flows.....	33
3.1	Two-Dimensional Finite Volume Method	36
3.2	Three-Dimensional Finite Volume Method.....	39
3.3	Solid Surface Boundary Condition.....	49
4.1	U-velocity profile for incompressible viscous flow over a semi-infinite flat plate ($Re = 1 \times 10^5$)	58
4.2	U-velocity profile for incompressible viscous flow over a semi-infinite flat plate with suction ($Re = 1 \times 10^5$, $V_s = 0.005$).....	58
4.3	U-velocity contours for incompressible viscous flow over a semi-infinite flat plate ($Re = 1 \times 10^5$)	58
4.4	U-velocity contours for incompressible viscous flow over a semi-infinite flat plate with suction ($Re = 1 \times 10^5$, $V_s = 0.005$).....	58
4.5	Incompressible viscous flow over a finite flat plate ($Re = 1 \times 10^5$)	60
4.6	Shock Wave/Boundary Layer Interaction	61
4.7	Pressure contours for Supersonic Potential Flow over a Wedge ($M_\infty = 2.0$)	64
4.8	Pressure contours for Shock Wave/B.L. Interaction ($M_\infty = 2.0$, $Re_L = 2.96 \times 10^5$)	64
4.9	Surface Pressure for Supersonic Potential Flow over a Wedge ($M_\infty = 2.0$)	64
4.10	Surface Pressure for Shock Wave/B.L. Interaction ($M_\infty = 2.0$, $Re_L = 2.96 \times 10^5$)	64
4.11	Pressure at $y=0.175$ for Supersonic Potential Flow over a Wedge ($M_\infty = 2.0$)	64
4.12	Pressure at $y=0.175$ for Shock Wave/B.L. Interaction ($M_\infty = 2.0$, $Re_L = 2.96 \times 10^5$)	64
4.13	U contours for Shock Wave/B.L. Interaction ($M_\infty = 2.0$, $Re_L = 2.96 \times 10^5$)	65

4.14	Entropy contours for Shock Wave/B.L. Interaction ($M_\infty = 2.0, Re_L = 2.96 \times 10^5$)	65
4.15	Skin friction coefficient for Shock Wave/B.L. Interaction ($M_\infty = 2.0, Re_L = 2.96 \times 10^5$)	65
4.16	U-velocity profiles for Shock Wave/B.L. Interaction ($M_\infty = 2.0, Re_L = 2.96 \times 10^5$)	65
5.1	Streamlines for incompressible inviscid shear flow over a cylinder ($\frac{\omega R}{U_\infty} = 5$)	71
5.2	Wake centerline velocity for incompressible inviscid shear flow over a cylinder ($\frac{\omega R}{U_\infty} = 5$)	71
5.3	Effect of incoming vorticity on the inviscid separation length for incompressible inviscid shear flow over a cylinder	71
5.4	Effect of incoming vorticity on the reattachment angle for incompressible inviscid shear flow over a cylinder	71
5.5	Streamlines for inviscid rotational flow over a cylinder ($M_\infty = 0.5$)	73
5.6	Surface pressure distribution for inviscid flow over a cylinder ($M_\infty = 0.5$) ..	73
5.7	Mach contours for inviscid transonic flow over a cylinder ($M_\infty = 0.5$)..	73
5.8	Mach contours for inviscid supersonic flow over a cylinder ($M_\infty = 2.0$)	74
5.9	Entropy contours for inviscid rotational flow over a cylinder ($M_\infty = 2.0$)	74
5.10	Sonic lines for inviscid rotational flow over a cylinder ($M_\infty=1.7, 2.0$ and 2.3)	74
5.11	Pressure jump across the bow shock at the symmetry line	75
5.12	Standoff distance for the bow shock in front of a circular cylinder	75
5.13	Streamlines for incompressible potential flows over a cylinder with and without rotation and/or suction	80
5.14	Streamlines for incompressible viscous flow over a cylinder at different Reynolds numbers	81
5.15	Effect of Reynolds number on separation length for incompressible viscous flow over a cylinder	82
5.16	Effect of rotation rate on lift coefficient for incompressible viscous flow over a rotating cylinder at $Re=30$	82
5.17	Effect of Reynolds number on lift coefficient for incompressible viscous flow over a rotating cylinder at $\alpha = 6$	82
5.18	Streamlines for incompressible viscous flow over a rotating cylinder at different Reynolds numbers and rotation rates	83
5.19	Pressure contours for incompressible viscous flow over a rotating cylinder at different Reynolds numbers and rotation rates	84
5.20	Streamlines for incompressible viscous flow over a cylinder with suction at different Reynolds numbers and suction rates	85
5.21	Pressure contours for incompressible viscous flow over a cylinder with suction at different Reynolds numbers and suction rates	86
5.22	Incompressible viscous flow over a rotating cylinder with suction ($Re=30, \alpha = 4, V_s = 0.9$)	87

6.1	Structured C-Grid for NACA0012 Airfoil	89
6.2	Inviscid flow over NACA0012 airfoil ($M_\infty = 0.86, \alpha = 0^\circ$)	90
6.3	Surface pressure distribution for inviscid flow over NACA0012 airfoil ($M_\infty = 0.86, \alpha = 0^\circ$)	90
6.4	Inviscid flow over NACA0012 airfoil ($M_\infty = 0.75, \alpha = 2^\circ$)	91
6.5	Surface pressure distribution for inviscid flow over NACA0012 airfoil ($M_\infty = 0.75, \alpha = 2^\circ$)	91
6.6	Inviscid flow over NACA0012 airfoil ($M_\infty = 0.85, \alpha = 1^\circ$)	92
6.7	Surface pressure distribution for inviscid flow over NACA0012 airfoil ($M_\infty = 0.85, \alpha = 1^\circ$)	92
6.8	Inviscid flow over NACA0012 airfoil ($M_\infty = 1.4, \alpha = 0^\circ$)	93
6.9	Surface pressure distribution for inviscid flow over NACA0012 airfoil ($M_\infty = 1.4, \alpha = 0^\circ$)	93
6.10	Inviscid flow over NACA0012 airfoil ($M_\infty = 1.4, \alpha = 4^\circ$)	94
6.11	Surface pressure distribution for inviscid flow over NACA0012 airfoil ($M_\infty = 1.4, \alpha = 4^\circ$)	94
6.12	Viscous flow over NACA0012 airfoil using first approach ($M_\infty = 0.8,$ $Re = 500, \alpha = 0^\circ$)	98
6.13	Surface pressure distribution for viscous flow over NACA0012 airfoil using first approach ($M_\infty = 0.8, Re = 500, \alpha = 0^\circ$)	98
6.14	Viscous flow over NACA0012 airfoil using first approach ($M_\infty = 0.8,$ $Re = 500, \alpha = 10^\circ$)	99
6.15	Surface pressure distribution for viscous flow over NACA0012 airfoil using first approach ($M_\infty = 0.8, Re = 500, \alpha = 10^\circ$)	99
6.16	Viscous flow over NACA0012 airfoil using first approach ($M_\infty = 0.9,$ $Re = 500, \alpha = 0^\circ$)	100
6.17	Surface pressure distribution for viscous flow over NACA0012 airfoil using first approach ($M_\infty = 0.9, Re = 500, \alpha = 0^\circ$)	100
6.18	Viscous flow over NACA0012 airfoil using first approach ($M_\infty = 0.9,$ $Re = 500, \alpha = 10^\circ$)	101
6.19	Surface pressure distribution for viscous flow over NACA0012 airfoil using first approach ($M_\infty = 0.9, Re = 500, \alpha = 10^\circ$)	101
6.20	Mach Contours for viscous flow over NACA0012 airfoil using first ap- proach ($M_\infty = 0.85, Re = 2000, \alpha = 0^\circ$)	102
6.21	Pressure contours for viscous flow over NACA0012 airfoil using first approach ($M_\infty = 0.85, Re = 2000, \alpha = 0^\circ$)	102
6.22	Surface pressure distribution for viscous flow over NACA0012 airfoil using first approach ($M_\infty = 0.85, Re = 2000, \alpha = 0^\circ$)	102
6.23	Mach Contours for viscous flow over NACA0012 airfoil using first ap- proach ($M_\infty = 0.5, Re = 1 \times 10^4, \alpha = 0^\circ$)	103
6.24	Pressure contours for viscous flow over NACA0012 airfoil using first approach ($M_\infty = 0.5, Re = 1 \times 10^4, \alpha = 0^\circ$)	103

6.25	Surface pressure distribution for viscous flow over NACA0012 airfoil using first approach ($M_\infty = 0.5$, $Re = 1 \times 10^4$, $\alpha = 0^\circ$)	103
6.26	Viscous flow over NACA0012 airfoil using first approach ($M_\infty = 1.5$, $Re = 1 \times 10^4$, $\alpha = 0^\circ$)	104
6.27	Surface pressure distribution for viscous flow over NACA0012 airfoil using first approach ($M_\infty = 1.5$, $Re = 1 \times 10^4$, $\alpha = 0^\circ$)	104
6.28	U contours for incompressible viscous flow over NACA0012 airfoil using first approach ($Re = 500$, $\alpha = 10^\circ$)	105
6.29	Surface pressure distribution for viscous flow over NACA0012 airfoil using first approach ($M_\infty = 0.0, 0.1, 0.2$, $Re = 500$, $\alpha = 10^\circ$)	105
6.30	Viscous flow over NACA0012 airfoil using second approach ($M_\infty = 0.8$, $Re = 500$, $\alpha = 0^\circ$)	109
6.31	Skin friction and surface pressure distributions for viscous flow over NACA0012 airfoil ($M_\infty = 0.8$, $Re = 500$, $\alpha = 0^\circ$)	109
6.32	Viscous flow over NACA0012 airfoil using second approach ($M_\infty = 0.8$, $Re = 500$, $\alpha = 10^\circ$)	110
6.33	Skin friction and surface pressure distributions for viscous flow over NACA0012 airfoil ($M_\infty = 0.8$, $Re = 500$, $\alpha = 10^\circ$)	110
6.34	Viscous flow over NACA0012 airfoil using second approach ($M_\infty = 1.5$, $Re = 1 \times 10^4$, $\alpha = 0^\circ$)	111
6.35	Skin friction and surface pressure distributions for viscous flow over NACA0012 airfoil ($M_\infty = 1.5$, $Re = 1 \times 10^4$, $\alpha = 0^\circ$)	111
6.36	Mach contours for viscous flow over NACA0012 airfoil using second approach ($M_\infty = 0.5$, $Re = 1 \times 10^4$, $\alpha = 0^\circ$)	112
6.37	Surface pressure distribution for viscous flow over NACA0012 airfoil ($M_\infty = 0.5$, $Re = 1 \times 10^4$, $\alpha = 0^\circ$)	112
6.38	Pressure contours for viscous flow over NACA0012 airfoil using second approach ($M_\infty = 0.5$, $Re = 1 \times 10^4$, $\alpha = 0^\circ$)	112
6.39	Viscous flow over NACA0012 airfoil using second approach ($M_\infty = 0.9$, $Re = 500$, $\alpha = 10^\circ$)	113
6.40	Surface pressure distributions for viscous flow over NACA0012 airfoil ($M_\infty = 0.9$, $Re = 500$, $\alpha = 10^\circ$)	113
7.1	Structured C-H Grid for NACA0012 Wing	115
7.2	Surface pressure distribution for subsonic flow over an elliptic wing ($M_\infty = 0.3$, $\alpha = 2^\circ$)	118
7.3	Local lift coefficient distribution for subsonic flow over an elliptic wing ($M_\infty = 0.3$, $\alpha = 2^\circ$)	118
7.4	Pressure contours on upper surface of elliptic wing ($M_\infty = 0.3$, $\alpha = 2^\circ$)	119
7.5	Pressure contours on lower surface of elliptic wing ($M_\infty = 0.3$, $\alpha = 2^\circ$)	119
7.6	Surface pressure distributions for inviscid flow over NACA0012 wing ($M_\infty = 0.3$, $\alpha = 2^\circ$)	120
7.7	Pressure contours on upper surface of NACA0012 wing ($M_\infty = 0.3$, $\alpha = 2^\circ$)	121

7.8	Pressure contours on lower surface of NACA0012 wing ($M_{\infty} = 0.3$, $\alpha = 2^\circ$)	121
7.9	Surface pressure distributions for inviscid flow over NACA0012 wing ($M_{\infty} = 0.84$, $\alpha = 3^\circ$).....	122
7.10	Pressure contours on upper surface of NACA0012 wing ($M_{\infty} = 0.84$, $\alpha = 3^\circ$, Potential Flow)	123
7.11	Pressure contours on lower surface of NACA0012 wing ($M_{\infty} = 0.84$, $\alpha = 3^\circ$, Potential Flow)	123
7.12	Pressure contours on upper surface of NACA0012 wing ($M_{\infty} = 0.84$, $\alpha = 3^\circ$, Inviscid Rotational Flow)	124
7.13	Pressure contours on lower surface of NACA0012 wing ($M_{\infty} = 0.84$, $\alpha = 3^\circ$, Inviscid Rotational Flow)	124
7.14	Surface pressure distributions for potential flow over NACA0012 Wing ($M_{\infty} = 0.9$, $\alpha = 1^\circ$)	126
7.15	Pressure contours on upper surface of NACA0012 wing ($M_{\infty} = 0.9$, $\alpha = 1^\circ$, Potential Flow)	127
7.16	Pressure contours on lower surface of NACA0012 wing ($M_{\infty} = 0.9$, $\alpha = 1^\circ$, Potential Flow)	127
7.17	Surface pressure distributions for viscous flow over NACA 0012 wing using first approach ($M_{\infty} = 0.9$, Re=1000, $\alpha = 1^\circ$).....	128
7.18	Pressure contours on upper surface of NACA0012 wing using first approach ($M_{\infty} = 0.9$, Re=1000, $\alpha = 1^\circ$)	129
7.19	Pressure contours on lower surface of NACA0012 wing using first approach ($M_{\infty} = 0.9$, Re=1000, $\alpha = 1^\circ$)	129
7.20	Comparison of surface pressure distributions for viscous flow over NACA0012 wing using the first and second approaches ($M_{\infty} = 0.9$, Re=1000, $\alpha = 1^\circ$)	130
7.21	Pressure contours on upper surface of NACA0012 wing using second approach ($M_{\infty} = 0.9$, Re=1000, $\alpha = 1^\circ$)	131
7.22	Pressure contours on lower surface of NACA0012 wing using second approach ($M_{\infty} = 0.9$, Re=1000, $\alpha = 1^\circ$)	131
7.23	Mach contours at symmetry plane for potential flow over NACA0012 wing ($M_{\infty} = 0.9$, $\alpha = 1^\circ$)	132
7.24	Mach contours at symmetry plane for viscous flow over NACA0012 wing using first approach ($M_{\infty} = 0.9$, Re=1000, $\alpha = 1^\circ$)	132
7.25	Mach contours at symmetry plane for viscous flow over NACA0012 wing using second approach ($M_{\infty} = 0.9$, Re=1000, $\alpha = 1^\circ$)	132
8.1	Structure of Multigrid Cycles	136
8.2	Full Multigrid Procedure.....	137
8.3	Mach contours for potential flow over NACA0012 airfoil ($M_{\infty} = 0.86$, $\alpha = 0^\circ$)	140
8.4	Mach contours for inviscid rotational flow over NACA0012 airfoil ($M_{\infty} = 0.86$, $\alpha = 0^\circ$)	140

8.5	Convergence history for potential flow over NACA0012 airfoil ($M_\infty = 0.86, \alpha = 0^\circ$)	140
8.6	Convergence history for inviscid rotational flow over NACA0012 airfoil ($M_\infty = 0.86, \alpha = 0^\circ$).....	140
8.7	Mach contours for potential flow over NACA0012 airfoil ($M_\infty = 1.5, \alpha = 0^\circ$).....	141
8.8	Mach contours for inviscid rotational flow over NACA0012 airfoil ($M_\infty = 1.5, \alpha = 0^\circ$).....	141
8.9	Convergence history for potential flow over NACA0012 airfoil ($M_\infty = 1.5, \alpha = 0^\circ$).....	141
8.10	Convergence history for inviscid rotational flow over NACA0012 airfoil ($M_\infty = 1.5, \alpha = 0^\circ$).....	141
8.11	Mach contours for viscous flow over NACA0012 airfoil ($M_\infty = 1.5, Re = 1 \times 10^4, \alpha = 0^\circ$): Coupling potential flow with viscous layer	142
8.12	Mach contours for viscous flow over NACA0012 airfoil ($M_\infty = 1.5, Re = 1 \times 10^4, \alpha = 0^\circ$): Coupling rotational flow with viscous layer ...	142
8.13	Convergence history for viscous flow over NACA0012 airfoil ($M_\infty = 1.5, Re = 1 \times 10^4, \alpha = 0^\circ$): Coupling potential flow with viscous layer	142
8.14	Convergence history for viscous flow over NACA0012 airfoil ($M_\infty = 1.5, Re = 1 \times 10^4, \alpha = 0^\circ$): Coupling rotational flow with viscous layer	142
8.15	Mach contours for potential flow over NACA0012 airfoil ($M_\infty = 0.1, \alpha = 0^\circ$).....	144
8.16	Mach contours for viscous flow over NACA0012 airfoil ($M_\infty = 0.1, Re = 500, \alpha = 0^\circ$)	144
8.17	Convergence history for potential flow over NACA0012 airfoil ($M_\infty = 0.1, \alpha = 0^\circ$).....	144
8.18	Convergence history for viscous flow over NACA0012 airfoil ($M_\infty = 0.1, Re = 500, \alpha = 0^\circ$)	144
8.19	Mach contours for potential flow over NACA0012 airfoil ($M_\infty = 0.1, \alpha = 10^\circ$).....	145
8.20	Mach contours for viscous flow over NACA0012 airfoil ($M_\infty = 0.1, Re = 500, \alpha = 10^\circ$)	145
8.21	Convergence history for potential flow over NACA0012 airfoil ($M_\infty = 0.1, \alpha = 10^\circ$)	145
8.22	Convergence history for viscous flow over NACA0012 airfoil ($M_\infty = 0.1, Re = 500, \alpha = 10^\circ$)	145
8.23	Mach contours for potential flow over NACA0012 airfoil ($M_\infty = 0.8, \alpha = 0^\circ$).....	146
8.24	Mach contours for viscous flow over NACA0012 airfoil ($M_\infty = 0.8, Re = 500, \alpha = 0^\circ$)	146
8.25	Convergence history for potential flow over NACA0012 airfoil ($M_\infty = 0.8, \alpha = 0^\circ$).....	146

8.26 Convergence history for viscous flow over NACA0012 airfoil ($M_\infty = 0.8$, $Re = 500$, $\alpha = 0^\circ$)	146
8.27 Mach contours for potential flow over NACA0012 airfoil ($M_\infty = 0.8$, $\alpha = 10^\circ$)	147
8.28 Mach contours for viscous flow over NACA0012 airfoil ($M_\infty = 0.8$, $Re = 500$, $\alpha = 10^\circ$)	147
8.29 Convergence history for potential flow over NACA0012 airfoil ($M_\infty = 0.8$, $\alpha = 10^\circ$)	147
8.30 Convergence history for viscous flow over NACA0012 airfoil ($M_\infty = 0.8$, $Re = 500$, $\alpha = 10^\circ$)	147
8.31 Mach contours for potential flow over NACA0012 airfoil ($M_\infty = 0.9$, $\alpha = 0^\circ$)	148
8.32 Mach contours for viscous flow over NACA0012 airfoil ($M_\infty = 0.9$, $Re = 500$, $\alpha = 0^\circ$)	148
8.33 Convergence history for potential flow over NACA0012 airfoil ($M_\infty = 0.9$, $\alpha = 0^\circ$)	148
8.34 Convergence history for viscous flow over NACA0012 airfoil ($M_\infty = 0.9$, $Re = 500$, $\alpha = 0^\circ$)	148
8.35 Mach contours for potential flow over NACA0012 airfoil ($M_\infty = 0.9$, $\alpha = 10^\circ$)	149
8.36 Mach contours for viscous flow over NACA0012 airfoil ($M_\infty = 0.9$, $Re = 500$, $\alpha = 10^\circ$)	149
8.37 Convergence history for potential flow over NACA0012 airfoil ($M_\infty = 0.9$, $\alpha = 10^\circ$)	149
8.38 Convergence history for viscous flow over NACA0012 airfoil ($M_\infty = 0.9$, $Re = 500$, $\alpha = 10^\circ$)	149
8.39 Mach contours for potential flow over NACA0012 airfoil ($M_\infty = 0.85$, $\alpha = 0^\circ$)	150
8.40 Mach contours for viscous flow over NACA0012 airfoil ($M_\infty = 0.85$, $Re = 2000$, $\alpha = 0^\circ$)	150
8.41 Convergence history for potential flow over NACA0012 airfoil ($M_\infty = 0.85$, $\alpha = 0^\circ$)	150
8.42 Convergence history for viscous flow over NACA0012 airfoil ($M_\infty = 0.85$, $Re = 2000$, $\alpha = 0^\circ$)	150
8.43 Mach contours for potential flow over NACA0012 airfoil ($M_\infty = 0.5$, $\alpha = 0^\circ$)	151
8.44 Mach contours for viscous flow over NACA0012 airfoil ($M_\infty = 0.5$, $Re = 1 \times 10^4$, $\alpha = 0^\circ$)	151
8.45 Convergence history for potential flow over NACA0012 airfoil ($M_\infty = 0.5$, $\alpha = 0^\circ$)	151
8.46 Convergence history for viscous flow over NACA0012 airfoil ($M_\infty = 0.5$, $Re = 1 \times 10^4$, $\alpha = 0^\circ$)	151

CHAPTER 1

INTRODUCTION

1.1 Scope of Aerodynamics

Aerodynamics is the branch of Fluid Mechanics concerned with the study of external flows over bodies of aeronautical interest such as airfoils and wings. In the study of Aerodynamics, gravity forces are usually neglected and, for high Reynolds number flows, the viscous effects are confined to very thin regions near solid surfaces called boundary layers.

One of the most important parameters in the study of aerodynamics, besides the Reynolds number, is the Mach number. The Mach number represents a measure of the compressibility effects on the flow field. For low Mach number flows (Mach number < 0.3), compressibility effects are negligible and the subject is known as Incompressible Aerodynamics. For higher Mach number flows, compressibility effects become important. As the Mach number goes even higher and starts approaching the sonic limit, the flow enters the transonic regime. Transonic flows are very difficult to study due to the mixed elliptic-hyperbolic nature of the flow, where the flow behavior is elliptic in subsonic regions and hyperbolic in supersonic regions. Shock

waves appear in transonic flows, separating the supersonic regions from the subsonic ones. The appearance of shock waves is undesirable in aerodynamic flows as it results in the generation of wave drag. Shock waves may also cause boundary layer separation which results in loss of lift and further rise in drag. Linearized theory provides good results for purely subsonic and purely supersonic flows. However, the linearized theory fails for transonic flows and more advanced tools must be developed for the analysis of such flows.

Accurate prediction of lift and drag at on and off design conditions is the main objective in the study of aerodynamics. The Kutta-Joukowski theorem provides an accurate prediction of lift based on inviscid flow theory. The theorem relates the lift per unit width to the circulation (Γ) according to the following equation

$$\frac{L}{b} = -\rho_\infty U_\infty \Gamma \quad (1.1)$$

The remaining problem is to determine the circulation (Γ) as a function of the airfoil shape and the angle of attack (α). However, even if the airfoil shape and the angle of attack (α) are given, an infinite number of solutions can be found corresponding to different values of (Γ). The Kutta condition fixed this nonuniqueness problem by identifying the physically proper value of circulation (Γ_{Kutta}) such that the flow leaves the trailing edge smoothly. Hence, for airfoils with sharp trailing edges, the Kutta condition implies that the trailing edge is a stagnation point. Based on this inviscid flow theory, accurate predictions of lift are possible as long as the bound-

ary layer is attached, however, in the case of boundary layer separation and stall, the inviscid approximation is no longer valid and more advanced tools are needed to provide accurate lift predictions in these cases.

Although inviscid flow theory provides a prediction for lift, however, it fails in predicting the drag resulting in D'Alembert's paradox which states that the drag of any closed body immersed in an incompressible uniform stream is identically zero. D'Alembert's paradox was finally solved when Prandtl introduced the boundary layer theory where he pointed out the profound effect of boundary layer on the flow field.

Three dimensional effects for wings of finite span were successfully modelled by the lifting line theory introduced also by Prandtl. Lifting line theory replaces the wing by a single lifting line and a continuous sheet of semi-infinite trailing vortices. Hence, a downwash velocity is induced at each point along the lifting line due to the trailing vortices. Downwash effectively reduces the angle of attack at each two-dimensional section across the wing. In the absence of boundary layer separation and stall, lifting line theory provides good predictions for lift and induced drag for the case of high aspect ratio unswept wings where the assumption of the flow near the wing being two-dimensional at each cross-section is a good approximation.

From the above discussion, it is clear that there is still need to develop more advanced tools for aerodynamic analysis of transonic flows, and for the accurate prediction of lift and drag at off design conditions in the presence of boundary layer separation and stall. In order to achieve that, considering more general fluid flow models than the inviscid flow theory is a necessity. A discussion of the available fluid

flow models is the subject of the next section.

1.2 Hierarchy of Fluid Flow Models

The Navier-Stokes equations are the governing equations for fluid mechanics representing conservation of mass, momentum and energy. For steady flows, the Navier-Stokes equations, using standard notations, are

$$\nabla \cdot \rho \vec{q} = 0 \quad (1.2)$$

$$\nabla \cdot (\rho \vec{q} \otimes \vec{q}) = -\nabla P + \frac{1}{Re} \nabla \cdot \bar{\tau} \quad (1.3)$$

$$\nabla \cdot \rho \vec{q} H = \frac{1}{Re Pr} \nabla \cdot k \nabla T + \frac{1}{Re} \nabla \cdot \bar{\tau} \cdot \vec{q} \quad (1.4)$$

For a Newtonian fluid, the stress ($\bar{\tau}$) is linearly related to the rate of strain

$$\tau_{ij} = \mu \left(\frac{\partial u_i}{\partial x_j} + \frac{\partial u_j}{\partial x_i} \right) + \lambda \delta_{ij} \frac{\partial u_k}{\partial x_k} \quad (1.5)$$

where ($\lambda = -\frac{2}{3}\mu$) under Stoke's hypothesis. This is a set of nonlinear second order partial differential equations. An equation of state is needed to close the system of equations. Navier-Stokes equations are extremely difficult to solve analytically. However, fortunately, for many flow problems, the full set of Navier-Stokes equations is not needed and certain simplifying assumptions can be introduced. One of the most common simplifying assumptions used frequently in aerodynamics is to neglect the effects of viscosity and heat conduction assuming the flow to be inviscid and adiabatic.

This reduces the Navier-Stokes equations to the simpler set of Euler equations.

$$\nabla \cdot \rho \vec{q} = 0 \quad (1.6)$$

$$\nabla \cdot (\rho \vec{q} \otimes \vec{q}) = -\nabla P \quad (1.7)$$

$$\nabla \cdot \rho \vec{q} H = 0 \quad (1.8)$$

This is a set of nonlinear first order partial differential equations. For smooth flows, Euler equations indicate that entropy and total enthalpy are constant along streamlines

$$S_s = 0 \quad (1.9)$$

$$H_s = 0 \quad (1.10)$$

while vorticity is related to the gradients of entropy and total enthalpy through Crocco's relation

$$\vec{\omega} \times \vec{q} = T \nabla S - \nabla H \quad (1.11)$$

Another common approximation in the field of aerodynamics is to assume the flow to be isentropic and isoenergetic. Under these assumptions, the velocity vector can be expressed as the gradient of a scalar potential function and the Euler equations reduce to the full potential equation. Potential flow is only governed by a single variable, the

potential function. The potential function is the solution of a single nonlinear second order partial differential equation,

$$\nabla \cdot \rho \nabla \phi = 0 \quad (1.12)$$

where

$$\rho = \left[1 - \frac{\gamma - 1}{2} M_\infty^2 (|\nabla \phi|^2 - 1) \right]^{\frac{1}{\gamma-1}} \quad (1.13)$$

thereby greatly simplifying the problem as opposed to solving the Navier-Stokes equations. For incompressible flows, the density is constant, eliminating the non-linearity in the potential equation, and the potential function is now governed by Laplace equation

$$\nabla^2 \phi = 0 \quad (1.14)$$

Analytical solutions for Laplace equation are well developed and the powerful principle of superposition can be applied to this linear equation providing analytical solutions for incompressible potential flows over cylinders, airfoils,...etc.

Moreover, the compressible nonlinear potential equation can be further simplified under the small disturbance approximation resulting in the Transonic Small Disturbance (TSD) equation in the perturbation potential φ .

$$[(1 - M_\infty^2) - (\gamma + 1)M_\infty^2 \varphi_{xx}] \varphi_{xx} + \varphi_{yy} + \varphi_{zz} = 0 \quad (1.15)$$

For purely subsonic or purely supersonic flows, the magnitude of $(\gamma + 1)M_\infty^2 \varphi_x$ is small in comparison with the magnitude of $(1 - M_\infty^2)$ and eqn(1.15) reduces to the linear Prandtl-Glauert equation which is the basic equation used in linearized aerodynamic theory.

$$(1 - M_\infty^2)\varphi_{xx} + \varphi_{yy} + \varphi_{zz} = 0 \quad (1.16)$$

Note that the Prandtl-Glauert equation is not valid for transonic flows because the magnitude of $(1 - M_\infty^2)$ is no longer large in comparison with the magnitude of $(\gamma + 1)M_\infty^2 \varphi_x$ together with the fact that the transonic regime is characterized by its nonlinear mixed elliptic-hyperbolic type behavior which is lost in the linearized Prandtl-Glauert equation. Therefore, it is clear that linearized theory breaks down for transonic flows.

A flowchart showing the hierarchy of the discussed fluid flow models is shown in fig (1.1).

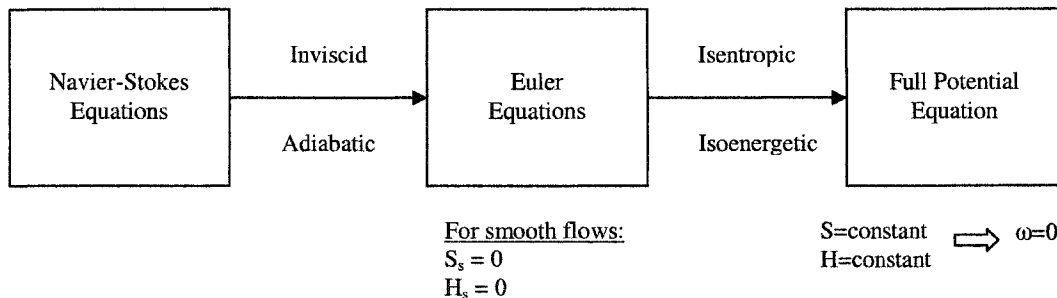


Figure 1.1: Hierarchy of Fluid Flow Models

1.3 History and Development of CFD

For several centuries, experimental and theoretical methods remained the only available methods for the analysis of problems in fluid mechanics. However, over the past fifty years and with the advent of the high speed digital computer, a third powerful approach to the analysis of problems in fluid mechanics emerged, namely, the approach of Computational Fluid Dynamics (CFD). In this computational approach, advanced numerical methods are used to solve the governing equations of fluid flow.

During the last three decades, many promising CFD codes have been developed. In 1971, Murman and Cole [1] introduced a type-dependent discretization scheme to solve the transonic small disturbance equation. Later, Murman [2] introduced a conservative scheme to correctly capture embedded and bow shocks. Moreover, Engquist and Osher [3] constructed a scheme satisfying a generalized entropy condition on the discrete level. Extensions to the solution of the full potential equation, for two and three-dimensional flows, followed by Jameson and Caughey [4]-[7]. Artificial compressibility methods for the solution of the full potential equation were used by Hafez et al [8], [9]. Corrections to the potential flow formulation due to the generation of entropy and vorticity by shock waves were introduced by Hafez and Lovell [10], [11]. For a comprehensive review of these developments, see Hirsch [12] and Holst [13]. The type dependent discretization schemes and relaxation procedures introduced for the solution of the potential equation had some advantages in terms of accuracy and efficiency compared to the solution of Euler equations at that time, where the unsteady hyperbolic equations with artificial viscosity terms added everywhere in the

field, were solved explicitly to reach a steady state solution.

During the eighties there were intensive efforts to improve the solution procedures of Euler equations, as a prerequisite to the solution of Navier-Stokes equations for high Reynolds Number flows. Implicit schemes introduced by Beam and Warming [14], MacCormack [15] and Lerat [16] improved the efficiency of calculations. Local time stepping, residual smoothing and multigrid as well as preconditioning techniques and GMRES [17] are used for convergence acceleration. Fourth order dissipation was introduced early by Kreiss [18] for the solution of hyperbolic equations with smooth solutions. Blending second and fourth order dissipation terms of a finite volume formulation was introduced by MacCormack and used also by Jameson, Schmidt and Turkel [19] with the method of lines based on a multistage Runge-Kutta time integration method. The use of limiters and TVD schemes enhanced the calculations further. On the other hand, flux vector splitting schemes were introduced by Steger and Warming [20] and later by van Leer [21]. Godunov type schemes [22] based on the exact and approximate solutions of the exact and approximate Riemann problems were developed by van Leer [23], Roe [24] and Osher [25]. Later, high resolution schemes and essentially non-oscillatory schemes were introduced by Harten [26] and others. For more details, see Hirsch [12]. The recent multidimensional upwinding and fluctuations splitting schemes are also promising [27].

Both block structured and unstructured grids were used in flow simulations based on Euler equations over complex geometries. Recently, finite element methods became competitive to finite volume methods [28]. The first transonic flow simulation

over a complete airplane was accomplished by Glowinski based on a control theory formulation of potential flow. For more details, see [29] and [30].

Most of the Euler schemes discussed here, have been used for the solution of Navier-Stokes equations, starting with the Lax-Wendroff scheme [31], MacCormack explicit [32] and implicit schemes, including the bidiagonal scheme, the line relaxation [33] and the recent symmetric schemes, Jameson's method of lines with scalar and matrix dissipation, Beam and Warming ADI scheme [34] and Lerat implicit schemes, as well as, upwind schemes, in particular Roe flux difference splitting for the discretization of the convection terms [35]. Similarly, finite elements have been used for the simulation of high Reynolds number viscous flows with structured grids in the boundary layers and the wakes and unstructured grids in the inviscid flow regions. Potential, Euler and Navier-Stokes codes have been successfully used in industry. Nevertheless, there is still need for more developments as described by a recent paper by Johnson [36].

1.4 Problems with current Euler solvers

Current Euler solvers reached a high level of maturity in terms of their development and implementation. However, there is still need for improvement concerning certain problems associated with these solvers. One of these problems is that Euler solvers don't guarantee the existence of a velocity potential function at the discrete level in the case of isentropic irrotational flows. This, in turn, implies that artificial entropy and vorticity are generated in the flow field, especially in the far field where

truncation errors are most significant due to the stretching of the elements. Special Euler schemes that produce a potential solution, if the latter exists, were recently developed by Roe and Rad [37], however, these schemes are obviously more expensive than solving the potential equation.

Another problem for Euler solvers is the introduction of artificial viscosity for the stability of the computations either explicitly or implicitly through upwind schemes, even in subsonic flow regions. This introduction of artificial viscosity everywhere in the flow field affects the accuracy of the computations.

A third problem is stagnation points and the incompressible flow limit. Euler solvers normally suffer from accuracy and slow convergence rate problems in these regions. The accuracy problem is a result of the excessive dissipation encountered at stagnation points which appears in the form of spurious entropy generation, which in turn leads to the contamination of the numerical solution in these regions. Slow convergence rates are due to the large disparity in the eigenvalues of the system at stagnation points which results in an ill-conditioned system of equations. Preconditioning techniques help in reducing these problems [38], [39]. However, preconditioned Euler solvers usually suffer from robustness problems at stagnation points due to the non-normality of the eigenvectors in these regions [40].

It is worth noting that the previously mentioned problems for Euler solvers are not encountered in potential flow solvers which indicates the need to use potential flow solvers as a basic building block towards a more robust and accurate Euler solver.

1.5 Problems with current Navier-Stokes solvers

One of the problems with current Navier-Stokes solvers is the stiffness problem caused by the no-slip boundary condition. This boundary condition results in flow velocities near the walls that are very small in comparison with the acoustic wave speed. This leads to a stiff system of equations which results in slow convergence rates.

For high Reynolds number flows, an extremely fine grid is required near solid surfaces and in wakes to accurately resolve the viscous effects within these regions. For three-dimensional simulations, this results in a nonlinear system of algebraic equations consisting of millions of unknowns which, even with today's high-speed digital computing power, requires extremely extensive memory requirements and CPU time. To avoid this problem, many different approaches have been considered such as viscous/inviscid interaction, fortified Navier-Stokes and zonal formulations. All these approaches try to minimize the memory requirements and CPU time needed for viscous flow simulations.

1.6 Boundary Layer Theory and Viscous/Inviscid Interaction

In 1904, Ludwig Prandtl published, arguably, the most important paper ever written in Fluid Mechanics in which he introduced the concept of the boundary layer, thus making viscous flow calculations possible. Prandtl proposed that for high Reynolds number flows, the viscous effects are confined to a thin boundary layer near the solid surface, while the rest of the flow is basically inviscid. Based on these

assumptions, Prandtl simplified the Navier-Stokes equations to obtain the boundary layer equations. A detailed discussion of the basic assumptions for boundary layer theory and the derivation of the boundary layer equations can be found in [41]. For a flat plate aligned with the x-axis, the boundary layer equations are

$$(\rho u)_x + (\rho v)_y = 0 \quad (1.17)$$

$$\rho uu_x + \rho vu_y = -P_x + \frac{1}{Re}(\mu u_y)_y \quad (1.18)$$

$$P_y = 0 \quad (1.19)$$

$$\rho u H_x + \rho v H_y = \frac{1}{RePr}(kT_y)_y + \frac{1}{Re}(\mu uu_y)_y \quad (1.20)$$

A similarity solution was obtained for the incompressible boundary layer equations by Blasius. Numerical solutions for the compressible boundary layer equations are much more easier than numerical solutions for the Navier-Stokes equations due to the parabolic nature of the boundary layer equations which allows marching the numerical solution in the x-direction, provided the flow is attached.

The first attempt at viscous/inviscid interaction was proposed by Prandtl, coupling potential flows with boundary layers. The inviscid flow calculation over the body provides the pressure and velocities at the edge of the boundary layer. The boundary layer equations are then solved using the inviscid pressure and velocities at the edge of the boundary layer as boundary conditions. The viscous flow calculation provides the displacement thickness (δ^*). The inviscid calculation is then repeated

once again over the body augmented with (δ^*) . The viscous/inviscid interaction continues until overall convergence is achieved. However, many problems are encountered with this procedure. One of the problems is the need to generate a new grid for the augmented body each time an inviscid calculation is performed. Following Lighthill [42], this problem can be avoided by using a normal velocity at the solid surface as a boundary condition for the inviscid flow calculation to account for the displacement effects. The normal velocity is obtained from

$$v_o = \frac{1}{\rho_o} \frac{d}{dx} (\rho_e u_e \delta^*) \quad (1.21)$$

A schematic representation summarizing the viscous/inviscid interaction procedure is shown in fig (1.2). For attached flows, the above mentioned viscous/inviscid interaction method works fairly well. However, for separated flows, the procedure breaks down due to a singularity at the separation point. Goldstein [43] presented an in-depth discussion on the breakdown of the boundary layer equations at separation and since then the singularity problem of the boundary layer equations at separation is referred to as the Goldstein singularity. Better coupling procedures were introduced to solve this problem, such as the inverse and semi-inverse methods.

The inverse method was introduced by Catherall and Mangler [44] where the boundary layer is solved with a prescribed displacement thickness. An early success of this method was obtained by Carter [45] when he computed the separated flow past an indented plate. However, convergence of the inverse method is very slow and

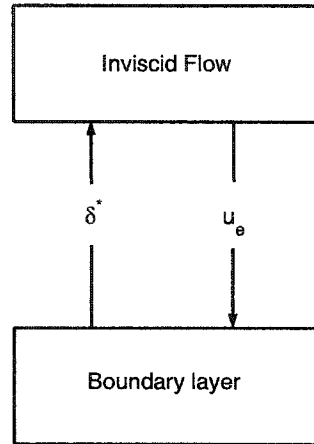


Figure 1.2: Direct Method for Viscous/Inviscid Interaction

defining the inverse formulation for the inviscid flow is a main problem for this method.

A more successful method was the semi-inverse method introduced by LeBalleur [46], [47] and Carter [48] in which the boundary-layer equations are solved in an inverse method with a prescribed displacement thickness, while the inviscid flow is solved in a direct method with the same prescribed displacement thickness. Under-relaxation is required for convergence which is a main disadvantage, in general, for viscous/inviscid interaction methods. A schematic representation for the semi-inverse method is shown in fig (1.3).

Other coupling procedures also exist, such as the quasi-simultaneous method introduced by Veldman [49], [50]. In this procedure, a simple approximation of the inviscid flow, termed the interaction law, is solved simultaneously with the boundary layer equations. The error introduced by using the interaction law as an approximation of the inviscid flow is then handled iteratively.

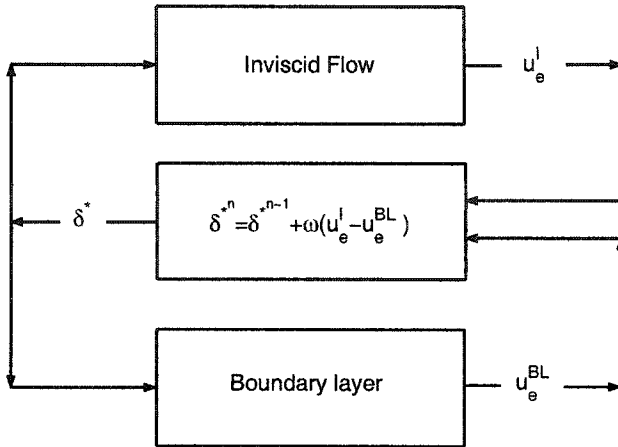


Figure 1.3: Semi-Inverse Coupling for Viscous/Inviscid Interaction

Extensions of viscous-inviscid interaction methods to three-dimensional flows over wings are not straightforward, in particular at the tips and wing-body junctions where the flow is truly three-dimensional and the boundary layer approximation is no longer valid.

1.7 Zonal Formulations

To avoid the problems associated with viscous/inviscid interaction methods, zonal methods were proposed. Unlike viscous/inviscid interaction methods, zonal methods decompose the domain into an inviscid region and a viscous region. However, to avoid the limitations of the boundary layer equations, zonal methods normally use Navier-Stokes equations in the viscous region and either Euler equations or the full potential equation in the inviscid region. The interaction between the inviscid and viscous zones is normally done through an overlapping zone as shown in fig (1.4).

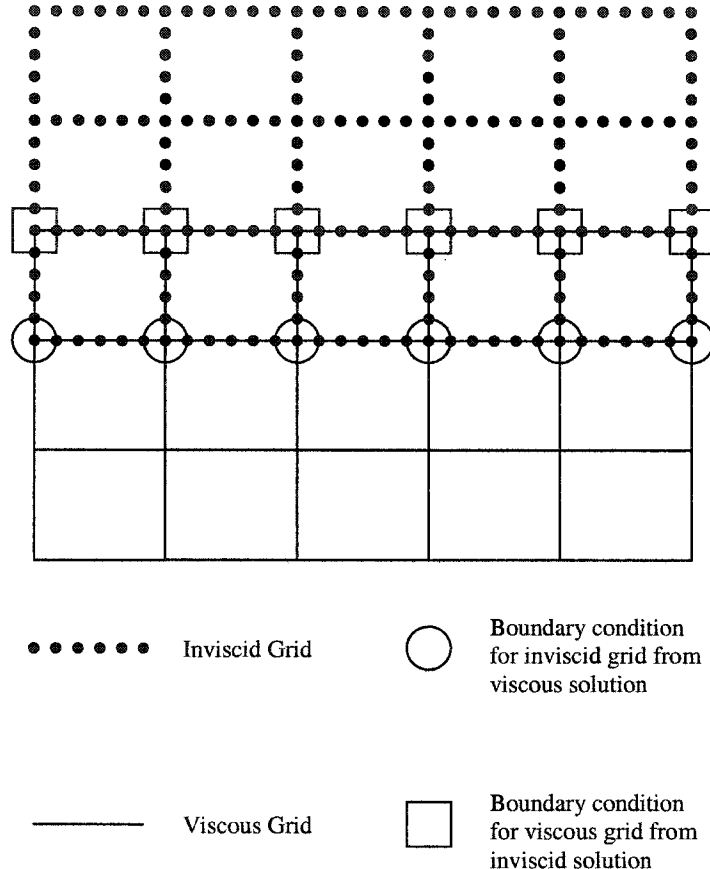


Figure 1.4: Zonal Methods

The robustness of any zonal formulation is entirely dependent on this overlapping region and how the boundary conditions are implemented for the inviscid and viscous flows within this region. Zonal methods were successfully applied to two and three dimensional aerodynamic applications [52]-[56], however, convergence difficulties are usually encountered due to the reflection of the error from the artificial boundary conditions used in patching the different zones [57], [58].

It is worth noting that Navier-Stokes equations are, in fact, not needed everywhere

in the viscous layers. An interesting approach proposed by Van Dalsem and Steger [51] uses the boundary layer solutions for attached flow regions in their method of fortified equations where the Navier-Stokes equations are augmented with a forcing function, $\chi(U_{BL} - U)$. The switching parameter χ is assigned a large value in the regions where the boundary layer solution, U_{BL} , is valid, otherwise it is set to a small value.

1.8 Scope of the Present Work

Traditional Euler and Navier-Stokes solvers are well developed and have been applied very effectively to the study of various aeronautical problems. However, as can be seen from the previous sections, there is still need for improvement regarding certain areas such as domain decomposition, the incompressible flow limit, upwinding, the far field behavior and multigrid.

The present work aims at developing a new approach that is specifically tailored to address these areas. To achieve this, the new approach introduces a potential function ϕ , a rotational velocity component \vec{q}^* , the entropy S and the total enthalpy H as the new dependent variables for the governing equations. The objective of the change of variables is clear, as by introducing the potential function ϕ as one of the new dependent variables, the new formulation naturally reduces to potential flow in the far field governed by the single variable ϕ . Hence, the formulation leads to an efficient implementation of domain decomposition methods where the problems associated with artificial interfaces and artificial boundary conditions are minimized when

compared to standard zonal methods. Also, there is no need for any coupling algorithms or boundary layer approximations as in viscous/inviscid interaction methods. The introduction of the potential function also identifies an acoustic mode governed by the potential equation from the convection/diffusion mode governing the rest of the dependent variables. This identification of modes allows efficient implementation of convergence acceleration methods and upwinding as the acoustic mode is well suited to multigrid methods and the scalar convection/diffusion equations are well suited to multidimensional upwind schemes. Moreover, the introduction of entropy as a dependent variable helps in controlling the spurious entropy generation encountered at stagnation points and in the far field which is a main concern in Euler solvers.

In the next chapters, the basic concepts of the present hierarchical formulation are introduced followed by the numerical methods used in its implementation. The formulation is then used to simulate several inviscid and viscous flow problems in order to assess the merits of the new approach. Multigrid techniques are then implemented and they result in an order of magnitude reduction in computational work. Finally, concluding remarks and recommendations for future work are presented.

CHAPTER 2

THE HIERARCHICAL FORMULATION

2.1 Traditional Euler and Navier-Stokes Formulations

The traditional formulation for the Navier-Stokes equations can be expressed in the following compact vector form

$$\frac{\partial \mathbf{U}}{\partial t} + \frac{\partial \mathbf{E}}{\partial x} + \frac{\partial \mathbf{F}}{\partial y} + \frac{\partial \mathbf{G}}{\partial z} = 0 \quad (2.1)$$

where the vectors $\mathbf{U}, \mathbf{E}, \mathbf{F}, \mathbf{G}$ are defined as follows

$$\mathbf{U} = \begin{pmatrix} \rho \\ \rho u \\ \rho v \\ \rho w \\ \rho \epsilon \end{pmatrix}$$

$$\mathbf{E} = \begin{pmatrix} \rho u \\ \rho u^2 + P - \frac{1}{Re}\tau_{xx} \\ \rho uv - \frac{1}{Re}\tau_{xy} \\ \rho uw - \frac{1}{Re}\tau_{xz} \\ \rho uH - \frac{1}{Re}u\tau_{xx} - \frac{1}{Re}v\tau_{xy} - \frac{1}{Re}w\tau_{xz} - \frac{1}{RePr}k\frac{\partial T}{\partial x} \end{pmatrix}$$

$$\mathbf{F} = \begin{pmatrix} \rho v \\ \rho uv - \frac{1}{Re}\tau_{xy} \\ \rho v^2 + P - \frac{1}{Re}\tau_{yy} \\ \rho vw - \frac{1}{Re}\tau_{yz} \\ \rho vH - \frac{1}{Re}u\tau_{xy} - \frac{1}{Re}v\tau_{yy} - \frac{1}{Re}w\tau_{yz} - \frac{1}{RePr}k\frac{\partial T}{\partial y} \end{pmatrix}$$

$$\mathbf{G} = \begin{pmatrix} \rho w \\ \rho uw - \frac{1}{Re}\tau_{xz} \\ \rho vw - \frac{1}{Re}\tau_{yz} \\ \rho w^2 + P - \frac{1}{Re}\tau_{zz} \\ \rho wH - \frac{1}{Re}u\tau_{xz} - \frac{1}{Re}v\tau_{yz} - \frac{1}{Re}w\tau_{xz} - \frac{1}{RePr}k\frac{\partial T}{\partial z} \end{pmatrix}$$

where ε is the total energy per unit mass. Eqn (2.1) is written in non-dimensional form where the x, y and z coordinates are normalized by a characteristic length scale L , the u, v and w velocity components are normalized by the free stream velocity q_∞ , the density is normalized by the free stream density ρ_∞ , the pressure is normalized by $\rho_\infty q_\infty^2$, while the temperature is normalized by q_∞^2/C_p .

For aerodynamic applications, ε represents the sum of internal energy (e) and kinetic energy while potential energy is neglected. ε can be expressed as follows

$$\varepsilon = e + \frac{q^2}{2} \quad (2.2)$$

where the total energy and the total enthalpy are related as follows

$$H = \varepsilon + \frac{P}{\rho} \quad (2.3)$$

Eqn (2.1) is written in conservation form to capture correctly shock waves and discontinuities in the flow field [59]. An equation of state is needed to close the system of equations. For aerodynamics, the perfect gas equation of state is used.

$$P = (\gamma - 1) \rho e \quad (2.4)$$

The system of equations is solved for the conservative variables represented in the vector of unknowns \mathbf{U} and the pressure. Non-conservative formulations also exist where the system of equations is solved for the primitive variables ρ, u, v, w, P and T .

2.2 The Hierarchical Formulation

The objective of the new hierarchical formulation is to introduce a potential function ϕ as one of the dependent variables in the Navier-Stokes equations. This is achieved by a Helmholtz decomposition of the velocity vector into the gradient of a potential function plus a rotational component

$$\vec{q} = \nabla\phi + \vec{q}^* \quad (2.5)$$

Alternative decompositions are possible, see for example [60] where a multiplicative decomposition of the velocity vector is used. Based on eqn (2.5), the vorticity $\vec{\omega}$ can be expressed in terms of \vec{q}^* as follows

$$\vec{\omega} = \nabla \times \vec{q} = \nabla \times \vec{q}^* \quad (2.6)$$

Substituting eqn (2.5) into the continuity equation results in an augmented potential equation

$$\nabla \cdot (\rho \nabla \phi) = -\nabla \cdot (\rho \vec{q}^*) \quad (2.7)$$

The potential function ϕ is evaluated from the augmented potential equation (2.7). For viscous flows, the right hand side of eqn (2.7) is a source term representing the displacement thickness effects (δ^*) on the potential flow field. Notice the analogy between the source term in eqn (2.7) and viscous/inviscid interaction methods where the potential flow is solved with mass sources at the body which again represent the displacement thickness effects. Hence, the source term in eqn (2.7) is responsible for the interaction between the potential flow region and the viscous flow region. Notice also that in the far field, \vec{q}^* vanishes thus recovering potential flow which is governed by the single variable ϕ .

The pressure and density are reformulated in terms of the speed and entropy in

order to introduce the entropy (S) as another new dependent variable within the formulation, as follows

$$\rho = \rho_i e^{-\frac{\Delta S}{R}} \quad (2.8)$$

$$P = P_i e^{-\frac{\Delta S}{R}} \quad (2.9)$$

where

$$\Delta S = S - S_\infty \quad (2.10)$$

$$\rho_i = \left[(\gamma - 1) M_\infty^2 \left(H - \frac{1}{2} q^2 \right) \right]^{\frac{1}{\gamma-1}} \quad (2.11)$$

$$P_i = \frac{\rho_i^\gamma}{\gamma M_\infty^2} \quad (2.12)$$

The total enthalpy H is obtained from the energy equation.

$$\nabla \cdot \rho \vec{q} H = \frac{1}{Re Pr} \nabla \cdot k \nabla T + \frac{1}{Re} \nabla \cdot \bar{\tau} \cdot \vec{q} \quad (2.13)$$

For $Pr = 1$ and for high Reynolds number flows, the energy equation reduces to the following form (thin layer approximation)

$$\rho u H_x + \rho v H_y = \frac{1}{Re} (\mu H_y)_y \quad (2.14)$$

Eqn (2.14) admits constant total enthalpy as a solution everywhere in the flow field even inside the viscous layer.

$$H = C_p T + \frac{1}{2} q^2 = H_\infty = \frac{1}{\gamma - 1} \frac{1}{M_\infty^2} + \frac{1}{2} \quad (2.15)$$

Notice that admitting constant total enthalpy as a solution of the energy equation implies that there is no heat transfer through the solid surface (i.e. $\frac{\partial T}{\partial n} = 0$) and that the temperature of the solid surface is constant and is equal to the stagnation temperature of the free stream. For aerodynamic flows, $Pr = 0.72$, using constant total enthalpy is an acceptable approximation for the solution of the energy equation.

For constant total enthalpy, eqn (2.11) becomes

$$\rho_i = \left[1 - \frac{\gamma - 1}{2} M_\infty^2 (q^2 - 1) \right]^{\frac{1}{\gamma-1}} \quad (2.16)$$

For the general case, the energy equation (2.13) is used in its general form to evaluate the total enthalpy.

2.3 Evaluation of Entropy and Vorticity

The rotational velocity \vec{q}^* , representing the vorticity, and the entropy S are obtained from the momentum equations. Notice, however, that based on the mechanisms of entropy and vorticity generation in aerodynamic flows, the flow field can be

decomposed into three distinct regions as shown in fig (2.1). The details of evaluating S and \vec{q}^* inside each of these regions are given in the following sections.

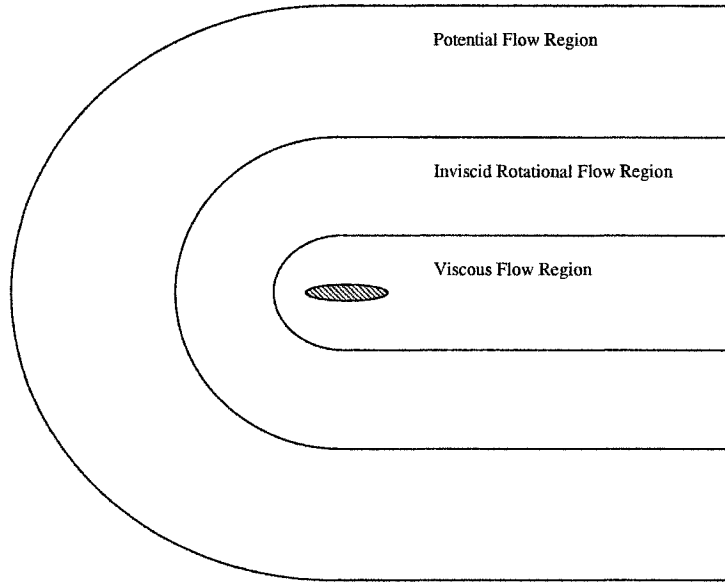


Figure 2.1: Flow Field Decomposition for Compressible Flows

2.3.1 Potential Flow Regions

In the outer field, assuming uniform upstream conditions, the flow is isentropic ($\Delta S = 0$) and irrotational ($\vec{q}^* = \vec{0}$) everywhere. Therefore, the hierarchical formulation reduces naturally to the potential flow formulation which is governed by the single variable ϕ .

For the other two regions, it is useful to identify the different entropy generation mechanisms in each of them. Entropy is generated in the inviscid rotational

flow regions by shock waves, while entropy in the viscous flow regions is generated by the viscous dissipation in the boundary layer. The different entropy generation mechanisms are summarized in fig(2.2).

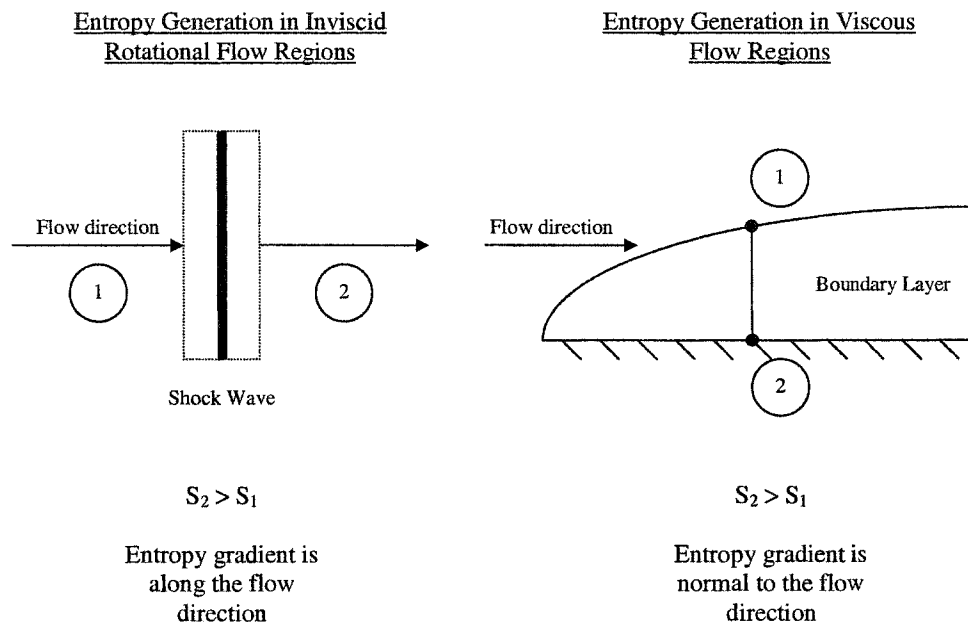


Figure 2.2: Entropy Generation in Inviscid and Viscous Flow Regions

2.3.2 Inviscid Rotational Flow Regions

As shown in fig(2.2), the direction of the entropy gradient is aligned with the flow direction. Therefore, the tangential momentum equation is used to evaluate the entropy. The deferred correction approach is used in solving for the entropy to guarantee conservation of tangential momentum as follows

$$P_i \vec{q} \cdot \nabla (\delta \kappa) = -\vec{q} \cdot [\nabla \cdot (\rho \vec{q} \otimes \vec{q}) + \nabla P] \quad (2.17)$$

where $\delta \kappa$ is the correction for κ ($\kappa = e^{-\frac{\Delta S}{R}}$). The left hand side of eqn (2.17) comes from the pressure term of the tangential momentum equation as follows

$$\vec{q} \cdot \nabla P = \vec{q} \cdot \nabla (P_i \kappa) = P_i \vec{q} \cdot \nabla \kappa + \kappa \vec{q} \cdot \nabla P_i \quad (2.18)$$

The term $(\kappa \vec{q} \cdot \nabla P_i)$ is lagged from the previous iteration, while we substitute $(\kappa = \kappa_{old} + \delta \kappa)$ into the term $(P_i \vec{q} \cdot \nabla \kappa)$ which gives rise to the correction term on the left hand side of eqn (2.17).

On the other hand, \vec{q}^* is obtained from the momentum equations in the following manner. Starting with Crocco's relation,

$$(\nabla \times \vec{q}^*) \times \vec{q} = T \nabla S - \nabla H \quad (2.19)$$

the cross product of eqn (2.19) with \vec{q} is used to evaluate \vec{q}^* with a deferred correction approach

$$\vec{q} \times [(\nabla \times \delta \vec{q}^*) \times \vec{q}] = -\vec{q} \times [(\nabla \cdot (\rho \vec{q} \otimes \vec{q}) + \nabla P) / \rho] \quad (2.20)$$

Eqn(2.20) is used to march \vec{q}^* from the far field, where \vec{q}^* is zero, all the way through the inviscid rotational flow region. Notice that since the applied Helmholtz decomposition introduces an extra degree of freedom, one of the components of \vec{q}^*

can be chosen to be identically zero without any loss of generality.

For example, in the case of flow over a flat plate, the component of \vec{q}^* normal to the plate, w^* , is chosen to be identically zero, while u^* and v^* are evaluated from

$$\rho(u^2 + w^2)(\delta u^*)_z = u(R_{Z-Mom}) - w(R_{X-Mom})$$

$$\rho(u^2 + v^2)(\delta v^*)_x = v(R_{X-Mom}) - u(R_{Y-Mom})$$

where

$$R_{X-Mom} = [(\rho u^2)_x + (\rho vu)_y + (\rho wu)_z + P_x]$$

$$R_{Y-Mom} = [(\rho uv)_x + (\rho v^2)_y + (\rho wv)_z + P_y]$$

$$R_{Z-Mom} = [(\rho uw)_x + (\rho vw)_y + (\rho w^2)_z + P_z]$$

A similar approach can be found in [61].

2.3.3 Viscous Flow Regions

In viscous flow regions, the direction of the entropy gradient is normal to the flow direction as shown in fig (2.2). Therefore, the normal momentum equation is used to march the pressure from the edge of the boundary layer all the way to the solid

surface. Assuming μ is constant ($\mu = \mu_\infty$)

$$\frac{1}{Re} \nabla \cdot \vec{\tau} = \frac{1}{Re} \frac{\partial}{\partial x_j} \left[\left(\frac{\partial u_i}{\partial x_j} + \frac{\partial u_j}{\partial x_i} \right) - \frac{2}{3} \delta_{ij} \frac{\partial u_k}{\partial x_k} \right] = \frac{1}{Re} \left[\nabla^2 \vec{q} + \frac{1}{3} \nabla (\nabla \cdot \vec{q}) \right] \quad (2.21)$$

Hence, the normal momentum equation can be written as follows

$$\frac{\partial P}{\partial n} = \vec{n} \cdot \nabla P = -\vec{n} \cdot \left(\nabla \cdot (\rho \vec{q} \otimes \vec{q}) - \frac{1}{Re} \left[\nabla^2 \vec{q} + \frac{1}{3} \nabla (\nabla \cdot \vec{q}) \right] \right) \quad (2.22)$$

The entropy is then obtained from the pressure using eqn (2.9). In a body fitted coordinate system, the grid lines normal to the body are used in constructing the unit normal vector \vec{n} for eqn (2.22). The marching of the pressure using the normal momentum equation (2.22) has the advantage of eliminating the need for boundary conditions for the pressure and entropy at the solid surface.

Two approaches are used for the evaluation of \vec{q}^* in the viscous region. The first approach makes use of the extra degree of freedom introduced by the Helmholtz decomposition by choosing the component of \vec{q}^* normal to the body to be identically zero. The other two components are evaluated from their respective momentum equations, with the no-slip boundary condition enforced at the solid surface, in the following manner

$$\rho \vec{q} \cdot \nabla (\vec{t}_1 \cdot \delta \vec{q}^*) - \frac{1}{Re} \nabla^2 (\vec{t}_1 \cdot \delta \vec{q}^*) = -R_{t_1-Mom} \quad (2.23)$$

$$\rho \vec{q} \cdot \nabla (\vec{t}_2 \cdot \delta \vec{q}^*) - \frac{1}{Re} \nabla^2 (\vec{t}_2 \cdot \delta \vec{q}^*) = -R_{t_2-Mom} \quad (2.24)$$

where \vec{t}_1 and \vec{t}_2 are two orthogonal unit vectors along the solid surface. R_{t_1-Mom} and R_{t_2-Mom} are the residuals of the components of the vector momentum equation in the t_1 and t_2 directions respectively.

$$R_{t_1-Mom} = \vec{t}_1 \cdot \left(\nabla \cdot (\rho \vec{q} \otimes \vec{q}) + \nabla P - \frac{1}{Re} \left[\nabla^2 \vec{q} + \frac{1}{3} \nabla (\nabla \cdot \vec{q}) \right] \right) \quad (2.25)$$

$$R_{t_2-Mom} = \vec{t}_2 \cdot \left(\nabla \cdot (\rho \vec{q} \otimes \vec{q}) + \nabla P - \frac{1}{Re} \left[\nabla^2 \vec{q} + \frac{1}{3} \nabla (\nabla \cdot \vec{q}) \right] \right) \quad (2.26)$$

The second approach evaluates the cartesian components of \vec{q}^* from the x,y and z momentum equations as follows

$$\rho u(\delta u^*)_x + \rho v(\delta u^*)_y + \rho w(\delta u^*)_z - \frac{1}{Re} \nabla^2(\delta u^*) = -R_{X-Mom}$$

$$\rho u(\delta v^*)_x + \rho v(\delta v^*)_y + \rho w(\delta v^*)_z - \frac{1}{Re} \nabla^2(\delta v^*) = -R_{Y-Mom}$$

$$\rho u(\delta w^*)_x + \rho v(\delta w^*)_y + \rho w(\delta w^*)_z - \frac{1}{Re} \nabla^2(\delta w^*) = -R_{Z-Mom}$$

where the no-slip boundary condition is enforced at the solid surface and R_{X-Mom} , R_{Y-Mom} and R_{Z-Mom} are the residuals of the x,y and z momentum equations respectively.

tively and are evaluated as follows

$$R_{X-Mom} = \left[(\rho u^2)_x + (\rho v u)_y + (\rho w u)_z + P_x - \frac{1}{Re} \left(\nabla^2 u + \frac{1}{3} (\nabla \cdot \vec{q})_x \right) \right]$$

$$R_{Y-Mom} = \left[(\rho u v)_x + (\rho v^2)_y + (\rho w v)_z + P_y - \frac{1}{Re} \left(\nabla^2 v + \frac{1}{3} (\nabla \cdot \vec{q})_y \right) \right]$$

$$R_{Z-Mom} = \left[(\rho u w)_x + (\rho v w)_y + (\rho w^2)_z + P_z - \frac{1}{Re} \left(\nabla^2 w + \frac{1}{3} (\nabla \cdot \vec{q})_z \right) \right]$$

For simple geometries, both approaches are easy to implement, while the second approach allows greater flexibility in the simulation of flows in more complex geometries. It is worth noting that the hierarchical formulation admits the boundary layer approximation as a special case by replacing equation (2.22) with

$$\frac{\partial P}{\partial n} = 0 \quad (2.27)$$

2.4 The Incompressible Flow Limit

Notice that for incompressible flows with uniform upstream conditions, the flow field is decomposed into only two regions, a potential flow region and a viscous flow region as shown in fig (2.3). The inviscid rotational flow region is nonexistent in incompressible flows as there are no longer any mechanisms to generate entropy and vorticity in the inviscid flow due to the absence of shock waves.

The present formulation has a built-in preconditioning for the simulation of in-

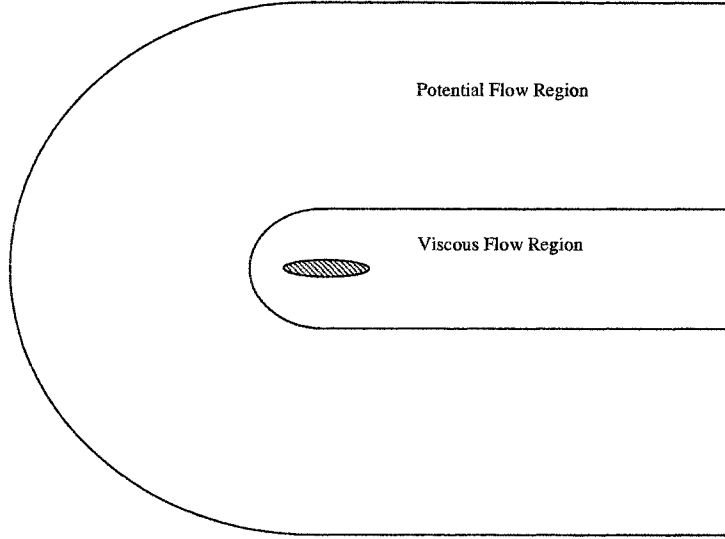


Figure 2.3: Flow Field Decomposition for Incompressible Flows

compressible flows. Eqn (2.16) shows that as $M_\infty \rightarrow 0$, $\rho_i \rightarrow 1$ and the density becomes constant. The potential function is evaluated from the augmented potential equation

$$\nabla^2 \phi = -\nabla \cdot \vec{q}^* \quad (2.28)$$

The rotational velocity \vec{q}^* vanishes in the potential flow region and is evaluated as in section (2.3.3) for the viscous flow region. The energy equation decouples and the entropy drops out of the formulation as the density and pressure are already known, the density being a constant and the pressure being obtained from the normal momentum equation.

For standard Navier-Stokes solvers, problems are encountered at the incompress-

ible flow limit since the time derivative of the density vanishes, hence the time dependent marching methods become ill-posed. Several methods were developed to remedy this problem, the most successful of them are the pseudo compressibility methods and the pressure correction methods. The pseudo compressibility method was introduced by Chorin [62], where a structure similar to the well-posed time marching structure of the compressible flow equations can be recovered by adding an artificial compressibility term under the form of a time derivative of pressure to the continuity equation, which vanishes when steady state is reached. The pressure correction method, first introduced by Harlow and Welch [63], solves the time-dependent momentum equations for the velocity components, together with a Poisson equation for the pressure obtained by taking the divergence of the momentum equation in conjunction with expressing the condition of a divergence-free velocity field.

The present formulation offers an alternative approach by exploiting the elliptic character of the mass conservation using eqn(2.28) to solve for the potential function. Hence, the potential function guarantees conservation of mass which eliminates the problems associated with the Poisson equation of the pressure .

CHAPTER 3

NUMERICAL METHODS

Finite difference, finite volume and finite element methods have all been successfully used as discretization schemes to the governing equations of Fluid Mechanics. In the present work, the finite volume method is selected as the discretization scheme for the hierarchical formulation. Quadrilateral control volumes are used for the two-dimensional problems while hexahedral control volumes are used for the three-dimensional problems. The details of the finite volume method are given in the following sections.

3.1 The Finite Volume Method

The finite volume method uses the integral form of the governing equations to conserve mass, momentum and energy over the finite control volumes generated by the grid. A cell vertex finite volume scheme is used in which the control volumes are constructed around the nodes (where variables are evaluated) as shown in fig (3.1).

The coordinates for the corners of the control volume are taken as the average of the coordinates of the four surrounding grid points. For example, the coordinates for

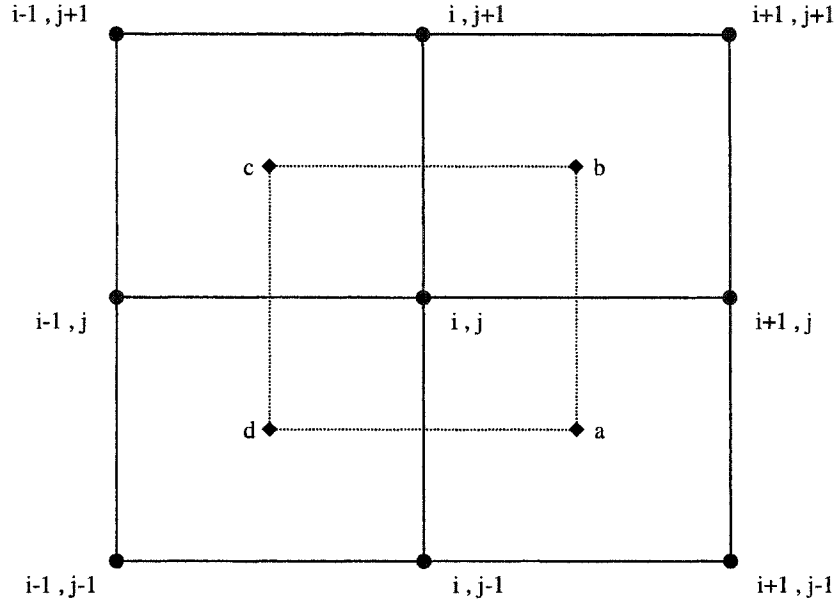


Figure 3.1: Two-Dimensional Finite Volume Method

point (a) are evaluated as follows

$$x_a = \frac{x_{i,j} + x_{i+1,j} + x_{i+1,j-1} + x_{i,j-1}}{4}$$

$$y_a = \frac{y_{i,j} + y_{i+1,j} + y_{i+1,j-1} + y_{i,j-1}}{4}$$

The areas of the controls volumes are obtained from Gauss Theorem in the following manner

$$A_{abcd} = \frac{1}{2} \oint (xdy - ydx) \quad (3.1)$$

Note that all line integrals have to be evaluated in a counterclockwise direction. The governing equations are integrated over the control volumes using Gauss Theorem. To illustrate the concept, consider the following partial differential equation in conservation form

$$\frac{\partial F}{\partial x} + \frac{\partial G}{\partial y} = 0 \quad (3.2)$$

The differential equation is integrated over the control volume using Gauss Theorem as follows

$$\iint \left(\frac{\partial F}{\partial x} + \frac{\partial G}{\partial y} \right) dx dy = \oint (F dy - G dx) = 0 \quad (3.3)$$

The line integral, representing the fluxes across the edges of the control volume, can now be evaluated in discrete form in the following manner

$$\begin{aligned} \oint (F dy - G dx) &= \langle F \rangle_{ab} [y]_{ab} - \langle G \rangle_{ab} [x]_{ab} \\ &\quad + \langle F \rangle_{bc} [y]_{bc} - \langle G \rangle_{bc} [x]_{bc} \\ &\quad + \langle F \rangle_{cd} [y]_{cd} - \langle G \rangle_{cd} [x]_{cd} \\ &\quad + \langle F \rangle_{da} [y]_{da} - \langle G \rangle_{da} [x]_{da} \end{aligned} \quad (3.4)$$

where $\langle \rangle$ represents the averaging operator and $[]$ represents the jump operator such that

$$\langle F \rangle_{ab} = \frac{F_a + F_b}{2}$$

$$[y]_{ab} = y_b - y_a$$

For second order derivatives, we consider the following differential equation

$$\frac{\partial^2 \tilde{F}}{\partial x^2} + \frac{\partial^2 \tilde{G}}{\partial y^2} = 0 \quad (3.5)$$

Equation (3.5) can be put in the same form as equation (3.2) by using the substitution $F = \tilde{F}_x$ and $G = \tilde{G}_y$. Therefore, the previous discussion holds for the discretization of second order derivatives provided that one can evaluate \tilde{F}_x and \tilde{G}_y at the corners of the control volume. This can be done by constructing a new control volume around each of the four corners (a, b, c, d) and evaluating \tilde{F}_x and \tilde{G}_y at each of them through a second application of Gauss Theorem as follows

$$\left(\frac{\partial \tilde{F}}{\partial x} \right)_a = \frac{\oint \tilde{F} dy}{A_a}$$

$$\left(\frac{\partial \tilde{G}}{\partial y} \right)_a = \frac{-\oint \tilde{G} dx}{A_a}$$

where A_a represents the area of the new control volume constructed around the corner point (a) . The finite volume method discussed above results in a nine-point

stencil and is second order accurate for reasonably stretched grids. The same finite volume method can be readily extended to three dimensions although it becomes much more complicated. Line integrals in two dimensions become surface integrals in three dimensions, while area integrals in two dimensions become volume integrals in three dimensions. For the three dimensional problem, hexahedral control volumes are constructed around the nodes as shown in fig(3.2). The coordinates for the corners of the hexahedron are taken as the average of the coordinates of the eight neighboring grid points.

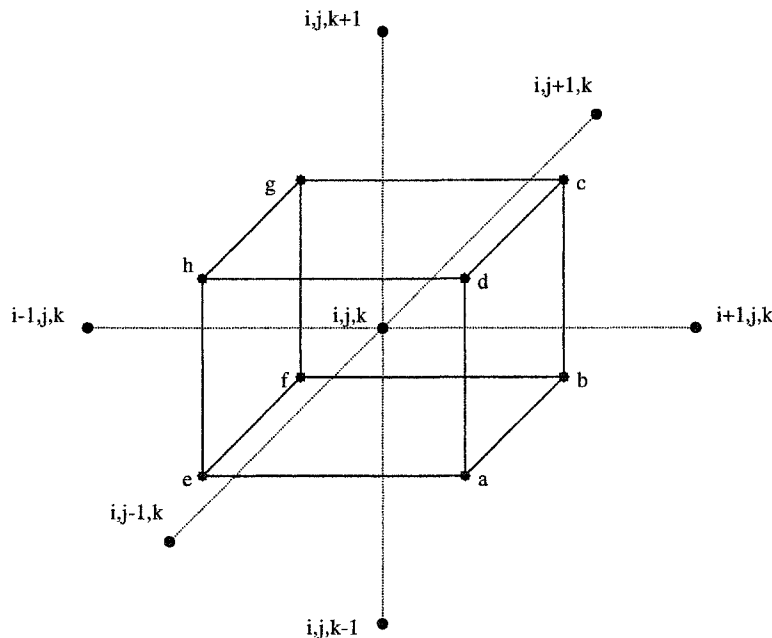


Figure 3.2: Three-Dimensional Finite Volume Method

Each cell-face consists of two planar triangles. Following Tannehill, Anderson and

Pletcher [64], the cell-face surface area vector, which is normal to the cell-face and pointing outwards, can be determined from

$$\vec{S}_{abcd} = \frac{1}{2} (\vec{r}_{ac} \times \vec{r}_{bd}) \quad (3.6)$$

where

$$\vec{r}_{ac} = \vec{r}_c - \vec{r}_a$$

$$\vec{r}_{bd} = \vec{r}_d - \vec{r}_b$$

$\vec{r}_a, \vec{r}_b, \vec{r}_c, \vec{r}_d$ are the position vectors of the points a, b, c, d respectively. The volume of the hexahedron can be obtained by subdividing it into tetrahedra or pyramids. Following [64], the hexahedron is subdivided into three pyramids that share the main diagonal as a common edge resulting in the following formula for the volume of a hexahedron

$$\vartheta = \frac{1}{3} (\vec{S}_{abcd} + \vec{S}_{dcgh} + \vec{S}_{bfgc}) \cdot (\vec{r}_c - \vec{r}_e) \quad (3.7)$$

The governing equations are integrated over the control volumes using Gauss Theorem. To illustrate how the integration is done in three dimensions, we consider the following differential equation

$$\frac{\partial E}{\partial x} + \frac{\partial F}{\partial y} + \frac{\partial G}{\partial z} = 0 \quad (3.8)$$

The divergence theorem of Gauss integrates this differential equation over the control volume and can be written in the following manner

$$\int \int \int \left(\frac{\partial E}{\partial x} + \frac{\partial F}{\partial y} + \frac{\partial G}{\partial z} \right) dx dy dz = \int \int (E \cos \alpha + F \cos \beta + G \cos \gamma) dA \quad (3.9)$$

where $\cos \alpha, \cos \beta$ and $\cos \gamma$ are the direction cosines for the cell-face surface area vector \vec{S} such that

$$\vec{n} = \cos \alpha \vec{i} + \cos \beta \vec{j} + \cos \gamma \vec{k} = \frac{\vec{S}}{\|\vec{S}\|} \quad (3.10)$$

The surface integral, representing the fluxes across the faces of the control volume, can be expressed in discrete form as follows

$$\sum_{i=1}^6 \left(\langle E \rangle_i \|\vec{S}\|_i (\cos \alpha)_i + \langle F \rangle_i \|\vec{S}\|_i (\cos \beta)_i + \langle G \rangle_i \|\vec{S}\|_i (\cos \gamma)_i \right) = 0$$

where the averaging operator is performed in the following manner

$$\langle E \rangle_{abcd} = \frac{E_a + E_b + E_c + E_d}{4} \quad (3.11)$$

For second order derivatives, the same approach used in the two-dimensional finite volume method can be readily extended to three dimensions. For second order derivatives, we consider the following differential equation

$$\frac{\partial^2 \tilde{E}}{\partial x^2} + \frac{\partial^2 \tilde{F}}{\partial y^2} + \frac{\partial^2 \tilde{G}}{\partial z^2} = 0 \quad (3.12)$$

Equation (3.12) can be put in the same form as equation (3.8) by using the substitution $E = \tilde{E}_x$, $F = \tilde{F}_y$ and $G = \tilde{G}_z$. Therefore, the previous discussion holds for the discretization of second order derivatives provided that one can evaluate \tilde{E}_x , \tilde{F}_y and \tilde{G}_z at the corners of the control volume. This can be done by constructing a new hexahedron around each of the eight corners (a, b, c, d, e, f, g, h) and evaluating \tilde{E}_x , \tilde{F}_y and \tilde{G}_z at each of them through a second application of Gauss Theorem as follows

$$\left(\frac{\partial \tilde{E}}{\partial x} \right)_a = \frac{\iint \tilde{E} \cos \alpha dA}{\vartheta_a}$$

$$\left(\frac{\partial \tilde{F}}{\partial y} \right)_a = \frac{\iint \tilde{F} \cos \beta dA}{\vartheta_a}$$

$$\left(\frac{\partial \tilde{G}}{\partial z} \right)_a = \frac{\iint \tilde{G} \cos \gamma dA}{\vartheta_a}$$

where ϑ_a represents the volume of the new hexahedron constructed around the corner point (a). The three dimensional finite volume method discussed above results in a 27-point stencil and is second order accurate for reasonably stretched grids.

3.2 The Potential Flow Solver

For incompressible and purely subsonic flows, the finite volume method discussed above can be directly applied to the potential equation and is second order accurate. For transonic and supersonic flows, two necessary modifications need to be introduced for the simulation of the locally supersonic flow.

3.2.1 Upwinding

To explain the need for these necessary modifications, it is useful to rewrite the potential equation in the following nonconservative form

$$\frac{1}{a^2} (\phi_{tt} + 2q\phi_{st}) = (1 - M^2)\phi_{ss} + \phi_{nn} \quad (3.13)$$

where s represents the streamline direction and n represents the direction normal to the streamline. For locally supersonic flow, $(1 - M^2)$ is negative and if a central discretization scheme is used, the resulting matrix is no longer guaranteed to be diagonally dominant. Another problem caused by central discretization schemes is that they violate the zone of dependence for supersonic flows. Therefore, upwinding the term $(1 - M^2)\phi_{ss}$ is essential to honour the zone of dependence for supersonic flows and to allow for shock capturing. For the potential equation in conservation form, the upwinding could be introduced through artificial compressibility methods by using an upwind density bias as proposed by Hafez, South and Murman [8] or an upwind flux bias as proposed by Hafez, Whitlow and Osher [9]. In the present work, upwinding the flux is adopted and the modified density is given by

$$\bar{\rho} = \rho - \frac{(\bar{\rho}q)_s}{q} \Delta s \quad (3.14)$$

where

$$\bar{\rho}q = \begin{cases} \rho^* q^* & \text{if } M \leq 1 \\ \rho q & \text{if } M > 1 \end{cases} \quad (3.15)$$

In equation (3.15), $\rho^* q^*$ is the flux at the sonic condition which is a function of the free stream Mach number.

$$\rho^* = \left[\frac{2 + (\gamma - 1) M_\infty^2}{(\gamma + 1)} \right]^{\frac{1}{\gamma-1}}$$

$$q^* = \sqrt{\frac{2 + (\gamma - 1) M_\infty^2}{(\gamma + 1) M_\infty^2}}$$

With the modified density, the finite volume discretization scheme is applicable for the mixed type potential equation. It is worth noting that the upwinding of the flux is completely equivalent to the addition of artificial viscosity which provides the necessary dissipation that is sufficient to enforce the missing entropy condition in the isentropic potential flow formulation and exclude non physical expansion shocks which are also a solution of the isentropic potential equation. An in-depth discussion of the mathematical entropy condition for inviscid flow models is given in [65].

3.2.2 The Iterative Solver (SLOR)

The other necessary modification is concerned with the iterative scheme. The system of equations resulting from the finite volume discretization of the potential equation are solved using successive line over-relaxation (SLOR). In this iterative solver, the unknowns along the grid lines normal to the body are solved for implicitly using a tridiagonal solver while lagging the density from the previous iteration and the domain is swept repeatedly until convergence is achieved.

Iterative schemes introduce an artificial time, representing the evolution of the solution through the iterations. From eqn (3.13), the unsteady behavior of the potential equation is represented by the two terms ϕ_{tt} and ϕ_{st} . The ϕ_{tt} term is not essential while the ϕ_{st} term is needed to ensure a well posed problem in the artificial time for locally supersonic flows. Therefore, the iterative scheme must be modified explicitly or implicitly to introduce the upwinded ϕ_{st} term in supersonic flow regions. In the present work, we introduce the upwinded ϕ_{st} term both explicitly by adding it to the potential equation and implicitly by sweeping the domain along the flow direction during the iterations.

3.3 Convection/Diffusion Equations

Two modifications are required for the solution of the convection/diffusion equations for entropy, vorticity and total enthalpy. The first modification is the need for a suitable upwind scheme to handle the convection terms. The second modification is the addition of an artificial time dependent term to the convection/diffusion

equations. These two modifications are discussed in detail in the next two sections.

3.3.1 Upwinding

To illustrate the upwind scheme used for the convection/diffusion equations, it is useful to consider first the inviscid Burger's equation

$$u_t + uu_x = 0 \quad (3.16)$$

A first order upwind scheme, using a finite difference approximation, for eqn (3.16) is

$$\frac{u_i^{n+1} - u_i^n}{\Delta t} + u_i^n \frac{u_i^n - u_{i-1}^n}{\Delta x} = 0 \quad u_i^n > 0 \quad (3.17)$$

$$\frac{u_i^{n+1} - u_i^n}{\Delta t} + u_i^n \frac{u_{i+1}^n - u_i^n}{\Delta x} = 0 \quad u_i^n < 0 \quad (3.18)$$

Eqns (3.17) and (3.18) can be rewritten into a single expression as follows

$$\frac{u_i^{n+1} - u_i^n}{\Delta t} + u_i^n \frac{u_{i+1}^n - u_{i-1}^n}{2\Delta x} - |u_i^n| \frac{\Delta x}{2} \frac{u_{i+1}^n - 2u_i^n + u_{i-1}^n}{\Delta x^2} = 0 \quad (3.19)$$

Hence, an upwind scheme can be interpreted as a central difference scheme augmented with an artificial dissipation term that is needed to produce the right upwind effect when the velocity (u) is either positive or negative. Now, let's consider the x-momentum equation that is used in evaluating u^*

$$\rho u(\delta u^*)_x + \rho v(\delta u^*)_y + \rho w(\delta u^*)_z - \frac{1}{Re} \nabla^2(\delta u^*) = -R_{X-Mom} \quad (3.20)$$

where

$$R_{X-Mom} = \left[(\rho u^2)_x + (\rho vu)_y + (\rho wu)_z + P_x - \frac{1}{Re} \left(\nabla^2 u + \frac{1}{3} (\nabla \cdot \vec{q})_x \right) \right] \quad (3.21)$$

The convection terms in eqns (3.20) and (3.21) are upwinded by the addition of an artificial dissipation term as follows

$$\rho u(\delta u^*)_x + \rho v(\delta u^*)_y + \rho w(\delta u^*)_z - \frac{1}{Re} \nabla^2(\delta u^*) - D(\delta u^*) = -R_{X-Mom} \quad (3.22)$$

where

$$R_{X-Mom} = \left[(\rho u^2)_x + (\rho vu)_y + (\rho wu)_z + P_x - \frac{1}{Re} \left(\nabla^2 u + \frac{1}{3} (\nabla \cdot \vec{q})_x \right) - \tilde{D}(u) \right] \quad (3.23)$$

The artificial dissipation operators (D) and (\tilde{D}) are defined as follows

$$D(\delta u^*) = \varepsilon_1 |\rho u| \delta u_{xx}^* + \varepsilon_2 |\rho v| \delta u_{yy}^* + \varepsilon_3 |\rho w| \delta u_{zz}^*$$

$$\tilde{D}(u) = (\varepsilon_1 |\rho u| u_x)_x + (\varepsilon_2 |\rho v| u_y)_y + (\varepsilon_3 |\rho w| u_z)_z$$

where $\varepsilon_1 = O\left(\frac{\Delta x}{2}\right)$, $\varepsilon_2 = O\left(\frac{\Delta y}{2}\right)$ and $\varepsilon_3 = O\left(\frac{\Delta z}{2}\right)$. Notice that (\tilde{D}) is in conserva-

tion form. The same procedure described above for upwinding the convection terms of the x-momentum equation is applied to the other convection/diffusion equations within the hierarchical formulation.

3.3.2 The Iterative Solver (SLOR)

The system of equations resulting from the finite volume discretization of the upwinded convection/diffusion equations are solved iteratively using successive line over-relaxation (SLOR). In this procedure, the unknowns along the grid lines normal to the body are solved for implicitly using a tridiagonal solver and the domain is swept repeatedly along the flow direction until convergence is achieved. As mentioned in section (3.2.2), iterative schemes introduce an artificial time representing the evolution of the solution through the iterations. Hence, an artificial time dependent term is added to the convection/diffusion equations. For example, the artificial time dependent term is added to the x-momentum equation as follows

$$\rho \frac{\delta u^*}{\delta t} + \rho u(\delta u^*)_x + \rho v(\delta u^*)_y + \rho w(\delta u^*)_z - \frac{1}{Re} \nabla^2(\delta u^*) - D(\delta u^*) = -R_{X-Mom} \quad (3.24)$$

The addition of $\rho \frac{\delta u^*}{\delta t}$ helps the convergence of iterations. Furthermore, the addition of $\rho \frac{\delta u^*}{\delta t}$ augments the diagonal of the coefficient matrix which leads to more stable calculations.

3.4 Boundary Conditions

3.4.1 Solid Surface Boundary Condition

The control volumes at the solid surface are constructed as shown in fig (3.3) for the two dimensional case.

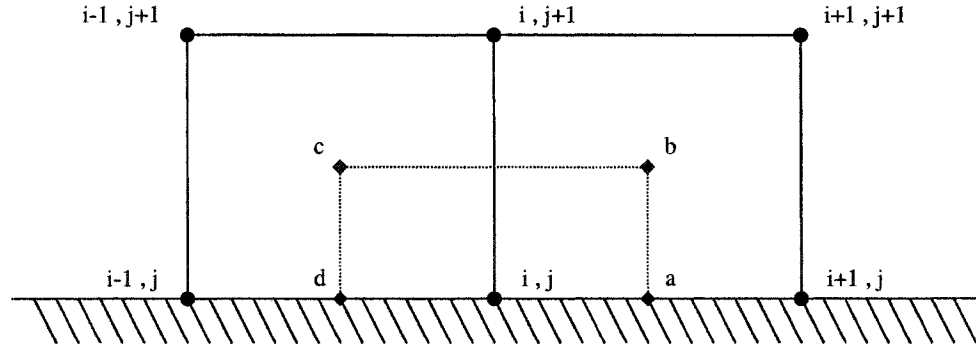


Figure 3.3: Solid Surface Boundary Condition

The coordinates for points (b) and (c) are evaluated as in section (3.1) while the coordinates for points (a) and (d) are evaluated as the average of the coordinates of the two neighbouring surface grid points. For example, the coordinates for point (a) are

$$x_a = \frac{x_{i,j} + x_{i+1,j}}{2}$$

$$y_a = \frac{y_{i,j} + y_{i+1,j}}{2}$$

The same strategy is extended to the three dimensional case, where the coordinates of the corners of the control volume that lie on the surface are evaluated as the average of the coordinates of the four neighbouring surface grid points.

For inviscid flows, the boundary condition at a solid surface is the no-penetration condition which can be expressed as follows

$$\vec{q} \cdot \vec{n} = 0 \quad (3.25)$$

Applying the Helmholtz decomposition of the velocity vector to eqn(3.25) results in the following boundary condition

$$\frac{\partial \phi}{\partial n} = -\vec{q}^* \cdot \vec{n} \quad (3.26)$$

Since the component of \vec{q}^* normal to the surface is chosen to be identically zero, then the boundary condition at the solid surface becomes

$$\frac{\partial \phi}{\partial n} = 0 \quad (3.27)$$

This boundary condition is implemented numerically by simply not evaluating the fluxes going through the surface. For example, in fig (3.3), the fluxes through the edge (*ad*) are set to zero in eqn (3.4).

For viscous flows, the no-slip boundary condition is imposed at the solid surface. For a stationary solid surface, the boundary condition is

$$\vec{q} = 0 \quad (3.28)$$

Applying the Helmholtz decomposition of the velocity vector to eqn(3.28) results in the following boundary condition

$$\nabla\phi = -\vec{q}^* \quad (3.29)$$

For viscous flows, there are two approaches for the evaluation of \vec{q}^* . In the first approach, the component of \vec{q}^* normal to the surface is chosen to be identically zero. Based on this approach, eqn (3.29) can be expressed in terms of three components (t_1, t_2, n) where t_1 and t_2 are two orthogonal directions along the surface

$$\frac{\partial\phi}{\partial n} = -\vec{q}^* \cdot \vec{n}$$

$$\frac{\partial\phi}{\partial t_1} = -\vec{q}^* \cdot \vec{t}_1$$

$$\frac{\partial\phi}{\partial t_2} = -\vec{q}^* \cdot \vec{t}_2$$

Since the component of \vec{q}^* normal to the surface is zero, the boundary conditions at the solid surface become

$$\frac{\partial\phi}{\partial n} = 0 \quad (3.30)$$

$$\vec{q}^* \cdot \vec{t}_1 = -\frac{\partial\phi}{\partial t_1} \quad (3.31)$$

$$\vec{q}^* \cdot \vec{t}_2 = -\frac{\partial \phi}{\partial t_2} \quad (3.32)$$

Eqn (3.30) provides a Neumann boundary condition for the potential function, while eqns (3.31) and (3.32) provide Dirichlet boundary conditions for the two components of \vec{q}^* .

In the second approach for evaluating \vec{q}^* , the cartesian components of \vec{q}^* are evaluated from the x,y and z momentum equations. Based on this approach, eqn (3.29) can be rewritten in terms of its cartesian components as follows

$$u^* = -\frac{\partial \phi}{\partial x} \quad (3.33)$$

$$v^* = -\frac{\partial \phi}{\partial y} \quad (3.34)$$

$$w^* = -\frac{\partial \phi}{\partial z} \quad (3.35)$$

Eqns (3.33)-(3.35) provide Dirichlet boundary conditions for u^* , v^* and w^* at the solid surface that are sufficient to enforce the no-slip condition. The boundary condition for ϕ is chosen to be

$$\frac{\partial \phi}{\partial n} = 0 \quad (3.36)$$

Notice that choosing eqn (3.36) implies that the component of \vec{q}^* normal to the surface is equal to zero, at the surface, which is similar to the choice made in the first approach.

3.4.2 Farfield Boundary Condition

In this section, the farfield boundary condition for the two dimensional problem is discussed. The farfield boundary condition for the three dimensional problem is discussed in detail in the chapter involving the three dimensional flow over wings.

For two dimensional flows with uniform upstream conditions, the inflow is basically irrotational and isentropic, hence

$$\Delta S = 0 \quad (3.37)$$

$$\vec{q}^* = \vec{0} \quad (3.38)$$

$$H = H_\infty = \frac{1}{\gamma - 1} \frac{1}{M_\infty^2} + \frac{1}{2} \quad (3.39)$$

The outflow boundary condition is obtained via extrapolation as follows

$$\Delta S_{ss} = 0 \quad (3.40)$$

$$\vec{q}_{ss}^* = \vec{0} \quad (3.41)$$

$$H_{ss} = 0 \quad (3.42)$$

As for the potential function, for subsonic upstream conditions, ϕ is represented by a uniform flow for nonlifting surfaces

$$\phi = U_\infty x + V_\infty y \quad (3.43)$$

For lifting surfaces, an irrotational vortex is added to the farfield boundary condition to allow for smaller computational domains

$$\phi = U_\infty x + V_\infty y + \frac{\Gamma}{2\pi} \tan^{-1} \left[\sqrt{1 - M_\infty^2} \tan(\theta - \alpha) \right] \quad (3.44)$$

where Γ is the circulation in the farfield, θ is the angular position of the far field point from the quarter chord and α is the angle of attack. Notice that the Prandtl-Glauert transformation is used in eqn (3.44) to account for compressibility effects. A detailed discussion of the Prandtl-Glauert transformation is given in [66].

For supersonic upstream conditions, the upstream boundary condition is represented by a uniform flow for both lifting and nonlifting surfaces

$$\phi = U_\infty x + V_\infty y \quad (3.45)$$

while the downstream boundary condition is obtained via extrapolation

$$\phi_{ss} = 0 \quad (3.46)$$

Note that the free stream velocity components (U_∞, V_∞) can be expressed in terms of the angle of attack (α) as follows

$$U_\infty = \cos \alpha$$

$$V_\infty = \sin \alpha$$

With the end of this chapter, the details of the hierarchical formulation and the numerical methods have been introduced. In the next chapters, the formulation is applied to a wide range of inviscid and viscous flow problems.

CHAPTER 4

FLOW OVER A FLAT PLATE

4.1 Incompressible Flow

In the following, incompressible viscous flows over semi-infinite and finite flat plates are simulated using the present formulation.

4.1.1 Flow over a Semi-Infinite Flat Plate with and without Suction

The results of the classical Prandtl boundary layer theory for laminar flow over a semi-infinite flat plate, away from the leading edge, are given by the Blasius self-similar solution where the pressure gradients in both the streamwise and normal directions are ignored.

On the other hand, in the present formulation the potential equation is elliptic and the pressure gradient does not necessarily vanish. If the domain is limited to the viscous layer with uniform flow on its outer boundary and non-reflecting boundary conditions at the exit plane, and if the normal momentum equation is replaced by the assumption of uniform pressure, the results of the calculations are in good agreement with Blasius solution as shown in fig(4.1).

Next, a semi-infinite plate with uniform suction is considered. An exact solution is

available for both boundary layer and Navier-Stokes equations which has the following form.

$$u = 1 - e^{-V_s Re_L y} \quad (4.1)$$

where $v = -V_s$ at the plate surface. Again, the results of the present formulation, away from the leading edge, are in good agreement with the analytical solution, see fig(4.2). Notice that with suction control, the boundary layer does not grow (see figs(4.3) and (4.4)).

4.1.2 Flow over a Finite Flat Plate: The Trailing-Edge Problem

The solution of the boundary layer equations leads to a singularity at the trailing edge as shown by Goldstein [67]. In the late sixties, a triple deck theory was proposed to construct a higher order approximation based on a multi-structured asymptotic expansion valid in the limit of $Re \rightarrow \infty$ for laminar flow in the neighborhood of the trailing edge of a flat plate. The details of triple deck theory are available in many references, see for example [68]-[70]. Results obtained by triple deck theory agree with those of interacting boundary layers and with Navier-Stokes calculations provided the right scale is honored for the resolution of the solution in this region.

Calculations based on the present formulation for incompressible viscous flow over a finite flat plate at $Re = 1 \times 10^5$, including the normal pressure gradient in a large domain to allow for viscous/inviscid interaction effects, are tested using a very fine mesh which is stretched away from the surface of the plate. In particular, the mesh is constructed so as to be able to resolve the important length scales identified by

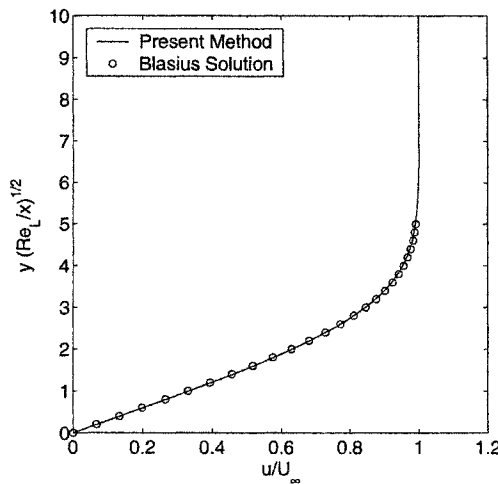


Figure 4.1: U-velocity profile for incompressible viscous flow over a semi-infinite flat plate ($Re = 1 \times 10^5$)

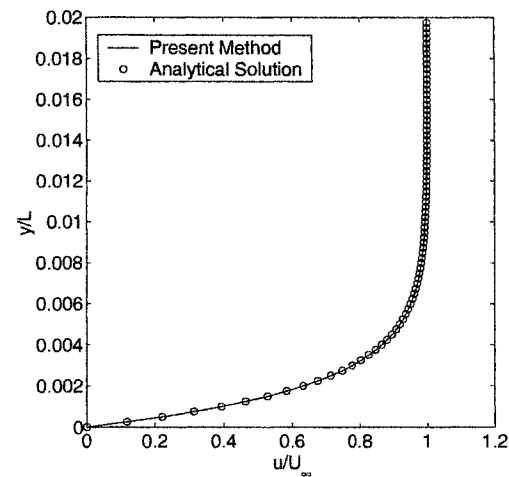


Figure 4.2: U-velocity profile for incompressible viscous flow over a semi-infinite flat plate with suction ($Re = 1 \times 10^5, V_s = 0.005$)

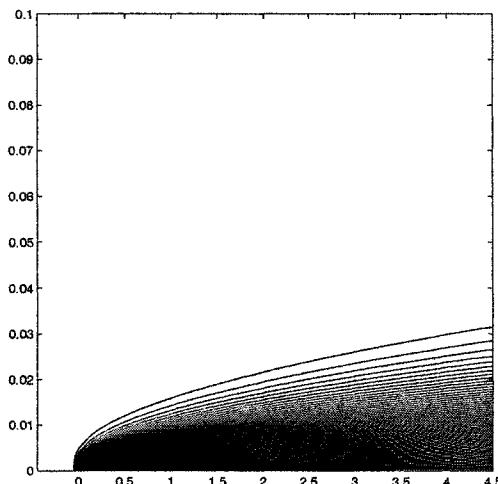


Figure 4.3: U-velocity contours for incompressible viscous flow over a semi-infinite flat plate ($Re = 1 \times 10^5$)

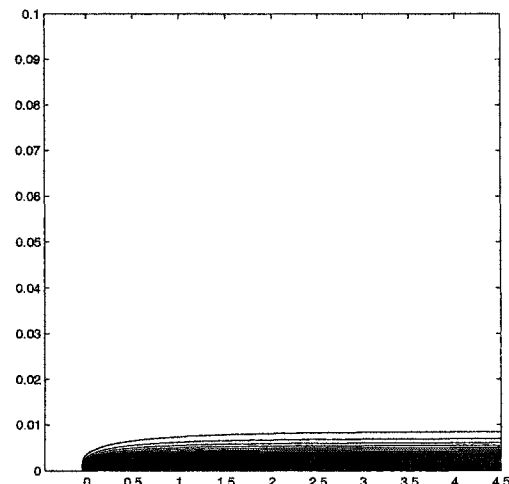


Figure 4.4: U-velocity contours for incompressible viscous flow over a semi-infinite flat plate with suction ($Re = 1 \times 10^5, V_s = 0.005$)

triple deck theory such as the lower deck region which has a thickness of $O(Re^{-\frac{5}{8}})$ and the trailing edge region which has a streamwise length of $O(Re^{-\frac{3}{8}})$. In fig(4.5), comparisons with classical results of Navier-Stokes equations [71] and interacting boundary layers [72] are plotted for surface pressure, skin friction, centerline velocity of the wake, displacement thickness and the defect velocity in the wake. Moreover, the results of the present formulation predict that the value of the skin friction at the trailing edge is 34% higher than the value obtained from the Blasius solution (non-interacting boundary layer). This is in good agreement with triple deck theory results [73] which predict a 35% rise.

4.2 Compressible Flow

Shock wave/boundary layer interaction is a classical problem of viscous/inviscid interaction. The adverse pressure gradient due to the shock often results in the separation of the boundary layer. A complex flow pattern is established as a result, consisting of a recirculating region with incident and reflected shocks as shown in figure (4.6).

Chapman et al. [74] obtained analytically an expression for the pressure rise by matching the pressure gradient from the small disturbance linearized supersonic flow and the pressure gradient from the boundary layer equations applied at the wall assuming the viscosity coefficient is linearly proportional to temperature, hence the skin friction is independent of the Mach number. This result agrees remarkably well with experiments (if the proper constant is used)

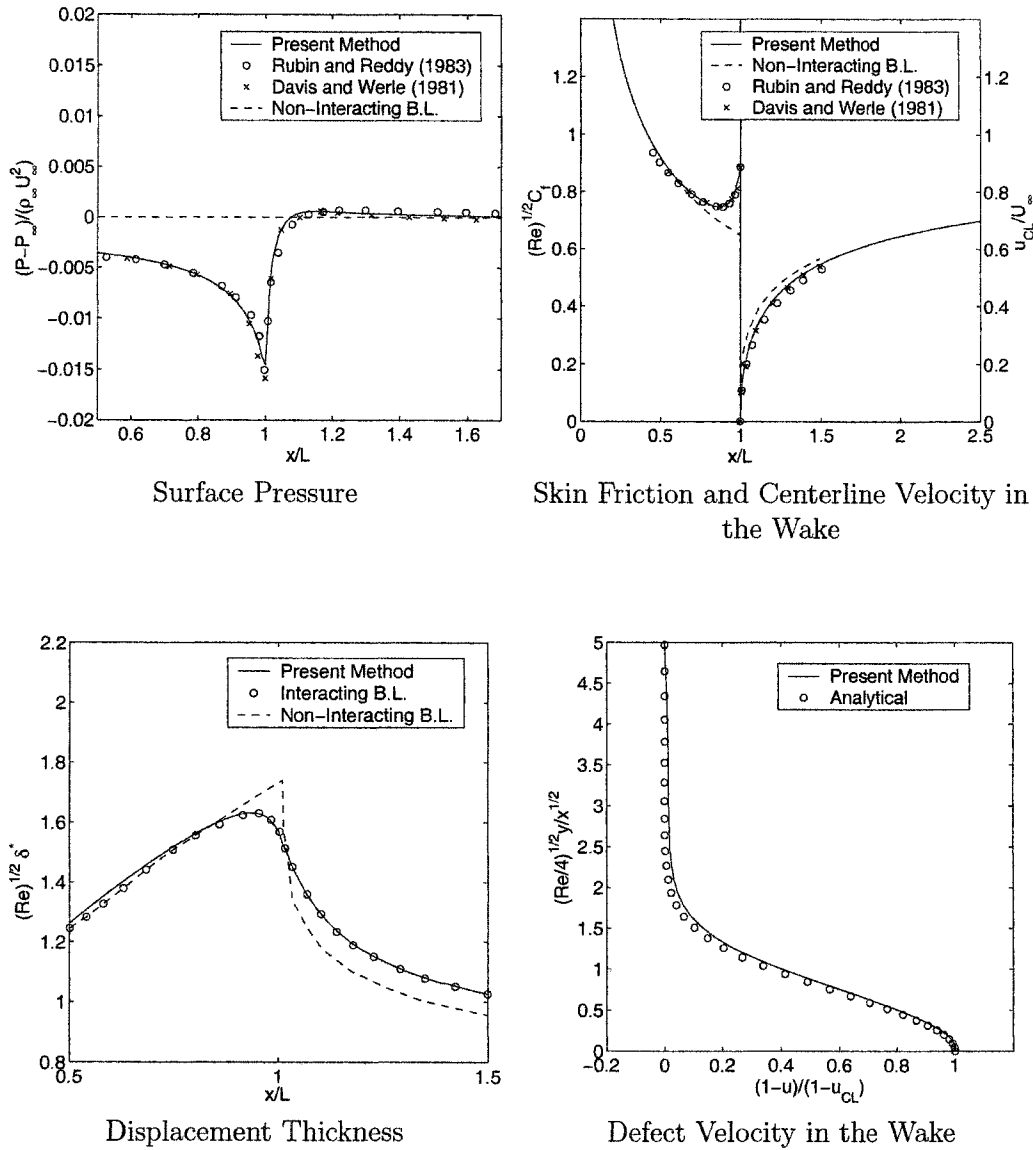


Figure 4.5: Incompressible viscous flow over a finite flat plate ($Re = 1 \times 10^5$)

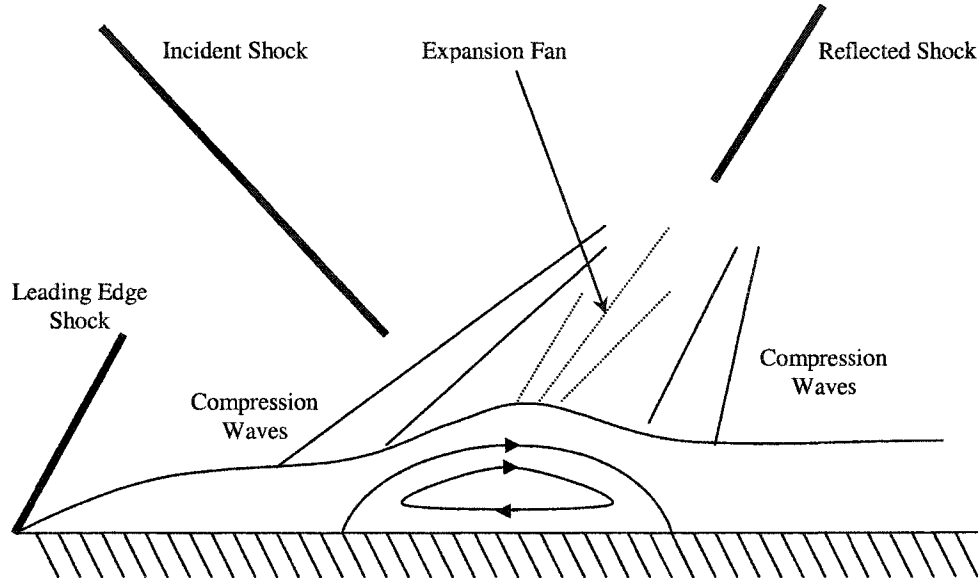


Figure 4.6: Shock Wave/Boundary Layer Interaction

$$\frac{\Delta P}{\rho U^2} \sim (M^2 - 1)^{-\frac{1}{2}} Re^{-\frac{1}{4}} \quad (4.2)$$

Experimental results for the interaction of an oblique shock wave with a laminar boundary layer at $M_\infty = 2.0$ are given by Hakkinen [75]. The same problem was solved numerically by MacCormack [76]. Since then, it became a benchmark problem for testing numerical schemes. In the present work, the hierarchical formulation is used to simulate this problem. First the inviscid flow over a wedge is calculated, then viscous effects are included and the shock wave/boundary layer interaction is simulated.

A non-reflecting boundary condition is used for the potential function at the upper

boundary, where the potential equation is solved implicitly with the Riemann invariant associated with the right running characteristic of the Prandtl-Glauert equation

$$\sqrt{M_\infty^2 - 1} \phi_x + \phi_y = C_1 \quad (4.3)$$

where C_1 is a constant determined from the prescribed velocities in the farfield (u_{FF}, v_{FF}) as follows

$$C_1 = \sqrt{M_\infty^2 - 1} u_{FF} + v_{FF} \quad (4.4)$$

A more accurate formula based on the nonlinear transonic small disturbance equation may be used.

4.2.1 Inviscid Flow over a Wedge

First, the inviscid supersonic flow over a wedge of half angle 3.08° at $M_\infty = 2.0$ is simulated. The shock is reflected from the flat plate. Pressure contours are given in fig(4.7), while the pressure distributions at the surface and at $y = 0.175$ are plotted in figs(4.9) and (4.11) showing a final pressure rise of 1.4, which agrees with inviscid flow theory.

4.2.2 Shock Wave/Boundary Layer Interaction

Next, the interaction of the oblique shock with a supersonic boundary layer developing over the flat plate at $M_\infty = 2.0$ and $Re_L = 2.96 \times 10^5$ is simulated where L represents the distance between the shock reflection point, as predicted from inviscid flow theory,

and the leading edge of the flat plate. The pressure contours are given in fig(4.8), while the pressure distributions at the surface and at $y = 0.175$ are plotted in figs(4.10) and (4.12). The u-velocity contours are given in fig(4.13) showing the presence of a recirculating region. The entropy contours are shown in fig(4.14), while the skin friction distribution and u-velocity profiles at various streamwise locations are plotted in figs(4.15) and (4.16) respectively. The comparison of surface pressure and skin friction distributions show that the results of the present method are in reasonable agreement with experimental results [75] and Navier-Stokes calculations [77].

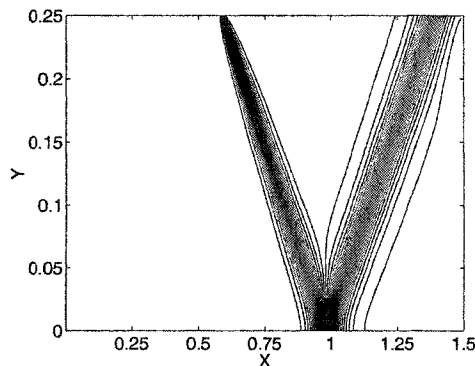


Figure 4.7: Pressure contours for Supersonic Potential Flow over a Wedge ($M_\infty = 2.0$)

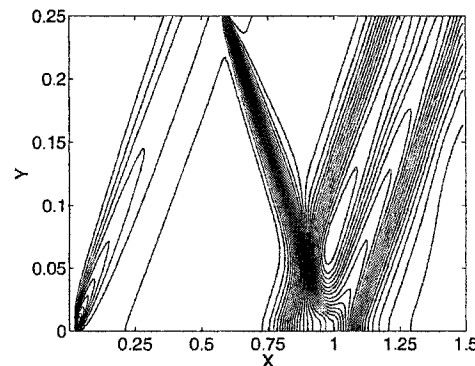


Figure 4.8: Pressure contours for Shock Wave/B.L. Interaction ($M_\infty = 2.0$, $Re_L = 2.96 \times 10^5$)

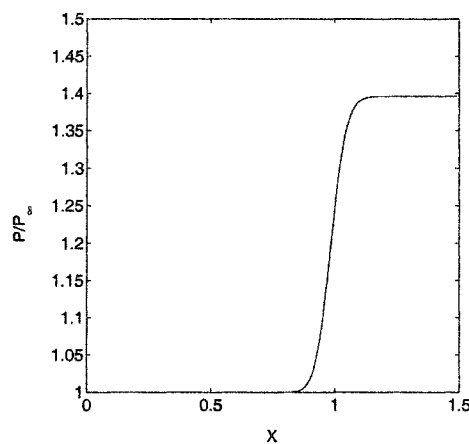


Figure 4.9: Surface Pressure for Supersonic Potential Flow over a Wedge ($M_\infty = 2.0$)

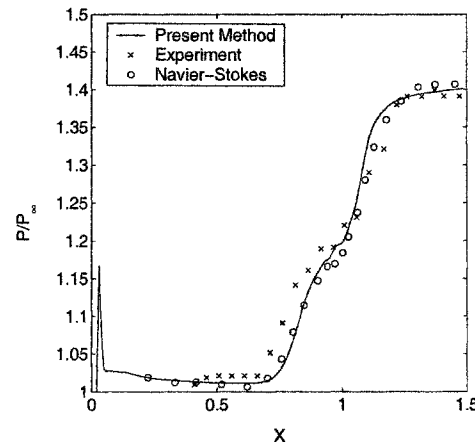


Figure 4.10: Surface Pressure for Shock Wave/B.L. Interaction ($M_\infty = 2.0$, $Re_L = 2.96 \times 10^5$)

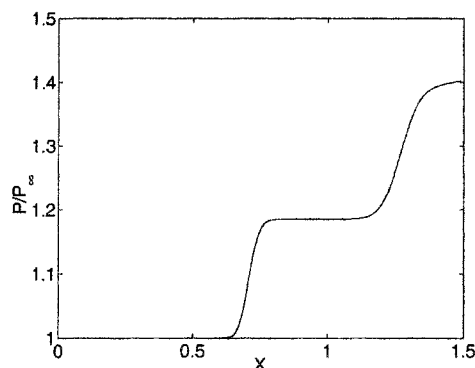


Figure 4.11: Pressure at $y=0.175$ for Supersonic Potential Flow over a Wedge ($M_\infty = 2.0$)

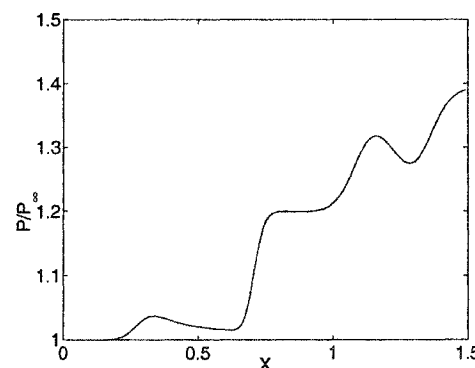


Figure 4.12: Pressure at $y=0.175$ for Shock Wave/B.L. Interaction ($M_\infty = 2.0$, $Re_L = 2.96 \times 10^5$)

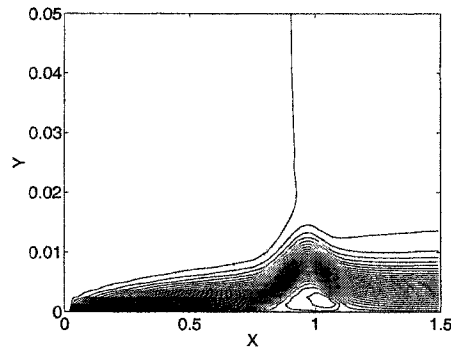


Figure 4.13: U contours for Shock Wave/B.L. Interaction ($M_\infty = 2.0$, $Re_L = 2.96 \times 10^5$)

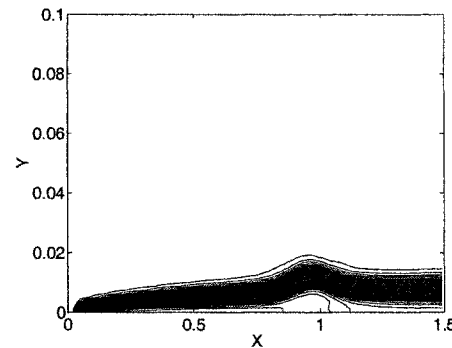


Figure 4.14: Entropy contours for Shock Wave/B.L. Interaction ($M_\infty = 2.0$, $Re_L = 2.96 \times 10^5$)

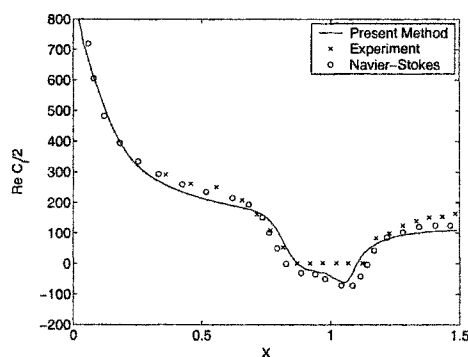


Figure 4.15: Skin friction coefficient for Shock Wave/B.L. Interaction ($M_\infty = 2.0$, $Re_L = 2.96 \times 10^5$)

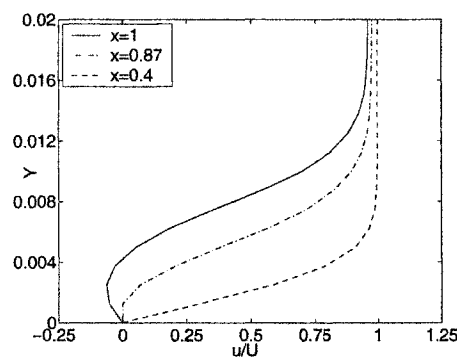


Figure 4.16: U-velocity profiles for Shock Wave/B.L. Interaction ($M_\infty = 2.0$, $Re_L = 2.96 \times 10^5$)

CHAPTER 5

INVISCID AND VISCOUS FLOWS OVER A CYLINDER

The flow over a cylinder is one of the most fundamental problems in fluid mechanics, in general, and in aerodynamics, in particular. Various types of flows over a cylinder have been experimentally, theoretically and numerically studied over the years. Recently, a book has been published on low speed flows around a circular cylinder [78]. Interesting experimental results can be found in the *Album of Fluid Motion* by van Dyke [79], see also [80].

Inviscid flows over a cylinder have been extensively studied in the past. The analytical solution for incompressible inviscid flow over a cylinder resulted in D'Alembert's paradox. Flow over a rotating cylinder is used to explain the Magnus effect and the generation of lift. Compressibility effects have been studied by Janzen, Rayleigh, Imai and others [81]. The critical Mach number, at which the sonic condition is attained, was predicted accurately by van Dyke using computer series extension techniques [82]. Numerical solutions of inviscid flows over a cylinder using Euler equations are reported in many papers, see for example [83], [84] and [85]. The simulation of inviscid flows over a cylinder can be considered a benchmark problem to test new Euler codes. Moreover, any airfoil (or any closed curve) can be mapped to a circle. Nonuniqueness

of transonic flows is also studied based on the numerical solutions of potential and Euler equations for flows over a cylinder [86] - [88].

On the other hand, viscous flows over a cylinder provide an excellent test case for flow separation in steady flows in the Reynolds number range $6 < Re < 40$, where Re is the Reynolds number based on the cylinder diameter. Viscous flows over a cylinder also provide another excellent test case for vortex shedding in unsteady flows for $Re > 40$ where the von Karman vortex street is formed in the wake of the cylinder. An in-depth discussion of the dramatic changes in the flow pattern in the wake of a cylinder with increasing the Reynolds number is given by Batchelor [89] and by Kundu [90]. Numerical simulations of rotating cylinders is also gaining considerable interest because of its application towards drag reduction and suppression of vortex induced oscillations in bluff body flows [91], [92].

5.1 Inviscid Flows Over a Cylinder

For steady, two-dimensional, inviscid, adiabatic and incompressible flows with uniform upstream conditions, the potential and stream functions are governed by Laplace equations. Analytical solutions can be obtained via the superposition principle. Adding the solutions of a uniform flow and a doublet yields the solution for an irrotational flow over a cylinder where the strength of the doublet is determined in terms of the radius of the cylinder and the speed of the uniform flow. A potential vortex is needed to simulate the effect of the cylinder rotation, while a sink is needed

to simulate the effect of suction through the cylinder surface.

$$\phi = r \cos \theta + \frac{\cos \theta}{r} + \frac{\Gamma}{2\pi} \theta + \frac{Q}{2\pi} \ln r \quad (5.1)$$

$$\psi = r \sin \theta - \frac{\sin \theta}{r} - \frac{\Gamma}{2\pi} \ln r + \frac{Q}{2\pi} \theta \quad (5.2)$$

Notice that the potential function is discontinuous in the presence of circulation (Γ) while the stream function is discontinuous in the presence of suction (Q).

5.1.1 Incompressible Shear Flow

If the incoming flow has vorticity, the potential function alone is not sufficient to represent such a flow. For two-dimensional (and axisymmetric) flows, the stream function can still be used, and it is governed by a Poisson's equation where vorticity is the forcing function. Since the vorticity remains constant along a streamline, the right hand side of the Poisson's equation depends on the stream function and this relation can be found from the incoming flow conditions. The problem becomes nonlinear and can be easily solved using iterative methods. For the special case of linear shear flow (constant vorticity) over half a cylinder, the analytical solution is available [93].

Alternatively, the solution can be obtained using the hierarchical formulation. In the far field, ϕ represents a uniform flow aligned with the x-axis

$$\phi_{FF} = x = r \cos \theta \quad (5.3)$$

Since the flow field has constant vorticity everywhere ($\omega = \text{constant}$), \vec{q}^* does not vanish in the far field and is evaluated as follows

$$\bar{u}_{FF}^* = \omega (L - r \sin \theta) \cos \theta$$

$$\bar{v}_{FF}^* = -\omega (L - r \sin \theta) \sin \theta$$

where \bar{u}^* and \bar{v}^* are the components of \vec{q}^* in the r and θ directions respectively and L is the vertical distance from the center of the cylinder to the outer boundary. Since one of the components of \vec{q}^* can be arbitrarily chosen, the component normal to the cylinder surface, \bar{u}^* , is chosen to have the same functional form $f(r, \theta)$ as it has in the far field

$$\bar{u}^* = \omega (L - r \sin \theta) \cos \theta \quad (5.4)$$

Hence, \bar{v}^* is obtained from integrating the vorticity definition from the far field all the way to the cylinder surface

$$\frac{1}{r} \frac{\partial}{\partial r} (r \bar{v}^*) = \frac{1}{r} \frac{\partial}{\partial \theta} (\bar{u}^*) + \omega \quad (5.5)$$

Since ω is constant everywhere, an exact integration is possible resulting in

$$\bar{v}^* = -\omega (L - r \sin \theta) \sin \theta \quad (5.6)$$

The augmented potential equation is solved for the potential function with the no

penetration boundary condition at the solid surface

$$\frac{\partial \phi}{\partial n} = -\bar{u}^*|_{r=1} = -\omega (L - \sin \theta) \cos \theta \quad (5.7)$$

The streamlines are shown in fig(5.1) for an incoming linear shear flow with constant vorticity $\frac{\omega R}{U_\infty} = 5$. The velocity at the wake centerline, obtained using the present method, is compared in fig(5.2) with that obtained using a stream function/vorticity formulation. Figs (5.3) and (5.4) show a comparison with the analytical solution for the variation of the stagnation point and the reattachment angle with vorticity.

5.1.2 Transonic Flow

Compressibility effects are examined by simulating transonic flow over a cylinder at $M_\infty = 0.5$. This test case is characterized by the presence of a strong curved shock on the surface of the cylinder. For the potential flow simulation, the flow downstream of the shock remains isentropic and irrotational. However, when entropy and vorticity variations are included for an Euler simulation, the shock becomes weaker due to entropy generation and its location moves further upstream as shown in fig(5.6). The strong entropy gradients result in vorticity generation which in turn leads to inviscid separation and a recirculating region in the wake of the cylinder as shown in fig (5.5). The size of the inviscid separation bubble calculated using the present method is in good agreement with that calculated in [86] using a standard Euler solver. A comparison of the Mach contours for the potential and rotational flow simulations is given in fig (5.7), where an inviscid wake is generated in the rotational flow case due

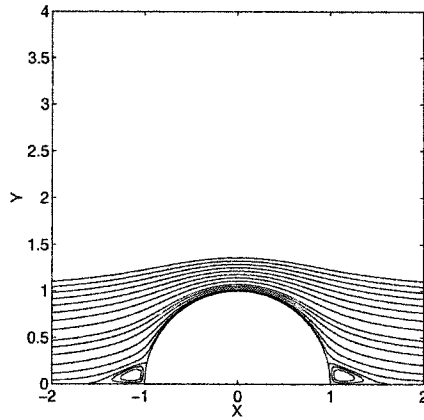


Figure 5.1: Streamlines for incompressible inviscid shear flow over a cylinder ($\frac{\omega R}{U_o} = 5$)

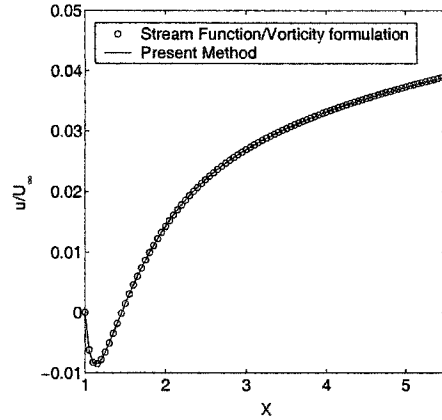


Figure 5.2: Wake centerline velocity for incompressible inviscid shear flow over a cylinder ($\frac{\omega R}{U_o} = 5$)

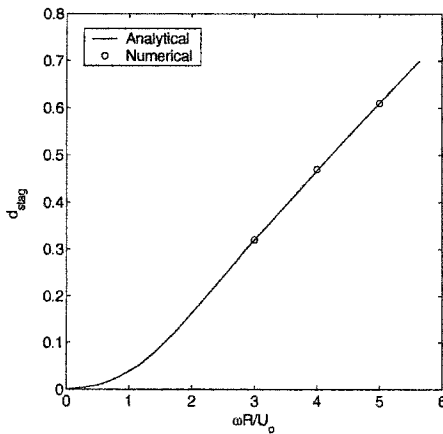


Figure 5.3: Effect of incoming vorticity on the inviscid separation length for incompressible inviscid shear flow over a cylinder

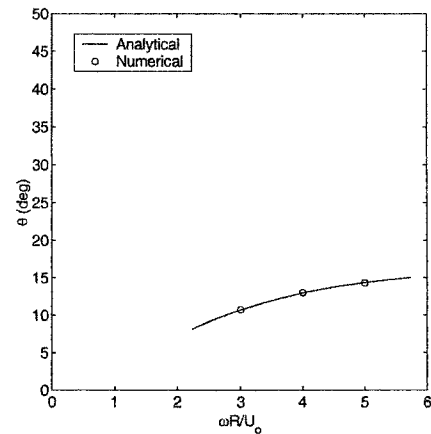


Figure 5.4: Effect of incoming vorticity on the reattachment angle for incompressible inviscid shear flow over a cylinder

to the total pressure loss encountered at the shock.

5.1.3 Supersonic Flow

Three cases are considered in the supersonic region for ($M_\infty = 1.7, 2.0, 2.3$). A comparison of the Mach contours for potential and rotational flows for one of the cases ($M_\infty = 2.0$) is given in fig(5.8). The entropy contours for ($M_\infty = 2.0$) are plotted in fig(5.9) while a comparison of the sonic line structure and location for the three rotational flow cases ($M_\infty = 1.7, 2.0, 2.3$) is given in fig(5.10). The potential flow simulations for all three cases result in bow shocks that are much stronger and located further downstream when compared with experimental data from [94]. However, the rotational flow simulations accurately predict the bow shock standoff distance and the shock strength at the symmetry line as shown in figs(5.11) and (5.12) respectively.

Additional results for transonic and supersonic inviscid shear flows using the present formulation are available in [95].

5.2 Viscous Incompressible Flows Over a Cylinder

Let's consider first the inviscid incompressible flow past a circular cylinder. As mentioned above, steady inviscid incompressible flows over a cylinder can be described by potential functions, obtained analytically as solutions of Laplace equation via superposition. The streamlines of the analytical solutions are plotted in fig(5.13) for typical cases of potential flows over a cylinder with and without rotation or suction. In the following, viscous incompressible flows over a cylinder with and without rotation

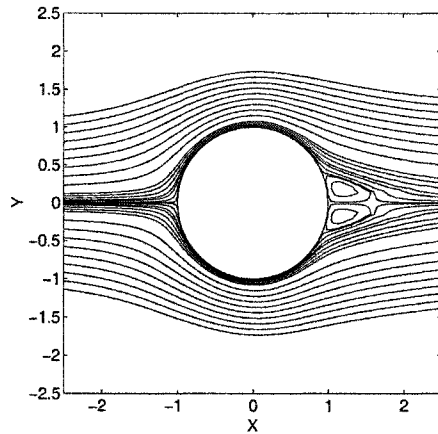


Figure 5.5: Streamlines for inviscid rotational flow over a cylinder ($M_\infty = 0.5$)

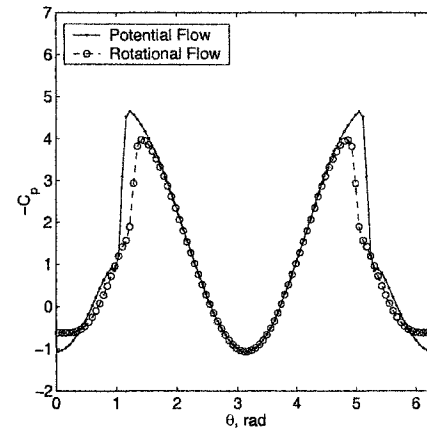
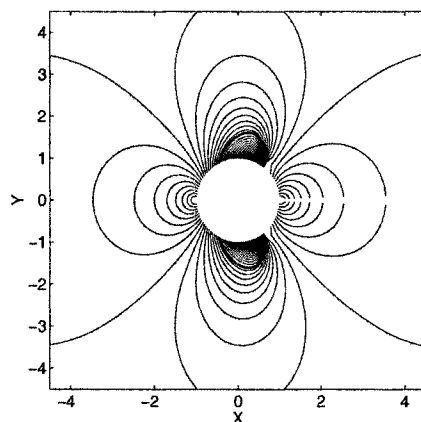
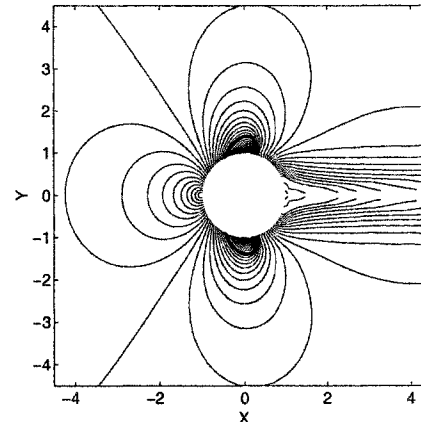


Figure 5.6: Surface pressure distribution for inviscid flow over a cylinder ($M_\infty = 0.5$)



Potential Flow



Rotational Flow

Figure 5.7: Mach contours for inviscid transonic flow over a cylinder ($M_\infty = 0.5$)

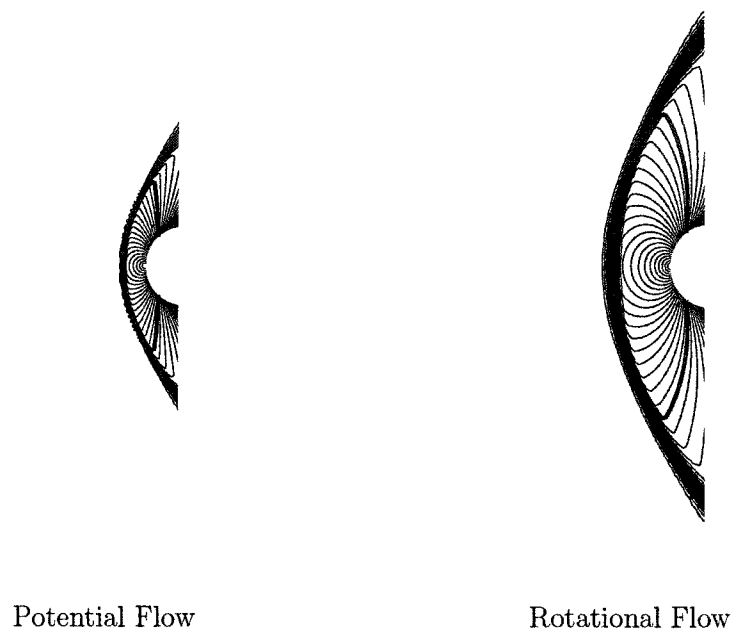


Figure 5.8: Mach contours for inviscid supersonic flow over a cylinder ($M_\infty = 2.0$)

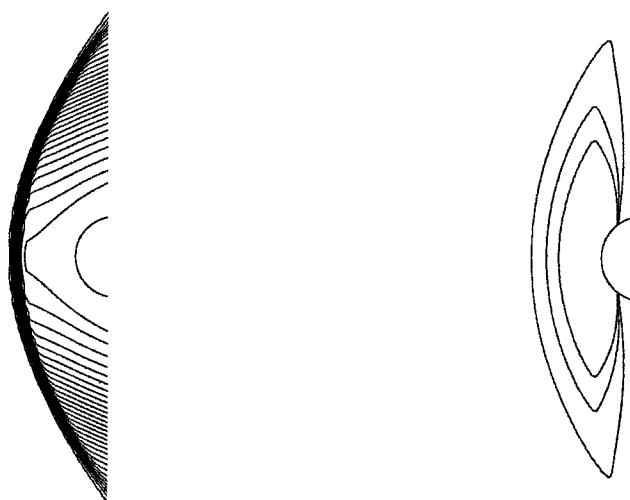


Figure 5.9: Entropy contours for inviscid rotational flow over a cylinder ($M_\infty = 2.0$)

Figure 5.10: Sonic lines for inviscid rotational flow over a cylinder ($M_\infty=1.7$, 2.0 and 2.3)

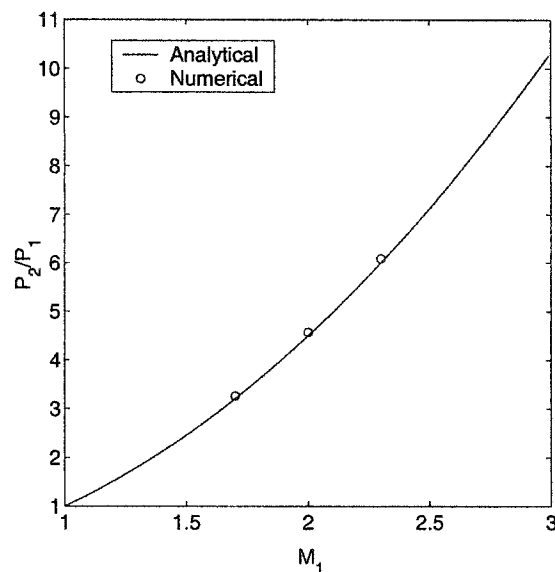


Figure 5.11: Pressure jump across the bow shock at the symmetry line

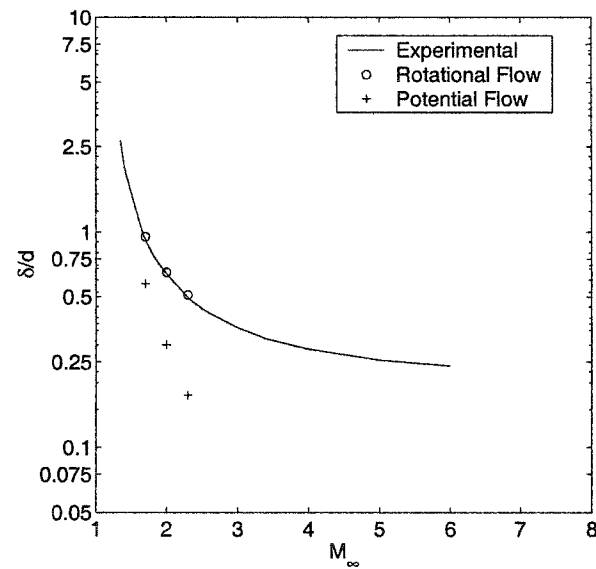


Figure 5.12: Standoff distance for the bow shock in front of a circular cylinder

and/or suction are simulated using the present formulation.

5.2.1 Flow over a stationary cylinder

For low Reynolds numbers, the viscous flow over a cylinder is steady and the length of the separation bubble increases linearly with Reynolds number, see fig(5.14). In these figures, the streamlines are calculated from the velocity components after the calculations converge. The results of the present formulation are in good agreement with experimental results available in [89] as shown in fig(5.15). As the Reynolds number increases, the flow becomes unsteady due to vortex shedding.

5.2.2 Flow over a rotating cylinder

For high rotation rates ($\alpha = \frac{\Omega R}{U_\infty}$), the viscous layer is wrapped around the cylinder with almost an inviscid potential flow in the outer region. To calculate the far field boundary condition for the potential function, the circulation is estimated using the Kutta-Joukowski theorem

$$\frac{L}{b} = -\rho_\infty U_\infty \Gamma \quad (5.8)$$

which represents, in fact, a balance of momentum in the direction normal to the flow. The lift is calculated by integrating the surface pressure and shear stresses.

$$C_{L_{total}} = C_{L_P} + C_{L_\tau} \quad (5.9)$$

where C_{L_P} and C_{L_τ} are the pressure and shear stress contributions to the lift

coefficient respectively (a similar approach was adopted by Thomas and Salas [96] for their Euler calculations of transonic flows). The effect of rotation rate on the lift coefficient is shown in fig(5.16) for $Re = 30$, including comparisons with standard Navier-Stokes calculations [97] and with potential flow theory ($C_L = 2\pi\alpha$). From fig (5.16), it is clear that the shear stress contribution to the lift coefficient is very small in comparison with the pressure contribution. In fig(5.17), the effect of Reynolds number on the lift coefficient, for $\alpha = 6$, is shown. The streamlines and the pressure contours for typical cases are given in figs(5.18) and (5.19) respectively. A slight lack of symmetry is noticed due to the viscous effect, particularly for the low Reynolds number case ($Re = 30$). For the high Reynolds number case ($Re = 200$), the present results as well as the results of Navier-Stokes calculations [98] are consistent with those of Glauert's asymptotic analysis [99] for two dimensional flows. It is worth noting that experiments with finite length cylinders result in lower lift coefficients due to three dimensional effects, depending on the end conditions.

5.2.3 Flow over a cylinder with suction

Suction is used to control separation, see for example [100]-[101]. Streamlines and pressure distributions for flows at different Reynolds numbers, with different uniform suction values V_s are shown in figs (5.20) and (5.21). An interesting conclusion from the numerical simulations is that as the Reynolds number increases, smaller suction rates are required to prevent flow separation. A similar behavior was reported in [101] for a slightly different configuration, where suction control is only applied in the rear

part of the cylinder.

5.2.4 Flow over a rotating cylinder with suction

Combining rotation and suction, the flow pattern is more complicated. Streamlines and pressure contours are given in fig(5.22) for potential and viscous flows ($Re = 30$).

At higher Reynolds number, the outer flow region must be allowed to include small vorticity in order to have a unique solution as indicated in [102]. Matching potential flow with a periodic boundary layer leads to nonunique solutions. The numerical simulation suffers in this case of convergence difficulties where the residuals are locked at a certain level and do not decrease with iterations.

It is worth noting that to plot the streamlines for all the above cases, a simple integration of the formula

$$d\psi = \frac{\partial \psi}{\partial r} dr + \frac{1}{r} \frac{\partial \psi}{\partial \theta} r d\theta = \bar{u} r d\theta - \bar{v} dr \quad (5.10)$$

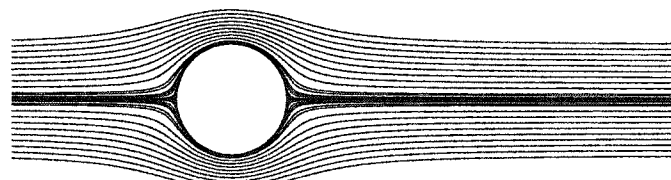
is used, where \bar{u} and \bar{v} are the velocity components in the r and θ directions respectively. For the stationary and rotating cylinder cases, ψ is zero on the surface of the cylinder and by integrating the formula, ψ could be found everywhere in the flow field. For the case of a cylinder with suction, ψ is discontinuous and the streamline, across which ψ jumps, is the wake centerline, being known a priori from symmetry considerations. Hence, the same simple integration method can again be used to find ψ everywhere in the field.

However, for the case of the rotating cylinder with suction, the streamline across

which ψ jumps is not known a priori and an alternative method for plotting the streamlines has to be considered. An equation for the convection of a scalar quantity C , which remains constant along a streamline, is solved for this case.

$$\bar{u} \frac{\partial C}{\partial r} + \frac{\bar{v}}{r} \frac{\partial C}{\partial \theta} = 0 \quad (5.11)$$

Hence, the streamlines can be detected as shown in fig(5.22). Notice that the jump in C is captured in few points due to numerical dissipation. The contours of the stream function based on equation(5.10), with the jump in ψ enforced along the $\theta = 0$ line, are also included in fig(5.22) for the sake of comparison.



Stationary cylinder

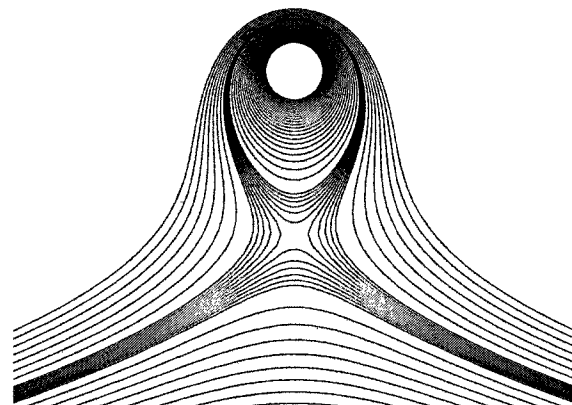
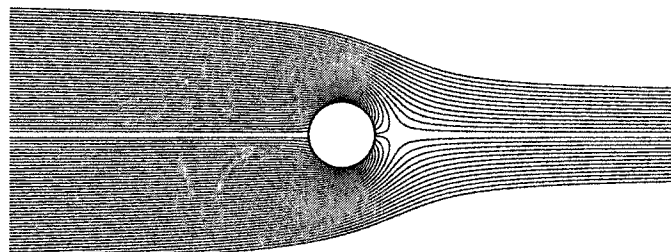
Rotating cylinder ($\alpha = 6$)Cylinder with suction ($V_s = 0.9$)

Figure 5.13: Streamlines for incompressible potential flows over a cylinder with and without rotation and/or suction

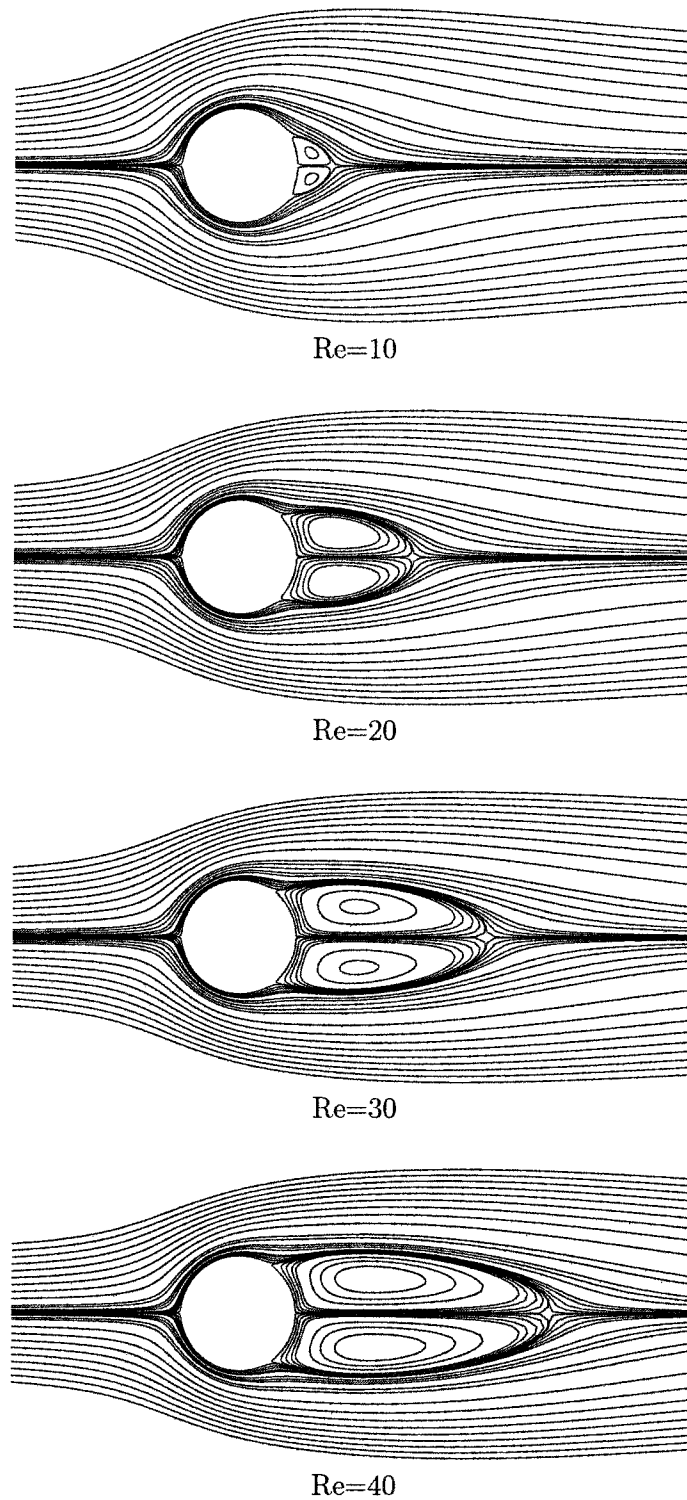


Figure 5.14: Streamlines for incompressible viscous flow over a cylinder at different Reynolds numbers

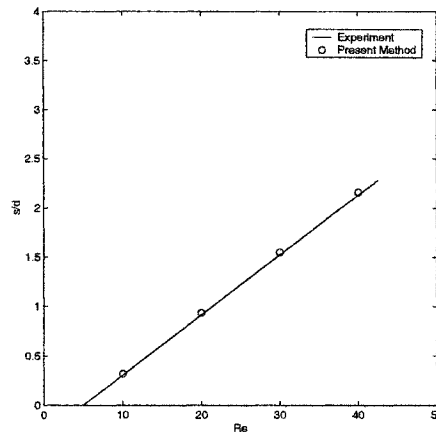


Figure 5.15: Effect of Reynolds number on separation length for incompressible viscous flow over a cylinder

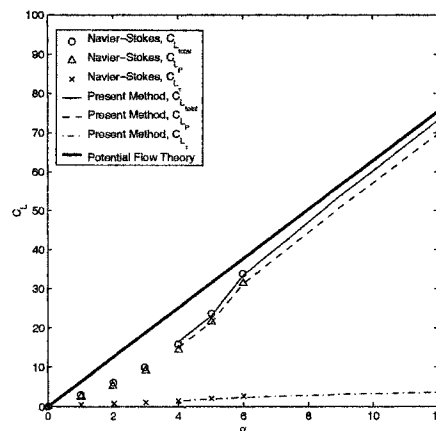


Figure 5.16: Effect of rotation rate on lift coefficient for incompressible viscous flow over a rotating cylinder at $\text{Re}=30$

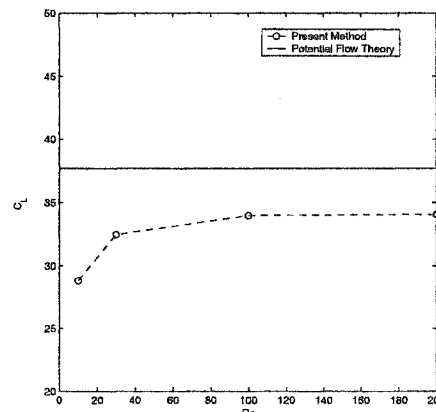


Figure 5.17: Effect of Reynolds number on lift coefficient for incompressible viscous flow over a rotating cylinder at $\alpha = 6$

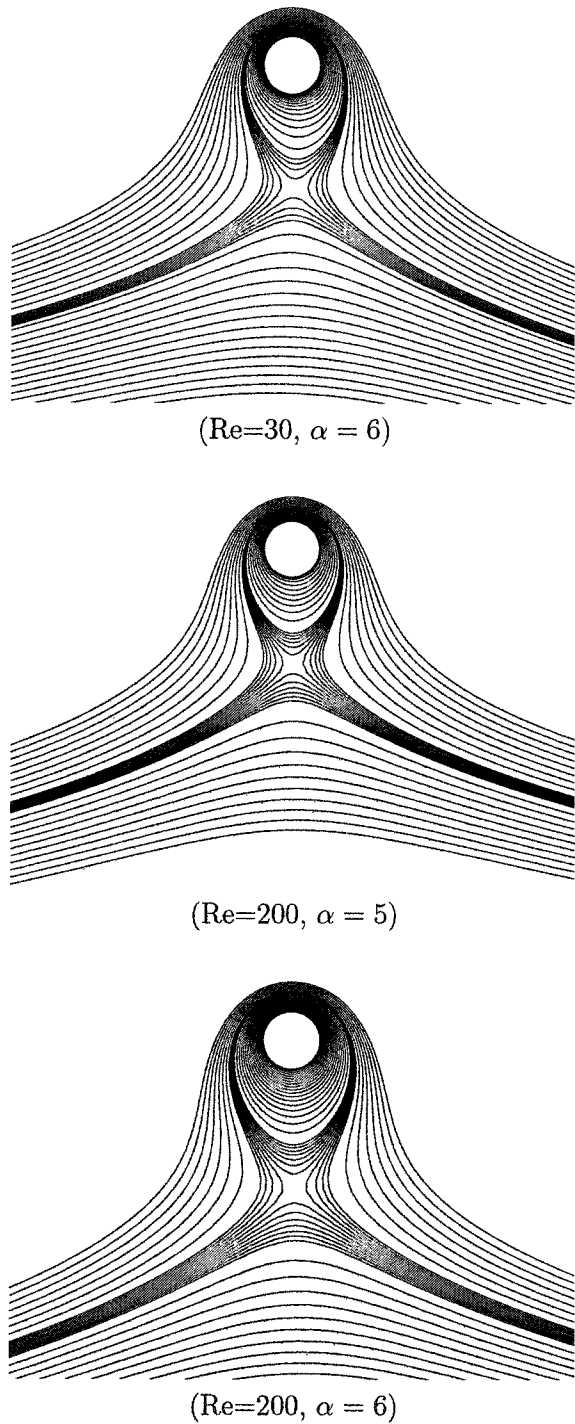
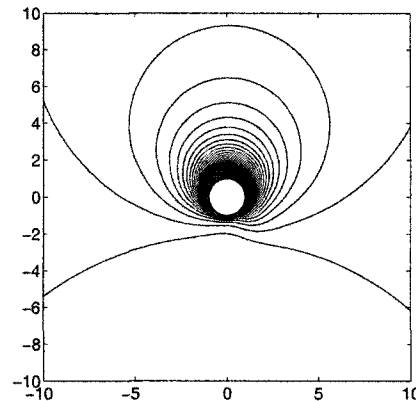
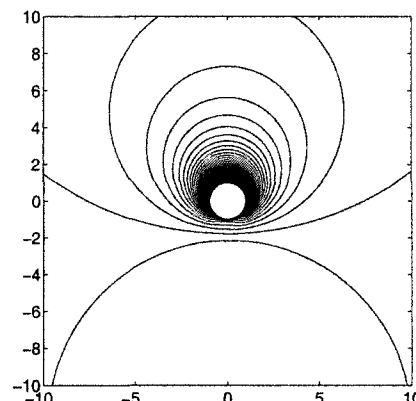


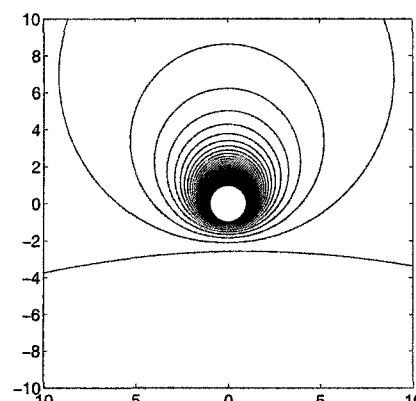
Figure 5.18: Streamlines for incompressible viscous flow over a rotating cylinder
at different Reynolds numbers and rotation rates



($\text{Re}=30, \alpha = 6$)

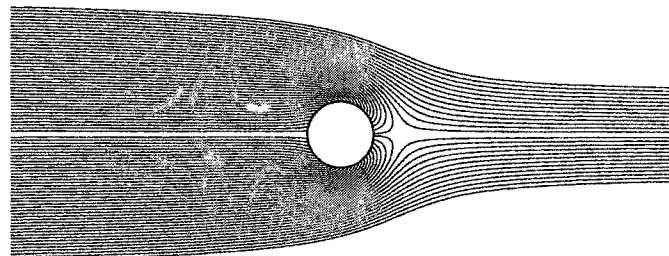


($\text{Re}=200, \alpha = 5$)

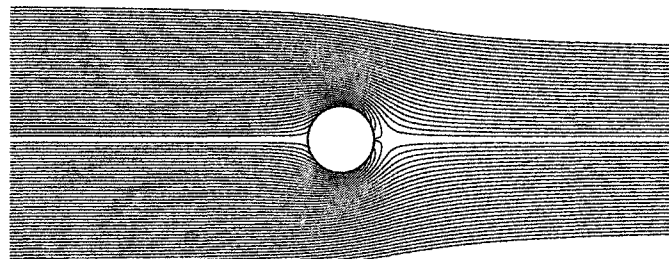


($\text{Re}=200, \alpha = 6$)

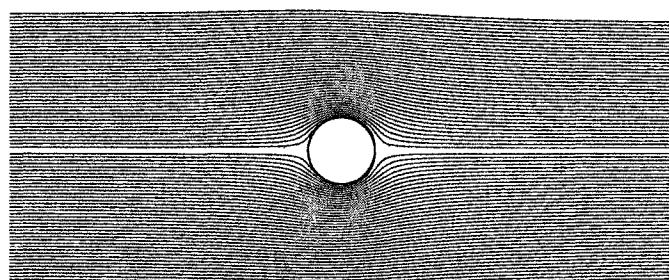
Figure 5.19: Pressure contours for incompressible viscous flow over a rotating cylinder at different Reynolds numbers and rotation rates



($Re = 30, V_s = 0.9$)



($Re = 200, V_s = 0.45$)



($Re = 1 \times 10^4, V_s = 0.1$)

Figure 5.20: Streamlines for incompressible viscous flow over a cylinder with suction at different Reynolds numbers and suction rates

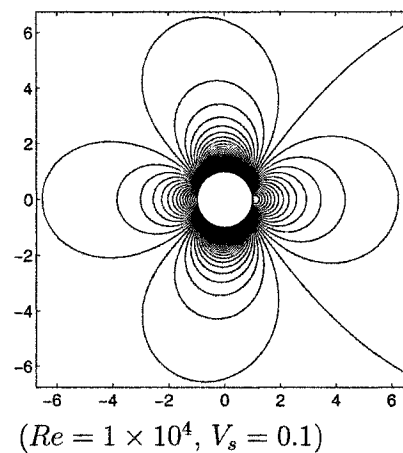
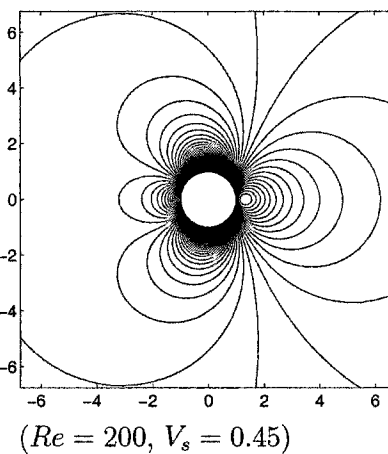
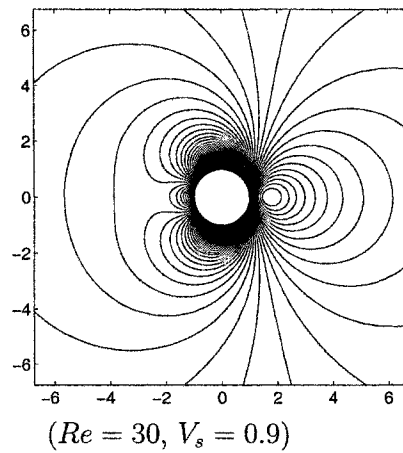


Figure 5.21: Pressure contours for incompressible viscous flow over a cylinder with suction at different Reynolds numbers and suction rates

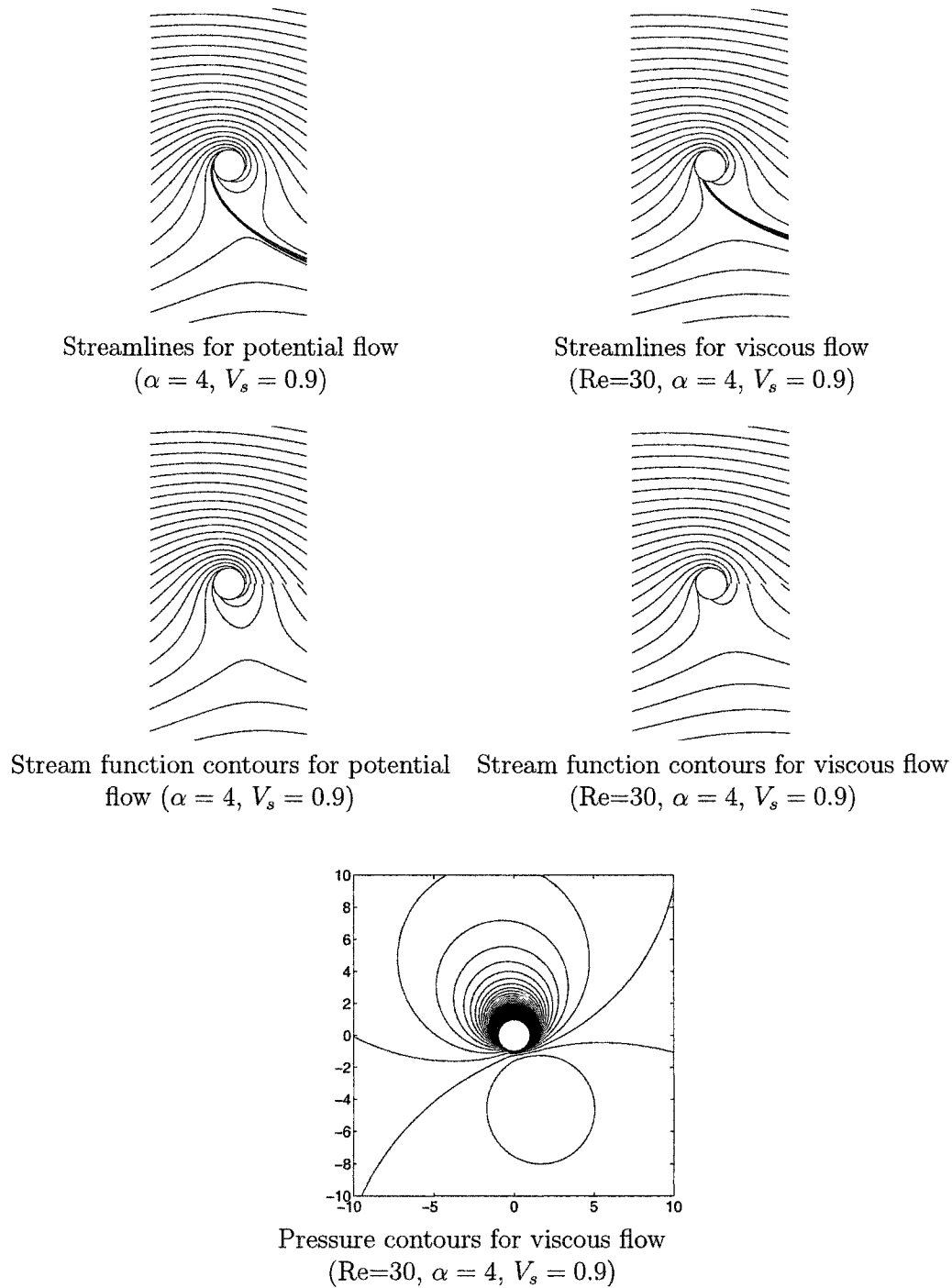


Figure 5.22: Incompressible viscous flow over a rotating cylinder with suction
($Re=30, \alpha = 4, V_s = 0.9$)

CHAPTER 6

INVISCID AND VISCOUS FLOWS OVER AIRFOILS

In this chapter, inviscid and viscous flows over NACA0012 airfoil are simulated. The test cases are chosen such that they span the whole Mach number range from incompressible to supersonic flows. For the viscous test cases, only laminar flows are considered. A (281×81) structured C-grid is generated around the airfoil using algebraic methods. The generated grid is shown in fig(6.1).

6.1 Inviscid Flows Over an Airfoil

Transonic flow over NACA0012 airfoil is simulated for a symmetric zero angle of attack case at $M_\infty = 0.86$. Pressure contours for the potential and rotational flow simulations are given in fig (6.2), while the surface pressure distribution is plotted in fig(6.3) showing the effect of entropy and vorticity on the shock location and strength. The same test case was simulated in [103] using FLO 52-S, a well documented Euler solver. The surface pressure distributions obtained using the present method and using FLO 52-S are in good agreement as shown in fig(6.3).

Similar results are presented for a lifting transonic case at $M_\infty = 0.75$ and $\alpha = 2^\circ$

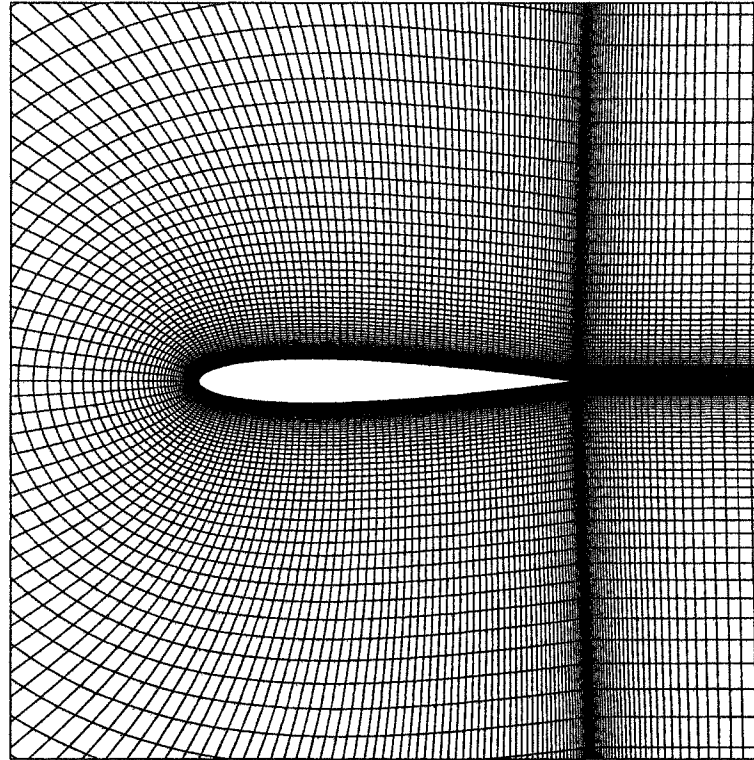


Figure 6.1: Structured C-Grid for NACA0012 Airfoil

in figs (6.4) and (6.5). The surface pressure distribution obtained using the present method is in good agreement with that obtained using standard Euler calculations [104] as evident from fig(6.5). The results for a second lifting transonic case at $M_\infty = 0.85$ and $\alpha = 1^\circ$ are given in figs(6.6) and (6.7).

Next supersonic free streams are considered. Numerical simulations at $M_\infty = 1.4$ for $\alpha = 0^\circ$ and $\alpha = 4^\circ$ are presented in figs (6.8)-(6.11). Notice the effect of entropy and vorticity on the bow shock stand off distance in both cases as evident from the pressure distribution along the axis.

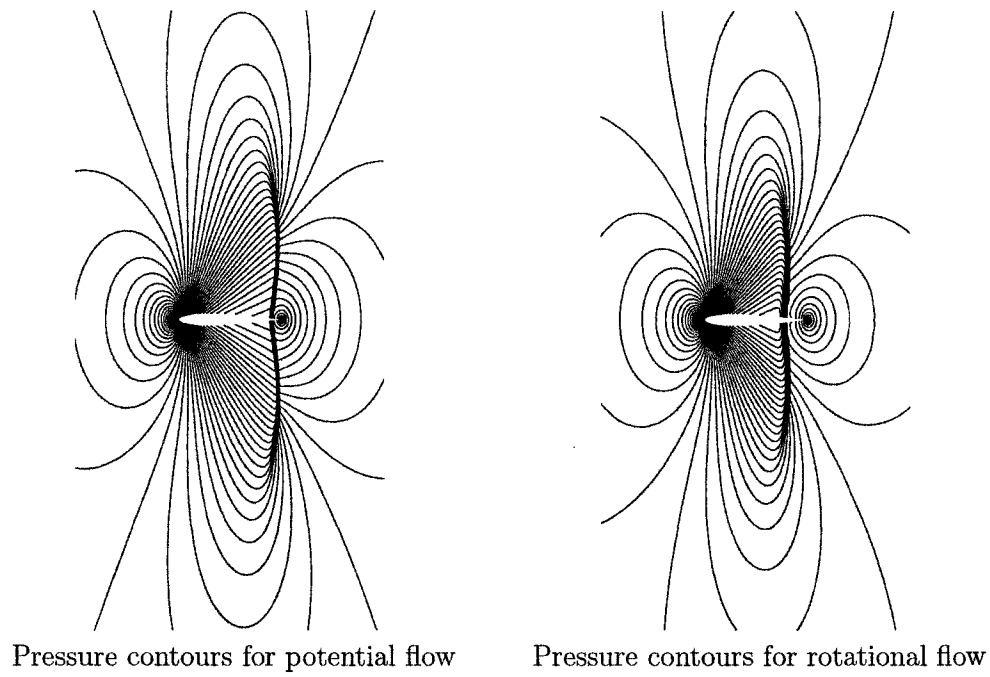


Figure 6.2: Inviscid flow over NACA0012 airfoil ($M_\infty = 0.86$, $\alpha = 0^\circ$)

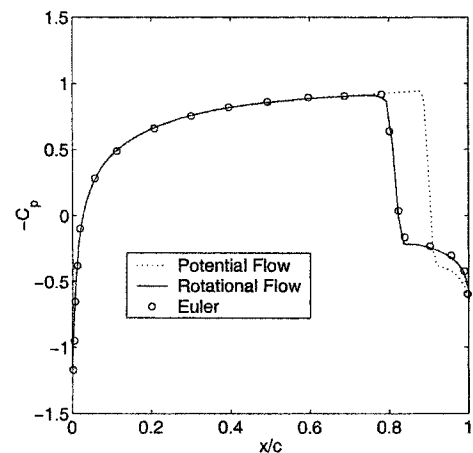


Figure 6.3: Surface pressure distribution for inviscid flow over NACA0012 airfoil ($M_\infty = 0.86$, $\alpha = 0^\circ$)

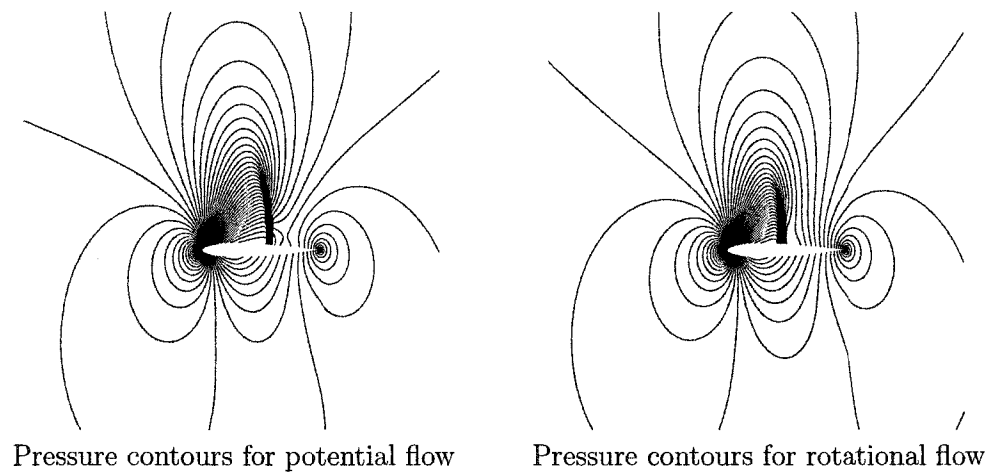


Figure 6.4: Inviscid flow over NACA0012 airfoil ($M_\infty = 0.75, \alpha = 2^\circ$)

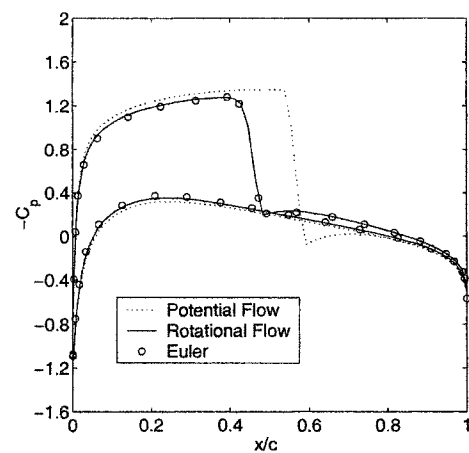


Figure 6.5: Surface pressure distribution for inviscid flow over NACA0012 airfoil ($M_\infty = 0.75, \alpha = 2^\circ$)

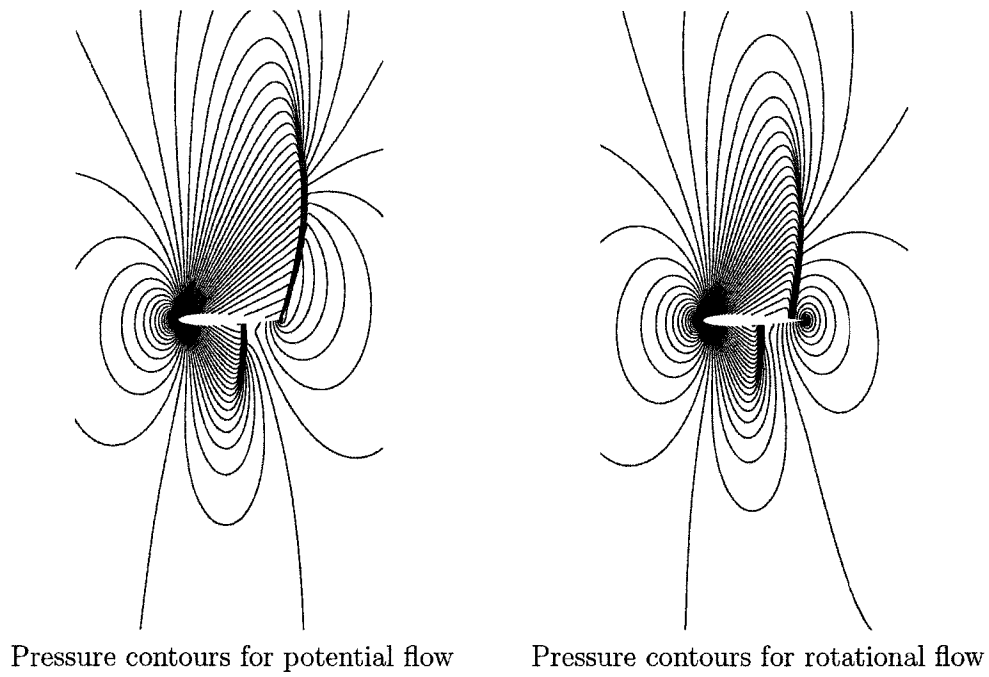


Figure 6.6: Inviscid flow over NACA0012 airfoil ($M_\infty = 0.85, \alpha = 1^\circ$)

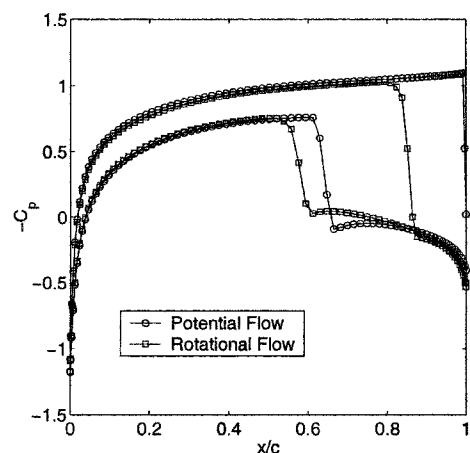


Figure 6.7: Surface pressure distribution for inviscid flow over NACA0012 airfoil ($M_\infty = 0.85, \alpha = 1^\circ$)

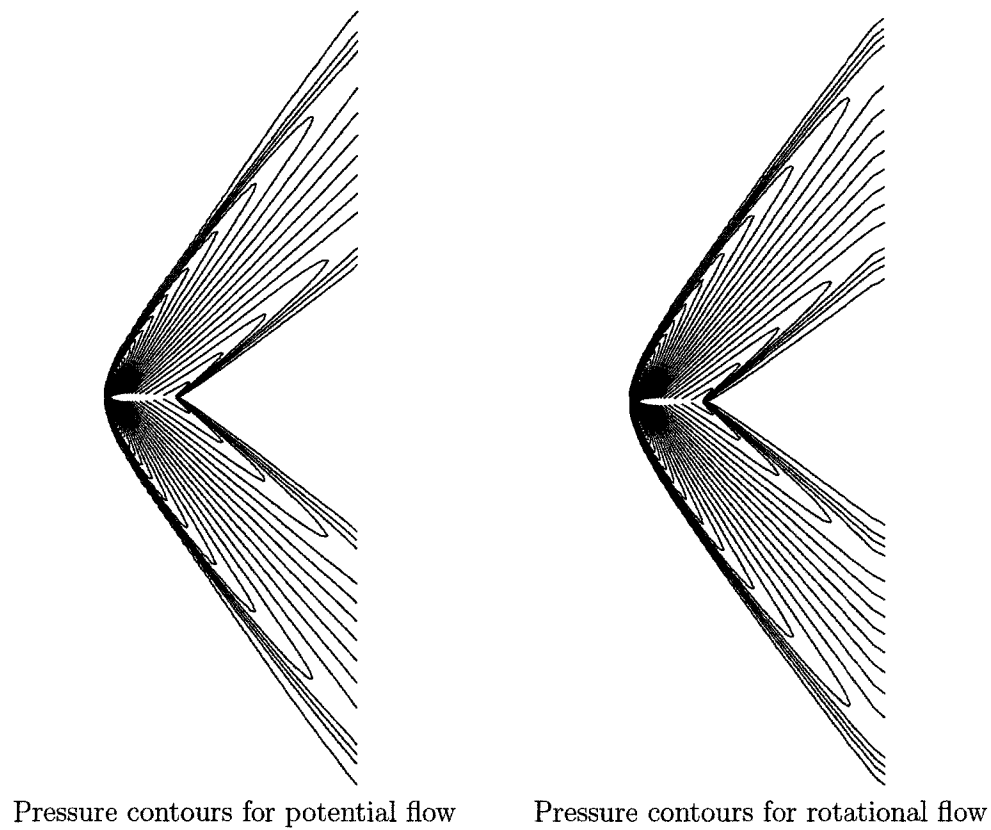


Figure 6.8: Inviscid flow over NACA0012 airfoil ($M_\infty = 1.4$, $\alpha = 0^\circ$)

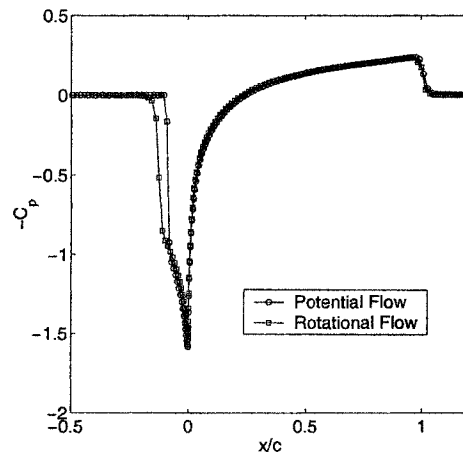


Figure 6.9: Surface pressure distribution for inviscid flow over NACA0012 airfoil ($M_\infty = 1.4$, $\alpha = 0^\circ$)

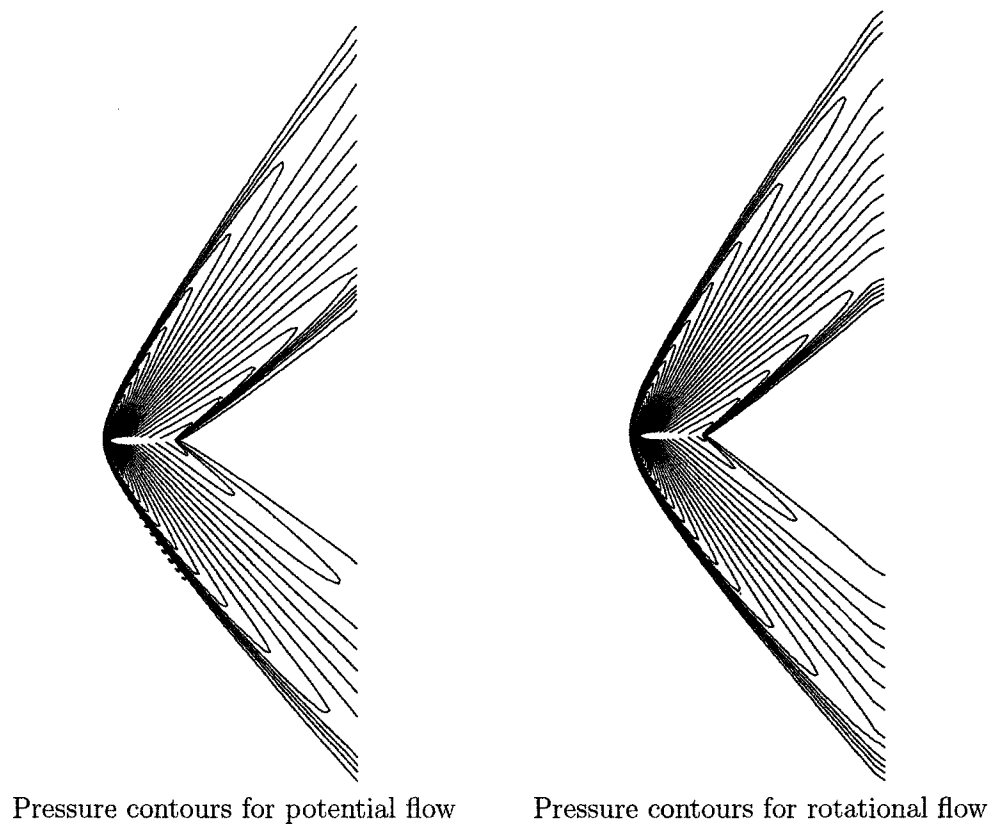


Figure 6.10: Inviscid flow over NACA0012 airfoil ($M_\infty = 1.4$, $\alpha = 4^\circ$)

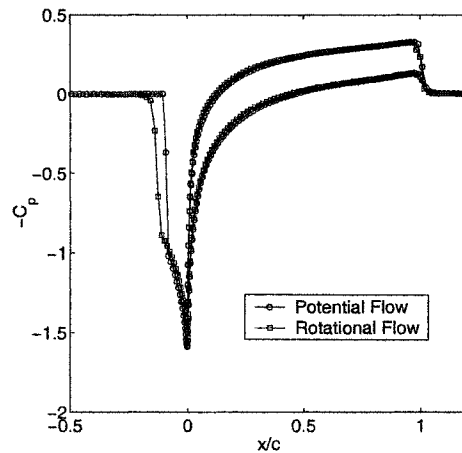


Figure 6.11: Surface pressure distribution for inviscid flow over NACA0012 airfoil ($M_\infty = 1.4$, $\alpha = 4^\circ$)

6.2 Viscous Flows Over an Airfoil

In the following, viscous flows over NACA0012 airfoil are considered. The two approaches of section (2.3.3) for evaluating the vorticity inside the viscous layers are applied and the results from the two approaches are compared to each other and to available Navier-Stokes calculations in the literature.

6.2.1 Evaluation of vorticity using first approach

Using the first approach for vorticity evaluation in the viscous layer, laminar flows over NACA0012 airfoil are simulated for a wide range of Mach and Reynolds numbers. In this approach, as described before, the normal component of the rotational velocity is chosen to be identically zero and hence, the tangential momentum equation is used to update the rotational velocity. Transonic viscous flow at $Re = 500$ for $M_\infty = 0.8$ and $M_\infty = 0.9$ at angles of attack $\alpha = 0^\circ$ and $\alpha = 10^\circ$ are considered first, where the results of the simulations are given in terms of the Mach contours, pressure contours and pressure distribution over the airfoil surface in figs (6.12)-(6.19). The same test cases were simulated in [105] using Overflow, a Navier-Stokes solver developed at NASA Ames [106]. The simulation results obtained using the present formulation are in good agreement with those of Overflow as can be seen from the comparison of the surface pressure distributions in figures (6.13),(6.15),(6.17) and (6.19), for all four cases.

Higher Reynolds numbers are considered next through a transonic case at $M_\infty = 0.85, Re = 2000$ and $\alpha = 0^\circ$, and a subsonic case at $M_\infty = 0.5, Re = 1 \times 10^4$

and $\alpha = 0^\circ$. Results for these two cases are given in figs (6.20)-(6.25). Standard Navier-Stokes calculation for the $M_\infty = 0.85$ case is available in [107] and for the $M_\infty = 0.5$ case is available in [108]. Again, the results of the present method are in good agreement with the standard Navier-Stokes calculations as can be seen from the comparison of the surface pressure distributions in figs(6.22) and (6.25). Notice that for the high Reynolds number cases, the boundary layer separates, even for a zero angle of attack. (For low Reynolds number cases ($Re = 500$) at zero angle of attack, the flow remains attached).

A supersonic viscous flow case at $M_\infty = 1.5$, $Re = 1 \times 10^4$ and $\alpha = 0^\circ$ is simulated next. Two sets of simulations are performed. In the first simulation, the viscous layer is coupled with rotational flow, hence allowing entropy and vorticity generation from curved shocks in the outer inviscid region. The Mach and pressure contours for this simulation are given in fig(6.26).

In the second simulation, the viscous layer is coupled with potential flow, hence ignoring entropy and vorticity generation from curved shocks in the outer inviscid region. A comparison of the surface pressure distributions resulting from the two simulations is given in fig(6.27), showing that both are basically similar except in estimating the pressure jump across the bow shock, where entropy and vorticity generation in the inviscid flow plays an important role in determining the shock strength and location. Notice that the pressure gradient over the airfoil for the supersonic flow case is a favourable pressure gradient, as evident from fig(6.27), which prevents boundary layer separation and helps in sustaining a laminar flow regime for

even higher Reynolds numbers. This is in contrast with the subsonic and transonic flow cases, where the presence of an adverse pressure gradient leads to boundary layer separation, even at moderate Reynolds numbers, which in turn leads to an early transition to turbulent flow.

Next, the incompressible flow limit is studied. Numerical results are obtained for viscous flows over NACA0012 airfoil at $M_\infty = 0.0, 0.1, 0.2$ with $\alpha = 10^\circ$ and $Re = 500$. In figures (6.28) and (6.29), the u-velocity contours and the surface pressure distributions are plotted for the three cases. The same rate of convergence was observed for incompressible and compressible flows. Moreover, no degeneration of accuracy is noticed for the incompressible flow case as can be seen from the comparison of the surface pressure distributions in fig(6.29).

6.2.2 Evaluation of vorticity using second approach

In this section, the second approach for vorticity evaluation in the viscous layer is applied where the x and y momentum equations are used to update the u^* and v^* components respectively. Some of the test cases simulated using the first approach are re-simulated using the second approach and a comparison of the two approaches is given in terms of the surface pressure and skin friction distributions.

The first case to be simulated using the second approach is the transonic viscous flow case at $M_\infty = 0.8$, $Re = 500$ and $\alpha = 0^\circ$. The Mach and pressure contours are given in fig (6.30). A comparison of the surface pressure and skin friction distributions obtained using both approaches is given in fig(6.31) showing that both approaches of

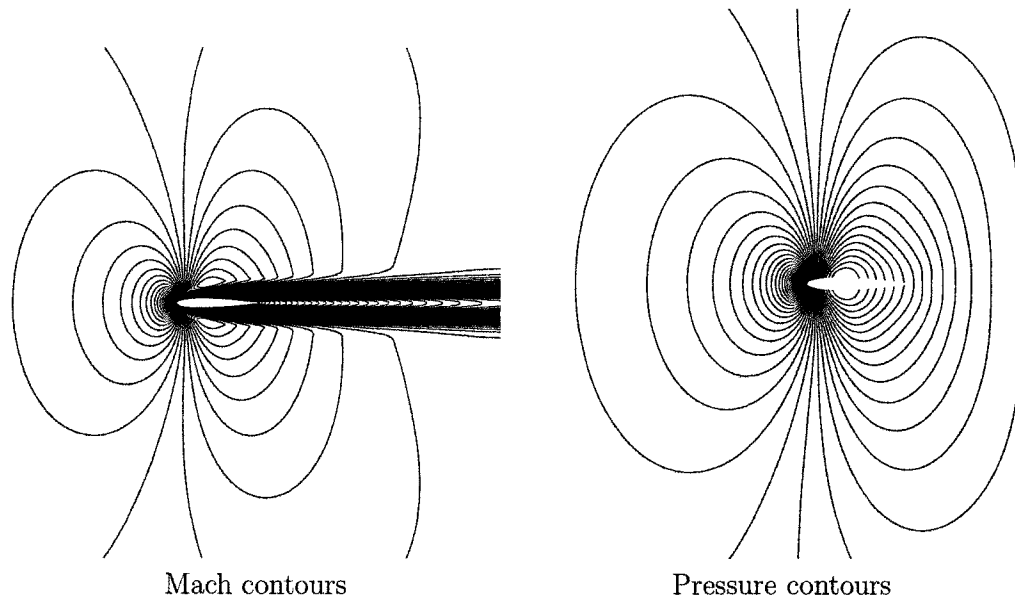


Figure 6.12: Viscous flow over NACA0012 airfoil using first approach
 $(M_\infty = 0.8, Re = 500, \alpha = 0^\circ)$

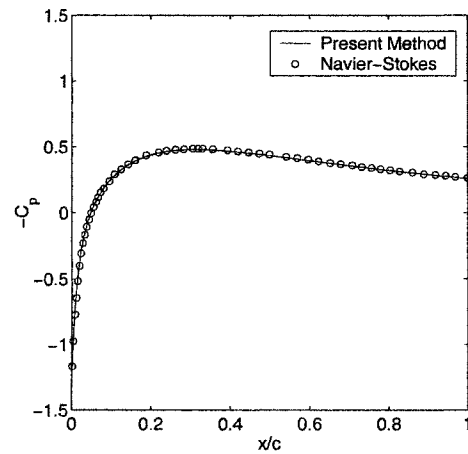


Figure 6.13: Surface pressure distribution for viscous flow over NACA0012 airfoil using first approach $(M_\infty = 0.8, Re = 500, \alpha = 0^\circ)$

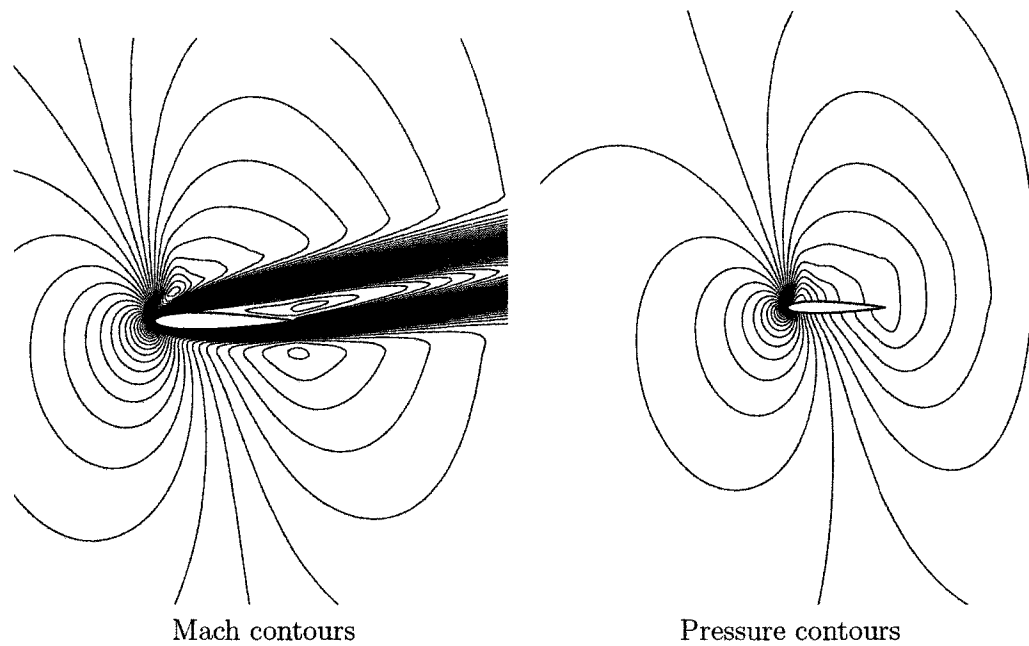


Figure 6.14: Viscous flow over NACA0012 airfoil using first approach
 $(M_\infty = 0.8, Re = 500, \alpha = 10^\circ)$

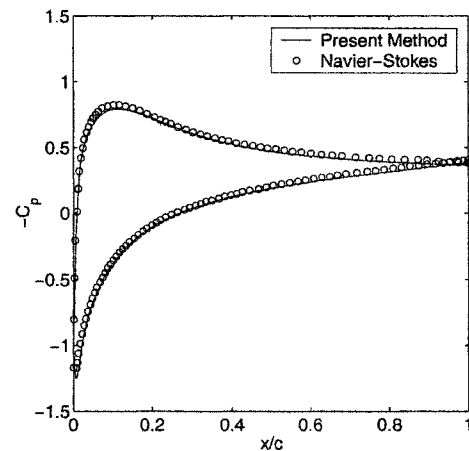


Figure 6.15: Surface pressure distribution for viscous flow over NACA0012 airfoil using first approach $(M_\infty = 0.8, Re = 500, \alpha = 10^\circ)$

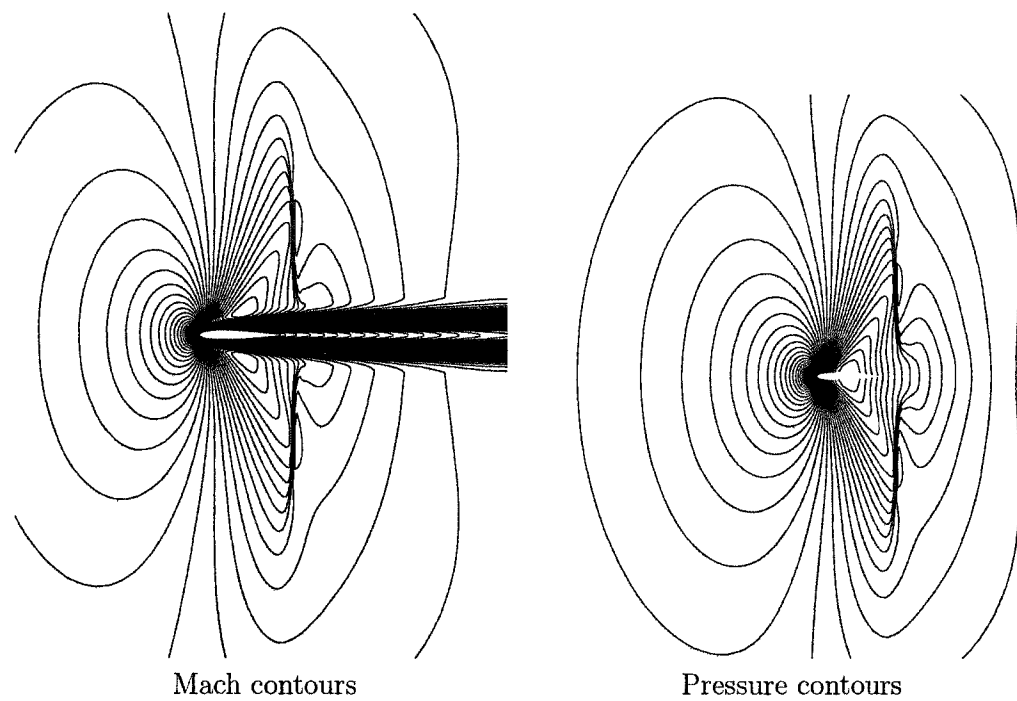


Figure 6.16: Viscous flow over NACA0012 airfoil using first approach
 $(M_\infty = 0.9, Re = 500, \alpha = 0^\circ)$

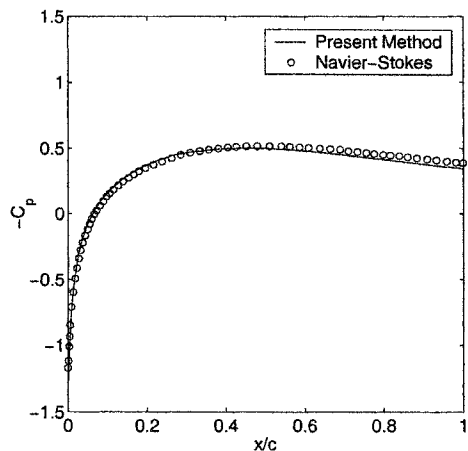


Figure 6.17: Surface pressure distribution for viscous flow over NACA0012 airfoil using first approach $(M_\infty = 0.9, Re = 500, \alpha = 0^\circ)$

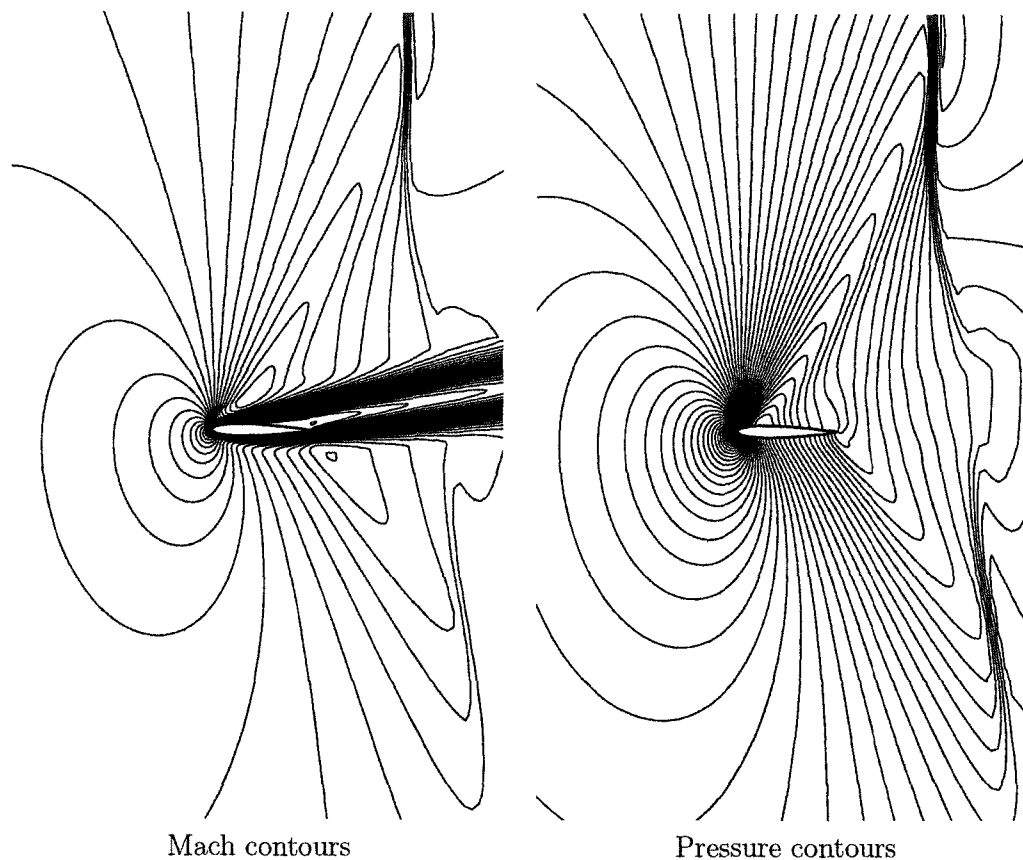


Figure 6.18: Viscous flow over NACA0012 airfoil using first approach
 $(M_\infty = 0.9, Re = 500, \alpha = 10^\circ)$

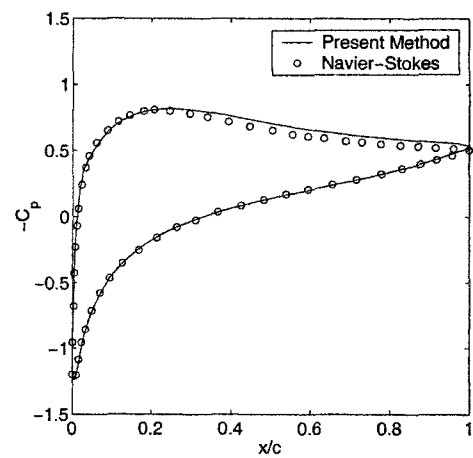


Figure 6.19: Surface pressure distribution for viscous flow over NACA0012 airfoil using first approach
 $(M_\infty = 0.9, Re = 500, \alpha = 10^\circ)$

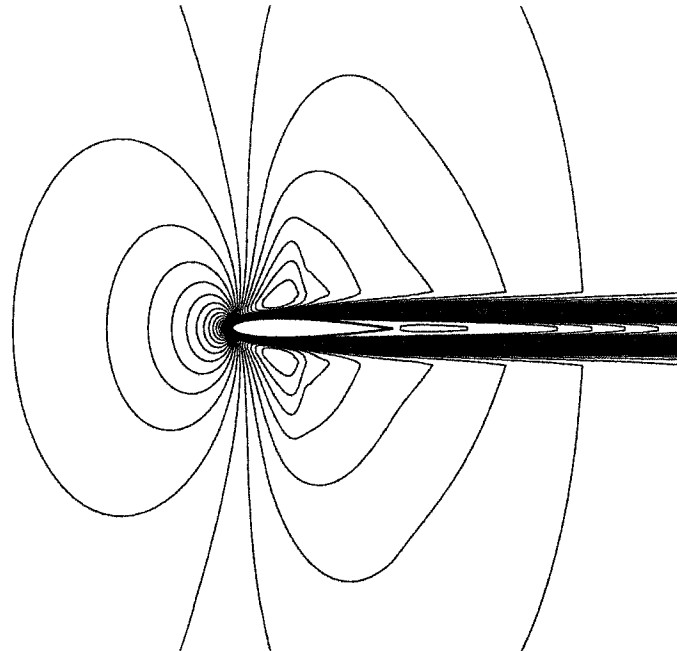


Figure 6.20: Mach Contours for viscous flow over NACA0012 airfoil using first approach ($M_\infty = 0.85$, $Re = 2000$, $\alpha = 0^\circ$)

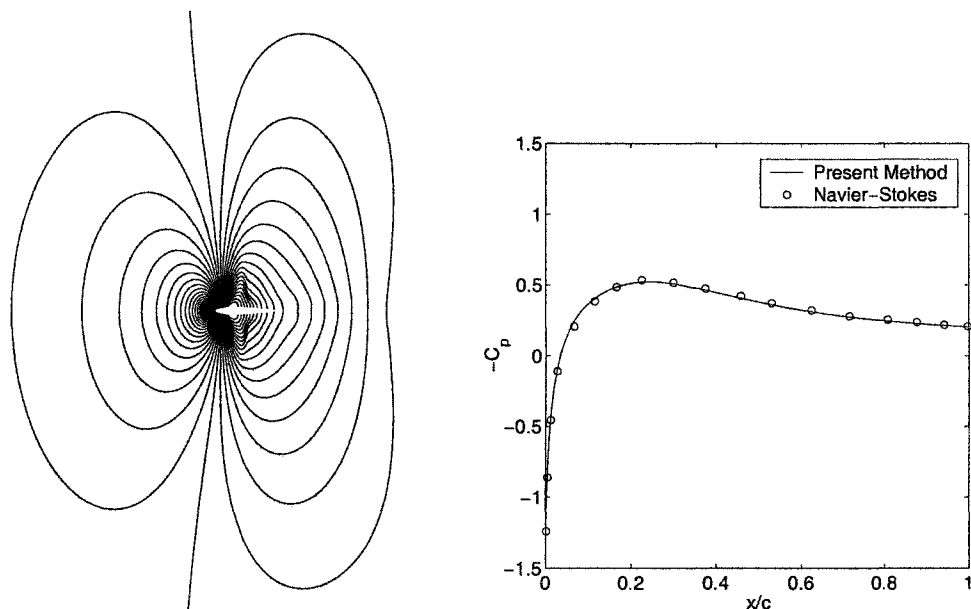


Figure 6.21: Pressure contours for viscous flow over NACA0012 airfoil using first approach ($M_\infty = 0.85$, $Re = 2000$, $\alpha = 0^\circ$)

Figure 6.22: Surface pressure distribution for viscous flow over NACA0012 airfoil using first approach ($M_\infty = 0.85$, $Re = 2000$, $\alpha = 0^\circ$)

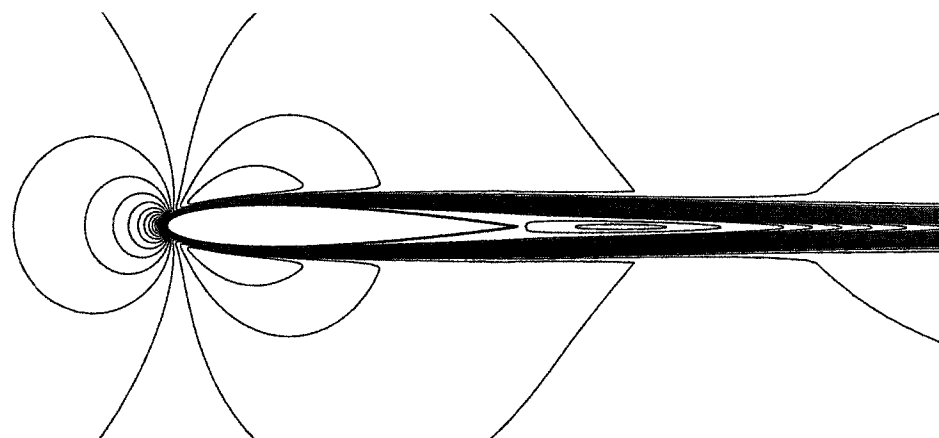


Figure 6.23: Mach Contours for viscous flow over NACA0012 airfoil using first approach ($M_\infty = 0.5$, $Re = 1 \times 10^4$, $\alpha = 0^\circ$)

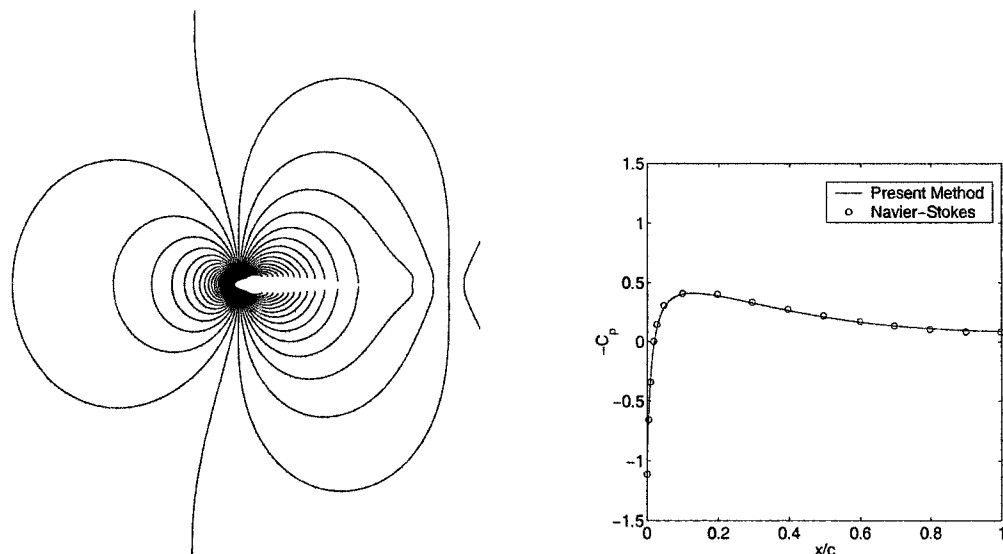


Figure 6.24: Pressure contours for viscous flow over NACA0012 airfoil using first approach ($M_\infty = 0.5$, $Re = 1 \times 10^4$, $\alpha = 0^\circ$)

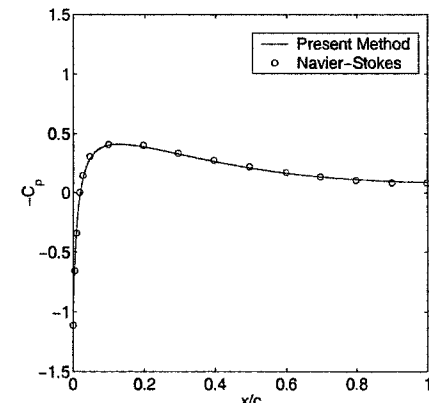


Figure 6.25: Surface pressure distribution for viscous flow over NACA0012 airfoil using first approach ($M_\infty = 0.5$, $Re = 1 \times 10^4$, $\alpha = 0^\circ$)

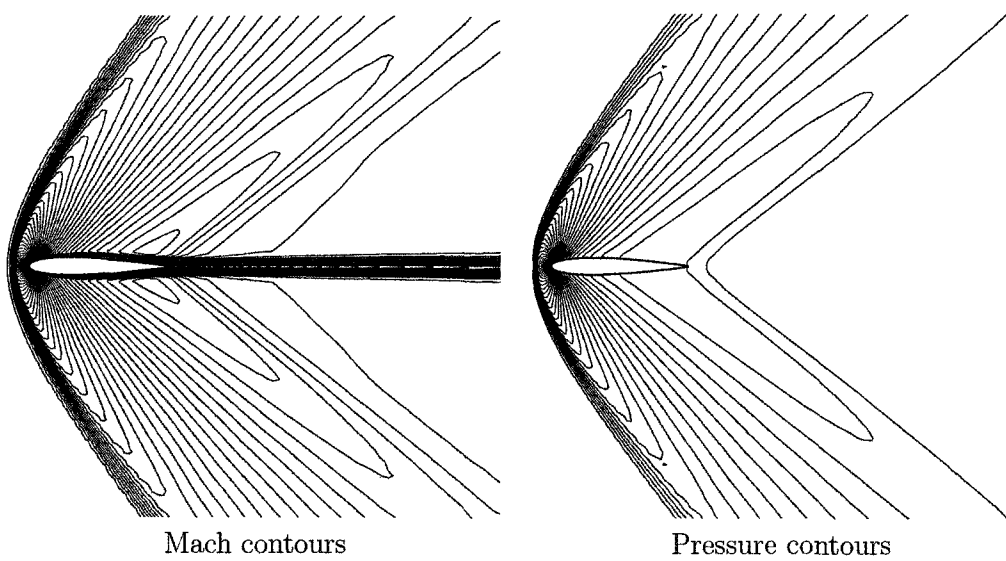


Figure 6.26: Viscous flow over NACA0012 airfoil using first approach
 $(M_\infty = 1.5, Re = 1 \times 10^4, \alpha = 0^\circ)$

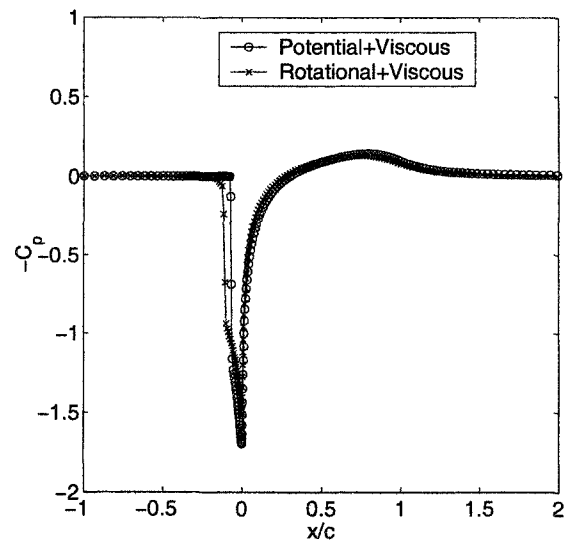


Figure 6.27: Surface pressure distribution for viscous flow over NACA0012 airfoil using first approach $(M_\infty = 1.5, Re = 1 \times 10^4, \alpha = 0^\circ)$

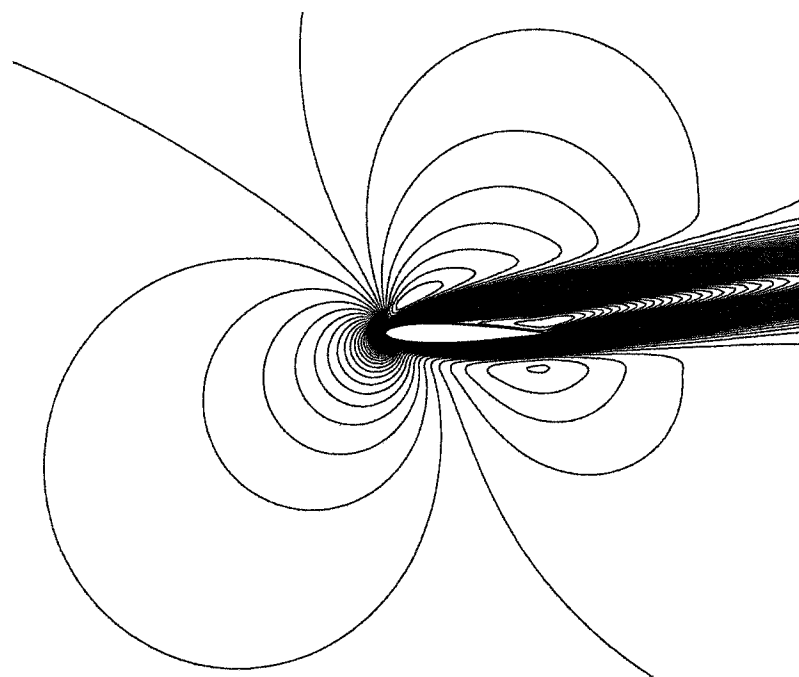


Figure 6.28: U contours for incompressible viscous flow over NACA0012 airfoil using first approach ($Re = 500$, $\alpha = 10^\circ$)

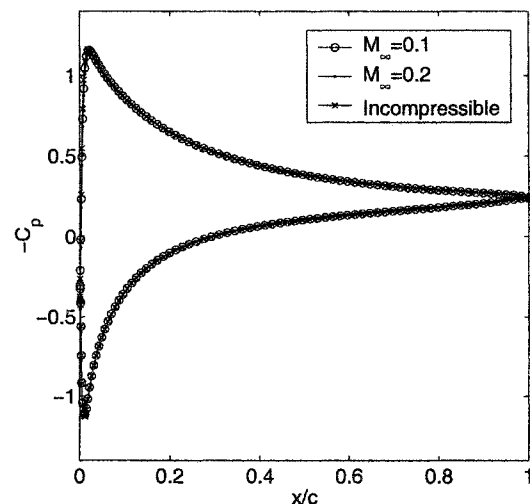


Figure 6.29: Surface pressure distribution for viscous flow over NACA0012 airfoil using first approach ($M_\infty = 0.0, 0.1, 0.2$, $Re = 500$, $\alpha = 10^\circ$)

vorticity evaluation result in basically similar results.

The second case is the transonic viscous flow at $M_\infty = 0.8$ and $Re = 500$ at an angle of attack $\alpha = 10^\circ$. The Mach and pressure contours are given in fig (6.32). Again, a comparison of the surface pressure and skin friction distributions in fig(6.33) reveals that both approaches of vorticity evaluation give identical results.

A supersonic viscous flow case at $M_\infty = 1.5$, $Re = 1 \times 10^4$ and $\alpha = 0^\circ$ is considered next. The Mach and pressure contours obtained using the second approach are given in fig(6.34). Again, both approaches give similar surface pressure and skin friction distributions as shown in fig(6.35).

Additional subsonic ($M_\infty = 0.5$, $Re = 1 \times 10^4$ and $\alpha = 0^\circ$)and transonic ($M_\infty = 0.9$, $Re = 500$ and $\alpha = 10^\circ$) flow cases are also considered using the second approach where the Mach and pressure contours are given in figs(6.36), (6.38) and (6.39). The comparison of the surface pressure distributions given in figs(6.37) and (6.40) further confirm that both approaches of vorticity evaluation yield identical results.

6.3 The Kutta Condition

For potential flows over a lifting airfoil, an infinite number of solutions are possible corresponding to different values of the circulation Γ . The Kutta condition identifies the right value of the circulation such that the flow leaves the trailing edge smoothly.

In the present work, a cut is defined along the wake starting from the trailing edge all the way to the outer boundary. Across the cut, the potential function is discontinuous, where the jump in the potential at the trailing edge is equal to the

circulation

$$\phi_{l_{TE}} - \phi_{u_{TE}} = \Gamma \quad (6.1)$$

where the subscripts l and u stand for the lower and upper sides of the cut respectively. The value of the circulation is updated from the Kutta condition during the iterative process by imposing equal velocities at both sides of the trailing edge. To guarantee that the pressure is continuous across the cut, the jump in potential at the trailing edge is held constant along the cut all the way to the outer boundary. Moreover, since the jump in potential is equal to the circulation in this case, it is used to calculate the far-field boundary condition.

For viscous flows, the right hand side of the augmented potential equation is a forcing function representing the displacement thickness effect on the outer potential flow. Hence, a modified potential function is obtained, with a jump at the trailing edge equal to the circulation over the augmented body due to displacement thickness effect. Therefore, the same strategy used for potential flows is readily extended to viscous flows, where the Kutta condition is applied such that the outer potential flow leaves the trailing edge of the augmented body smoothly. Furthermore, the jump in potential is kept constant along the wake cut all the way to the outer boundary and is also used to calculate the far-field boundary condition as in the potential flow case.

To further validate that the jump in the modified potential is equal to the circulation for viscous flows, another alternative method for calculating the circulation

is considered, where a box enclosing the airfoil and the total vorticity in the field is constructed and the circulation is calculated by evaluating a line integral over the box

$$\Gamma = \oint \vec{q} \cdot d\vec{l} \quad (6.2)$$

where $d\vec{l}$ is an incremental segment along the box. Numerical simulations confirmed that the circulation obtained by evaluating the line integral over the box is equal to the jump in the modified potential at the trailing edge.

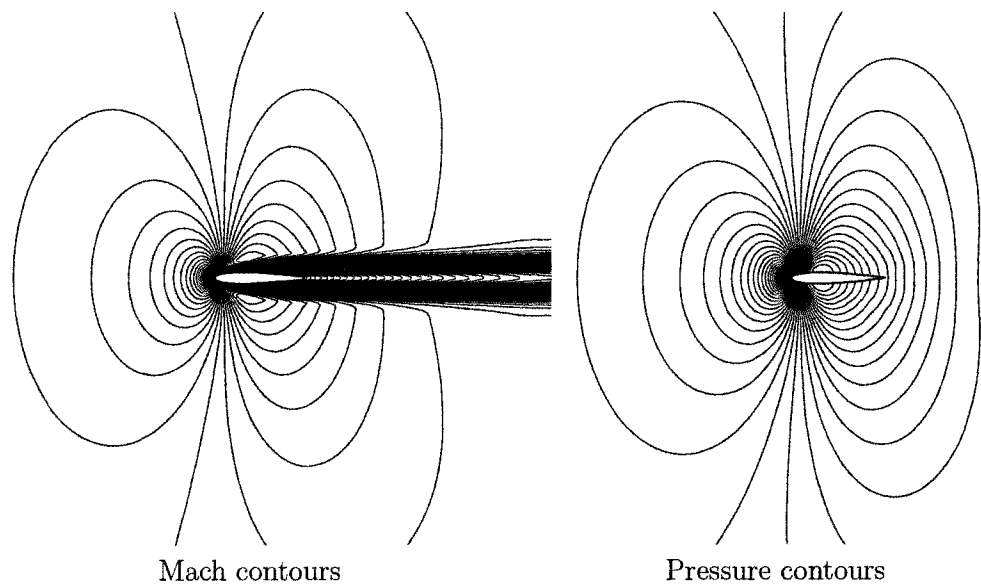


Figure 6.30: Viscous flow over NACA0012 airfoil using second approach
($M_\infty = 0.8$, $Re = 500$, $\alpha = 0^\circ$)

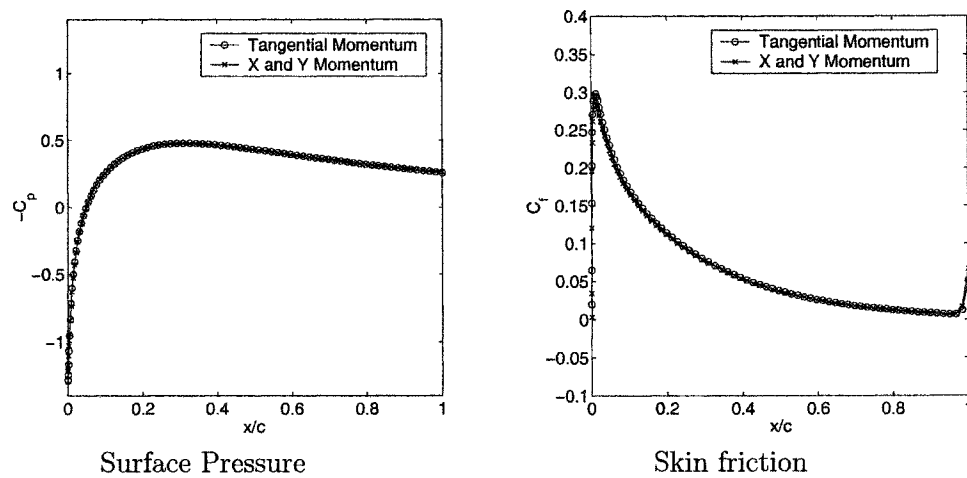


Figure 6.31: Skin friction and surface pressure distributions for viscous flow over NACA0012 airfoil ($M_\infty = 0.8$, $Re = 500$, $\alpha = 0^\circ$)

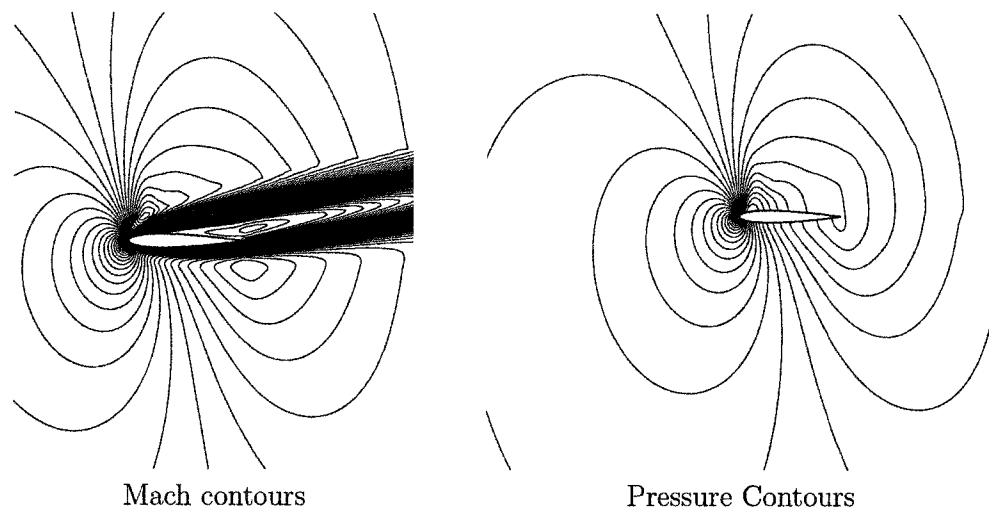


Figure 6.32: Viscous flow over NACA0012 airfoil using second approach
 $(M_\infty = 0.8, Re = 500, \alpha = 10^\circ)$

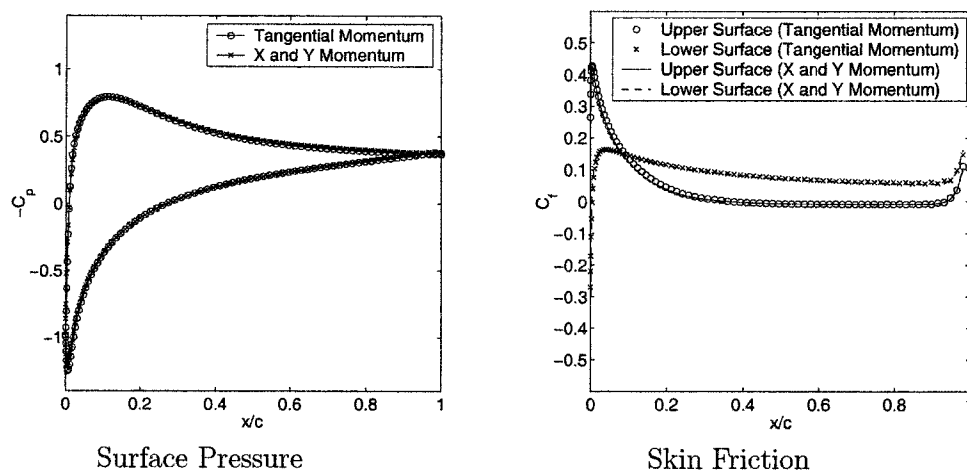


Figure 6.33: Skin friction and surface pressure distributions for viscous flow over NACA0012 airfoil $(M_\infty = 0.8, Re = 500, \alpha = 10^\circ)$

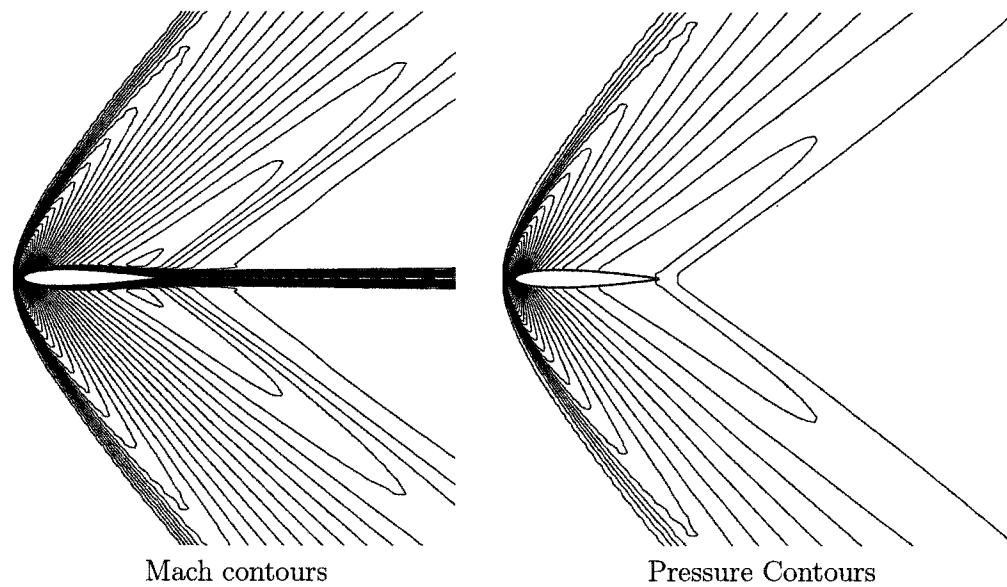


Figure 6.34: Viscous flow over NACA0012 airfoil using second approach
 $(M_\infty = 1.5, Re = 1 \times 10^4, \alpha = 0^\circ)$

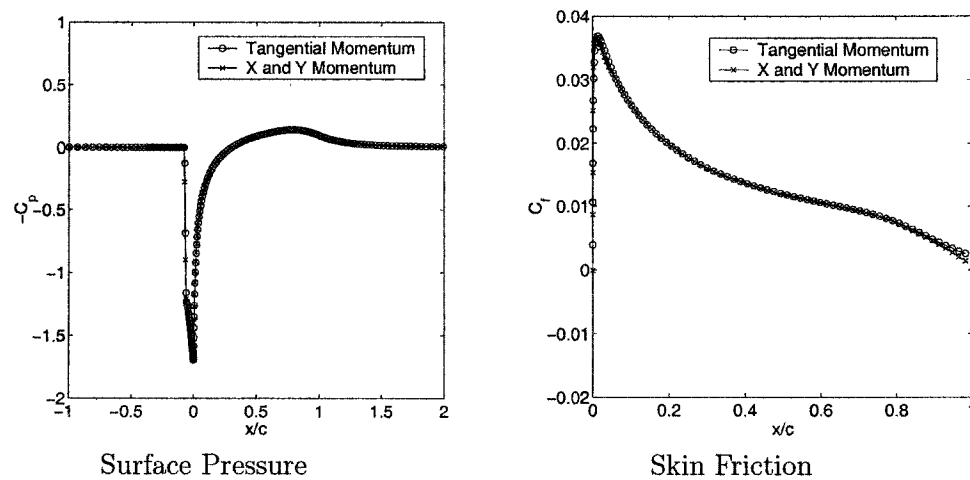


Figure 6.35: Skin friction and surface pressure distributions for viscous flow over NACA0012 airfoil $(M_\infty = 1.5, Re = 1 \times 10^4, \alpha = 0^\circ)$

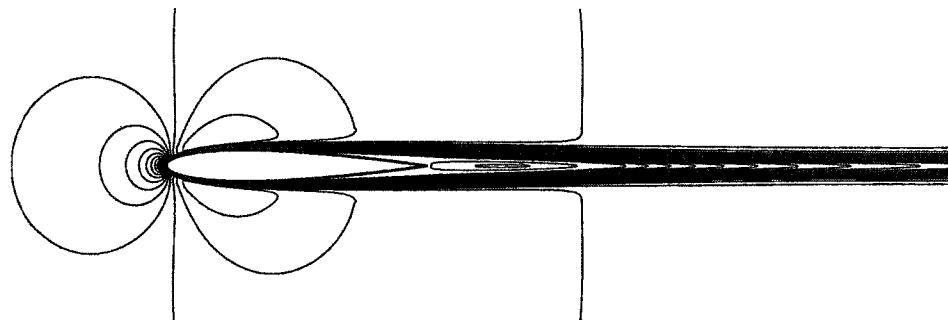


Figure 6.36: Mach contours for viscous flow over NACA0012 airfoil using second approach ($M_\infty = 0.5$, $Re = 1 \times 10^4$, $\alpha = 0^\circ$)

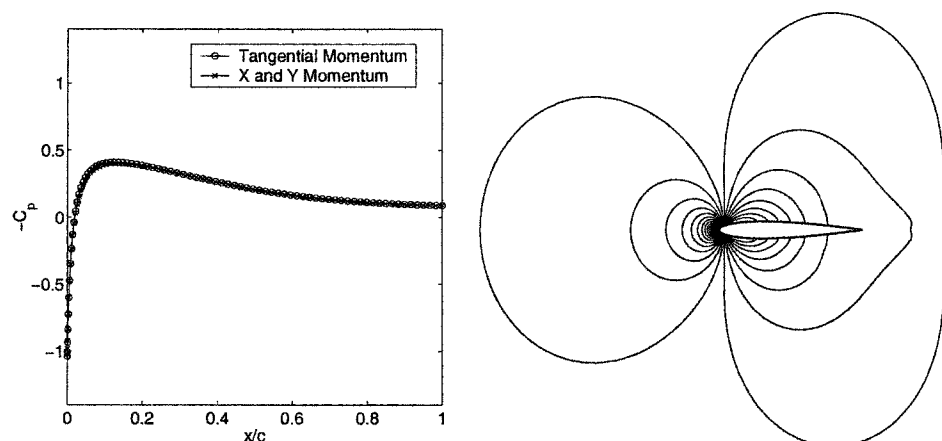


Figure 6.37: Surface pressure distribution for viscous flow over NACA0012 airfoil ($M_\infty = 0.5$, $Re = 1 \times 10^4$, $\alpha = 0^\circ$)

Figure 6.38: Pressure contours for viscous flow over NACA0012 airfoil using second approach ($M_\infty = 0.5$, $Re = 1 \times 10^4$, $\alpha = 0^\circ$)

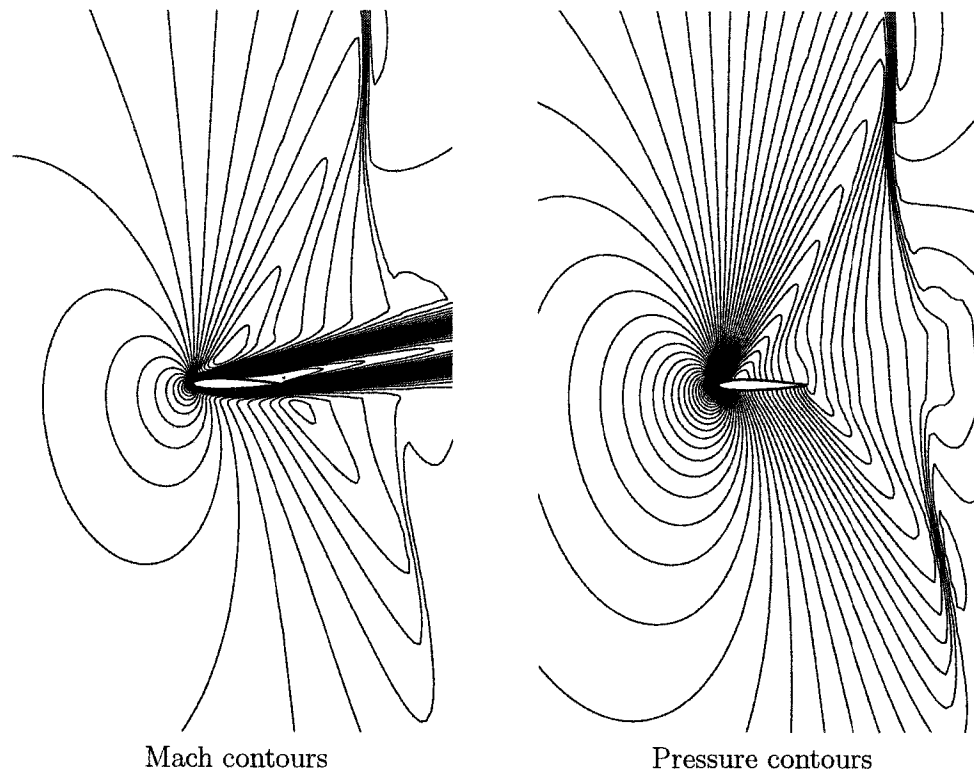


Figure 6.39: Viscous flow over NACA0012 airfoil using second approach
 $(M_\infty = 0.9, Re = 500, \alpha = 10^\circ)$

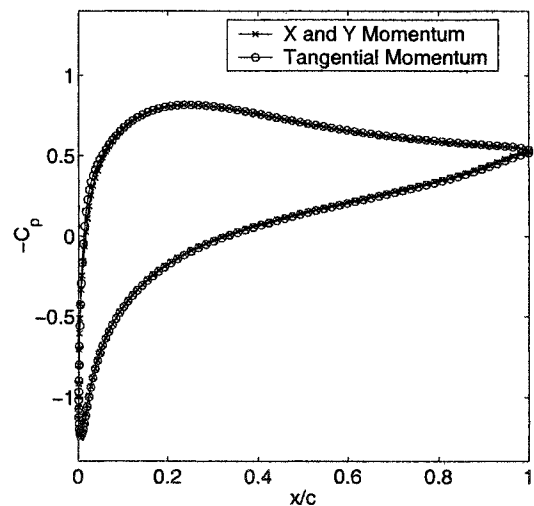


Figure 6.40: Surface pressure distributions for viscous flow over NACA0012 airfoil
 $(M_\infty = 0.9, Re = 500, \alpha = 10^\circ)$

CHAPTER 7

INVISCID AND VISCOUS FLOWS OVER WINGS

Three dimensional inviscid and viscous flows over a NACA0012 wing are simulated using the present formulation. The NACA0012 wing is derived from an ONERA M6 wing [109] replaced with NACA0012 airfoil cross-sections. Inviscid and viscous flows were simulated over the same NACA0012 wing by Tang and Hafez [104], [110] using the NASA Ames code, Overflow.

In the present work, a $(140 \times 40 \times 40)$ structured C-H grid is generated around the wing using algebraic methods, where a C-grid is wrapped around each wing cross-section and an H-grid is used in the spanwise direction which collapses into a single plane after the wing tip. The generated grid is shown in fig(7.1). Numerical simulations for both invsicid and viscous flows are performed.

A Zebra SLOR scheme is used for the augmented potential equation solver. Zebra schemes were used by Hafez [111], [112] and have the obvious advantage of being easily vectorizable, an important advantage in the case of three dimensional computations. In Zebra SLOR, all even planes can be solved at the same time using parallel processors, followed by the odd planes. Zebra schemes also provide another advantage by eliminating the $\phi_{\eta t}$ term resulting from the marching direction of the solver along

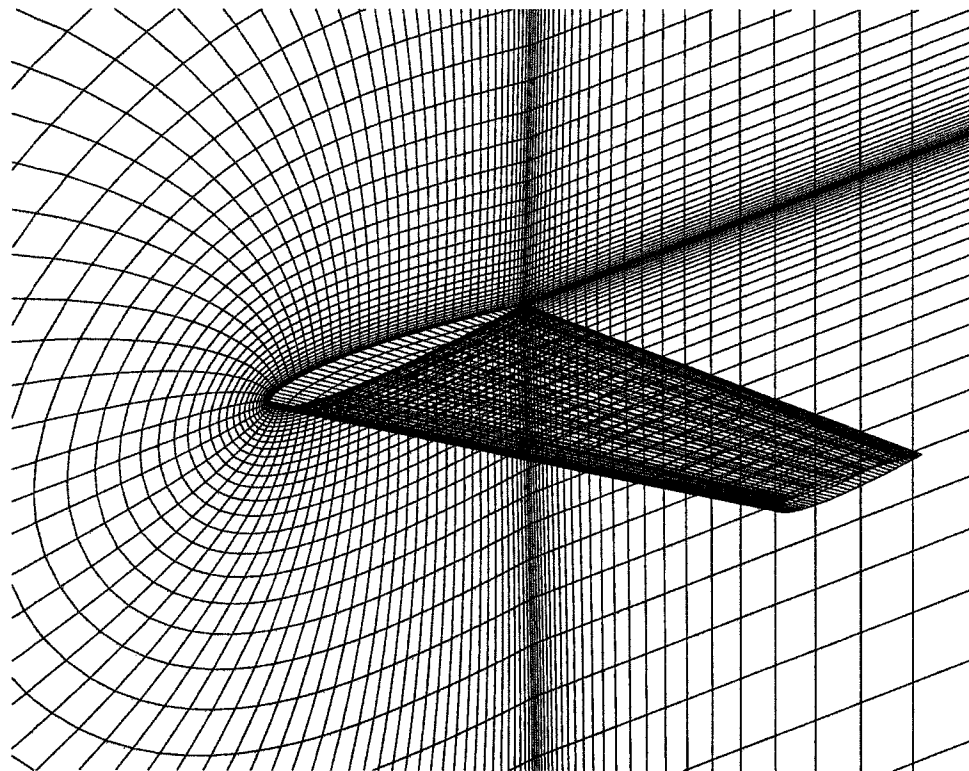


Figure 7.1: Structured C-H Grid for NACA0012 Wing

the wing span, where η represents the spanwise direction. This proves to be highly important for transonic flows, where the introduction of a $\phi_{\eta t}$ with the wrong sign, i.e. marching the planes against the flow direction, could lead to the divergence of the iterative solver.

7.1 Three Dimensional Farfield Boundary Condition

The boundary condition for the potential function in the farfield is evaluated from

$$\phi = U_\infty x + V_\infty y + W_\infty z + \frac{\Gamma(y)}{2\pi} \tan^{-1} \left[\sqrt{1 - M_\infty^2} \tan(\theta - \alpha) \right] \quad (7.1)$$

where $\Gamma(y)$ is the circulation which varies along the span. To test this boundary condition, numerical simulations are performed for inviscid flow over an elliptic wing of high aspect ratio ($AR = 9.0$) at subsonic conditions ($M_\infty = 0.3, \alpha = 2^\circ$). Results of the simulation are shown in fig(7.2) where the surface pressure distribution from 3-D calculations is in good agreement with that of corrected 2-D simulations based on the lifting line theory. The correction to the 2-D simulation is done by using an effective angle of attack (α_e), instead of the geometric angle of attack (α), in order to include the effect of downwash (α_i), where

$$\alpha_i = \frac{C_L}{\pi AR} \quad (7.2)$$

Hence,

$$\alpha_e = \alpha - \alpha_i = \frac{\alpha}{1 + \frac{m}{\pi AR}} \quad (7.3)$$

where it is assumed that the lift coefficient is linear in the angle of attack ($C_L = m\alpha$). The lift coefficient from the present 2D results agrees with the standard formula for thick airfoils

$$C_L = \frac{2\pi \left(1 + 0.77 \frac{t}{c}\right) \sin \alpha}{\sqrt{1 - M_\infty^2}} \quad (7.4)$$

while the corrected C_L results, according to the lifting line theory, agrees with the three-dimensional results as shown in fig(7.3). The pressure distributions on the upper and lower surfaces of the elliptic wing are given in figs(7.4) and (7.5) respectively.

7.2 Inviscid Flows Over NACA0012 Wing

Subsonic flow over the NACA0012 wing at $M_\infty = 0.3$ and $\alpha = 2^\circ$ is simulated first. The surface pressure distributions at six spanwise locations are shown in fig(7.6). The surface pressure contours on both the upper and lower wing surfaces are given in figs (7.7) and (7.8) respectively. For this subsonic case, both potential and rotational flow simulations are identical due to the absence of shock waves. The results of the present method are in good agreement with those of standard Euler calculations using Overflow [104] as evident from fig(7.6).

Next, a transonic flow case at $M_\infty = 0.84$ and $\alpha = 3^\circ$ is considered. Both potential and rotational flow simulations are performed. A comparison of the surface pressure distributions for the potential and rotational flows is given in fig(7.9). Surface pressure contours on the upper and lower wing surfaces for the potential flow simulation are given in figs(7.10) and (7.11), while those for the rotational flow simulation are given in figs(7.12) and (7.13).

7.3 Viscous Flows Over NACA0012 Wing

In this section, viscous flows over NACA0012 wing are considered. A transonic flow case at $M_\infty = 0.9$, $Re = 1000$ and $\alpha = 1.0$ is simulated using the present

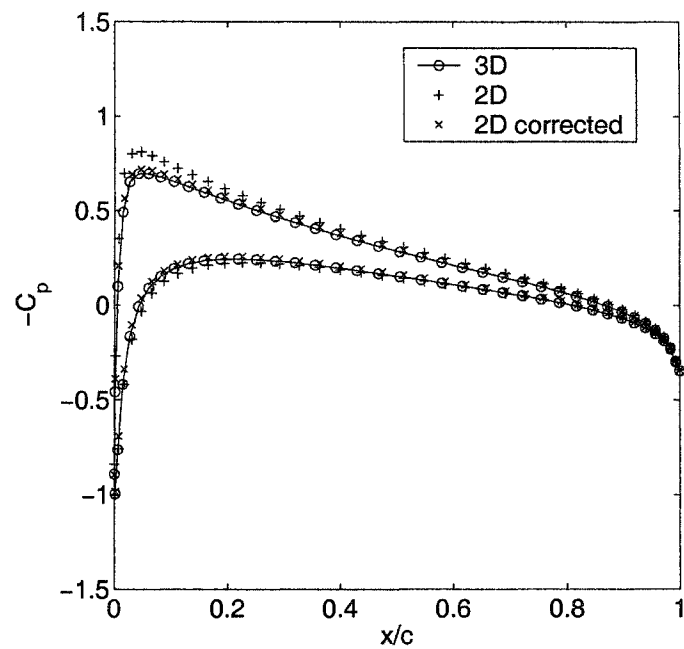


Figure 7.2: Surface pressure distribution for subsonic flow over an elliptic wing ($M_\infty = 0.3, \alpha = 2^\circ$)

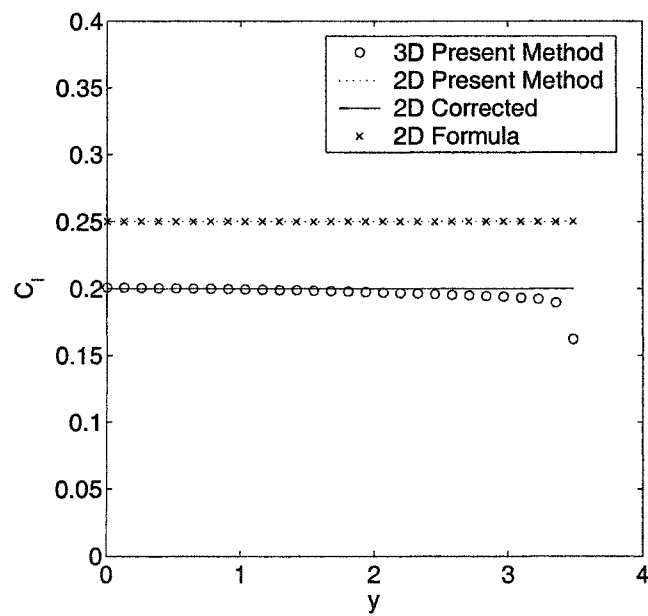


Figure 7.3: Local lift coefficient distribution for subsonic flow over an elliptic wing ($M_\infty = 0.3, \alpha = 2^\circ$)

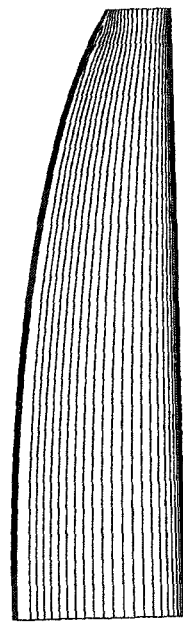


Figure 7.4: Pressure contours on upper surface of elliptic wing ($M_{\infty} = 0.3$, $\alpha = 2^\circ$)

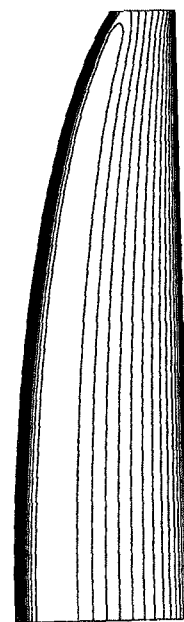


Figure 7.5: Pressure contours on lower surface of elliptic wing ($M_{\infty} = 0.3$, $\alpha = 2^\circ$)

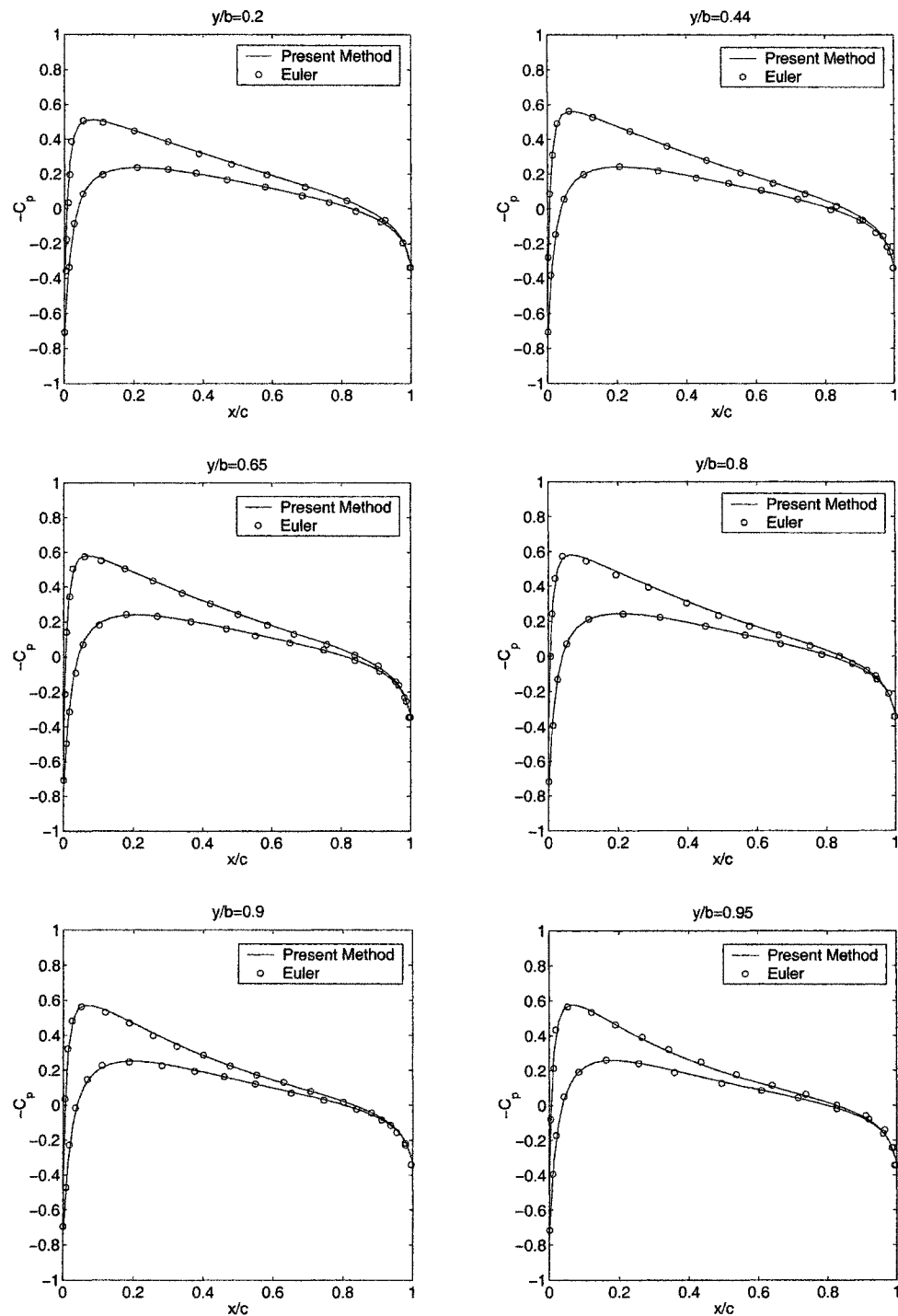


Figure 7.6: Surface pressure distributions for inviscid flow over NACA0012 wing ($M_\infty = 0.3$, $\alpha = 2^\circ$)

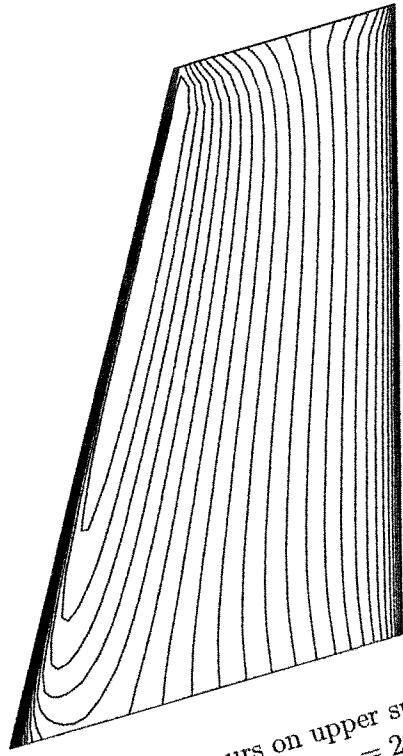


Figure 7.7: Pressure contours on upper surface of NACA0012 wing
($M_\infty = 0.3, \alpha = 2^\circ$)

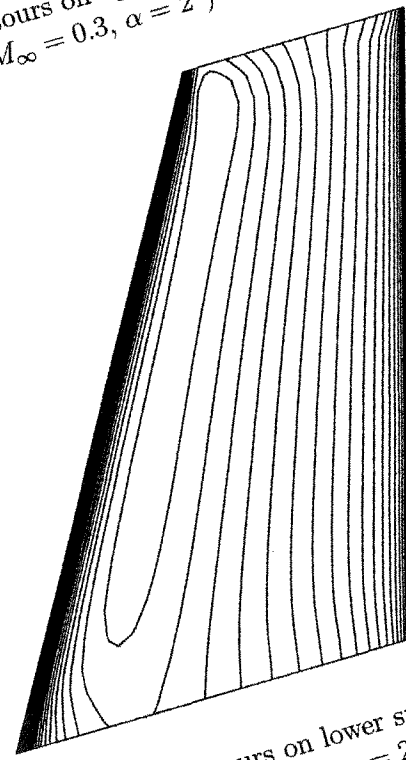


Figure 7.8: Pressure contours on lower surface of NACA0012 wing
($M_\infty = 0.3, \alpha = 2^\circ$)

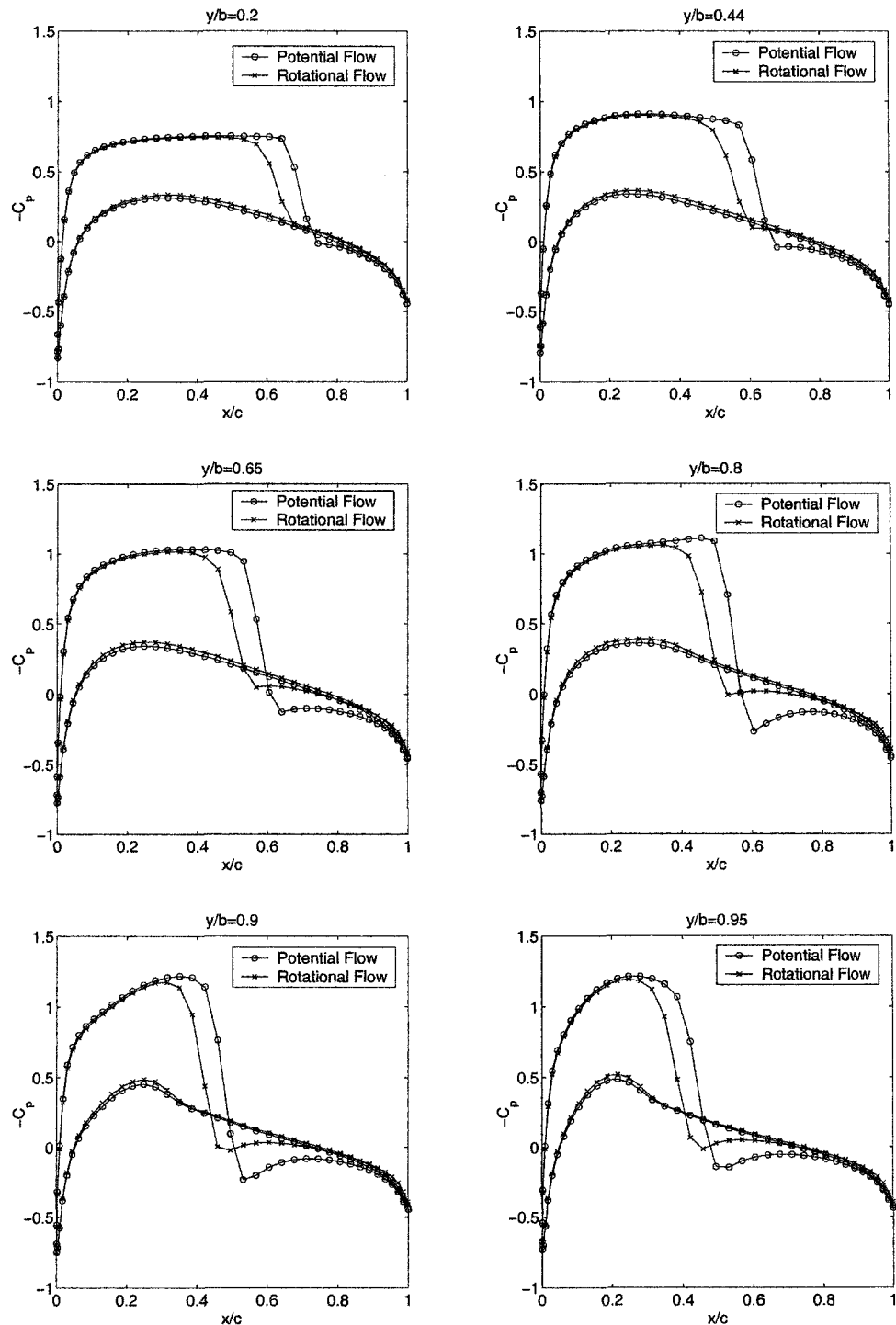


Figure 7.9: Surface pressure distributions for inviscid flow over NACA0012 wing
 $(M_\infty = 0.84, \alpha = 3^\circ)$



Figure 7.10: Pressure contours on upper surface of NACA0012 wing
($M_\infty = 0.84$, $\alpha = 3^\circ$, Potential Flow)

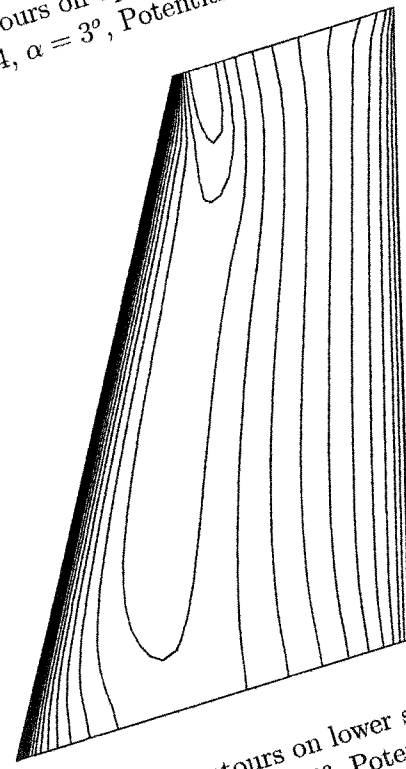


Figure 7.11: Pressure contours on lower surface of NACA0012 wing
($M_\infty = 0.84$, $\alpha = 3^\circ$, Potential Flow)

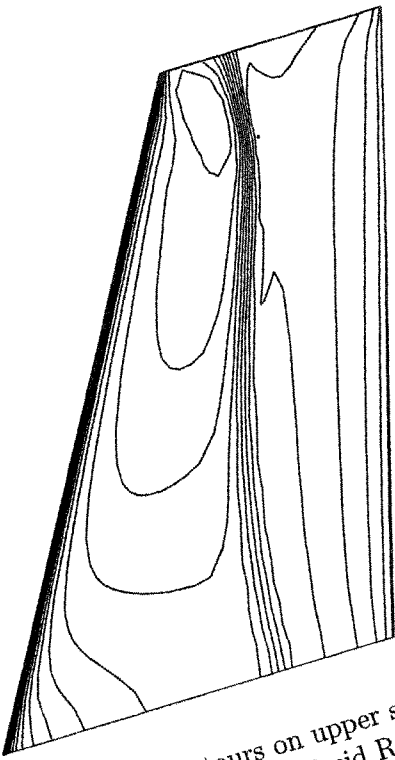


Figure 7.12: Pressure contours on upper surface of NACA0012 wing
($M_\infty = 0.84, \alpha = 3^\circ$, Inviscid Rotational Flow)

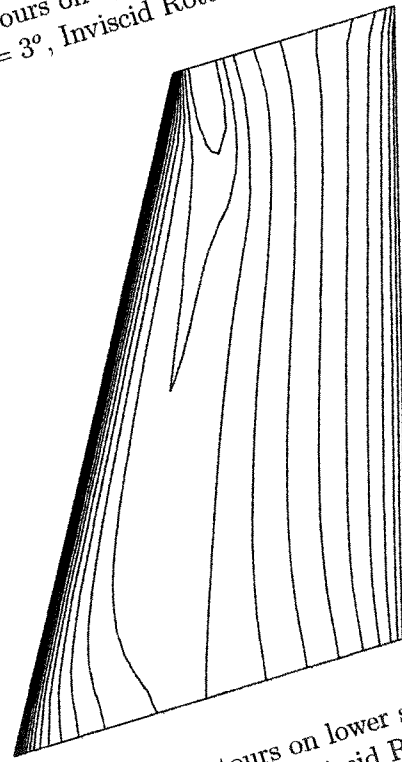


Figure 7.13: Pressure contours on lower surface of NACA0012 wing
($M_\infty = 0.84, \alpha = 3^\circ$, Inviscid Rotational Flow)

formulation. The two alternative approaches for evaluation of vorticity inside the viscous layer are applied and the results are compared to available standard Navier-Stokes calculations [110]. The results for the potential flow simulation at the same Mach number and angle of attack ($M_\infty = 0.9$ and $\alpha = 1.0$) are given in figs(7.14), (7.15), (7.16) and (7.23).

7.3.1 Evaluation of vorticity using first approach

In this approach, the normal component of the rotational velocity is chosen to be identically zero. The other two components are updated from their corresponding momentum equations as discussed in section (2.3.3). The surface pressure distributions are plotted in fig(7.17), while the surface pressure contours for the upper and lower wing surfaces are shown in figs(7.18) and (7.19) respectively. Good agreement between the present method and standard Navier-Stokes calculations [110] is achieved, as can be seen in fig(7.17).

7.3.2 Evaluation of vorticity using second approach

In the second approach, the x,y and z components of the rotational velocity are updated using the x,y and z momentum equations respectively. Fig(7.20) shows that both approaches of vorticity evaluation result in basically similar surface pressure distributions. The surface pressure contours on the upper and lower surfaces, using the second approach, are given in figs(7.21) and (7.22) respectively. Also, the Mach contours at the wing symmetry plane resulting from both approaches are nearly identical as evident in figs(7.24) and (7.25).

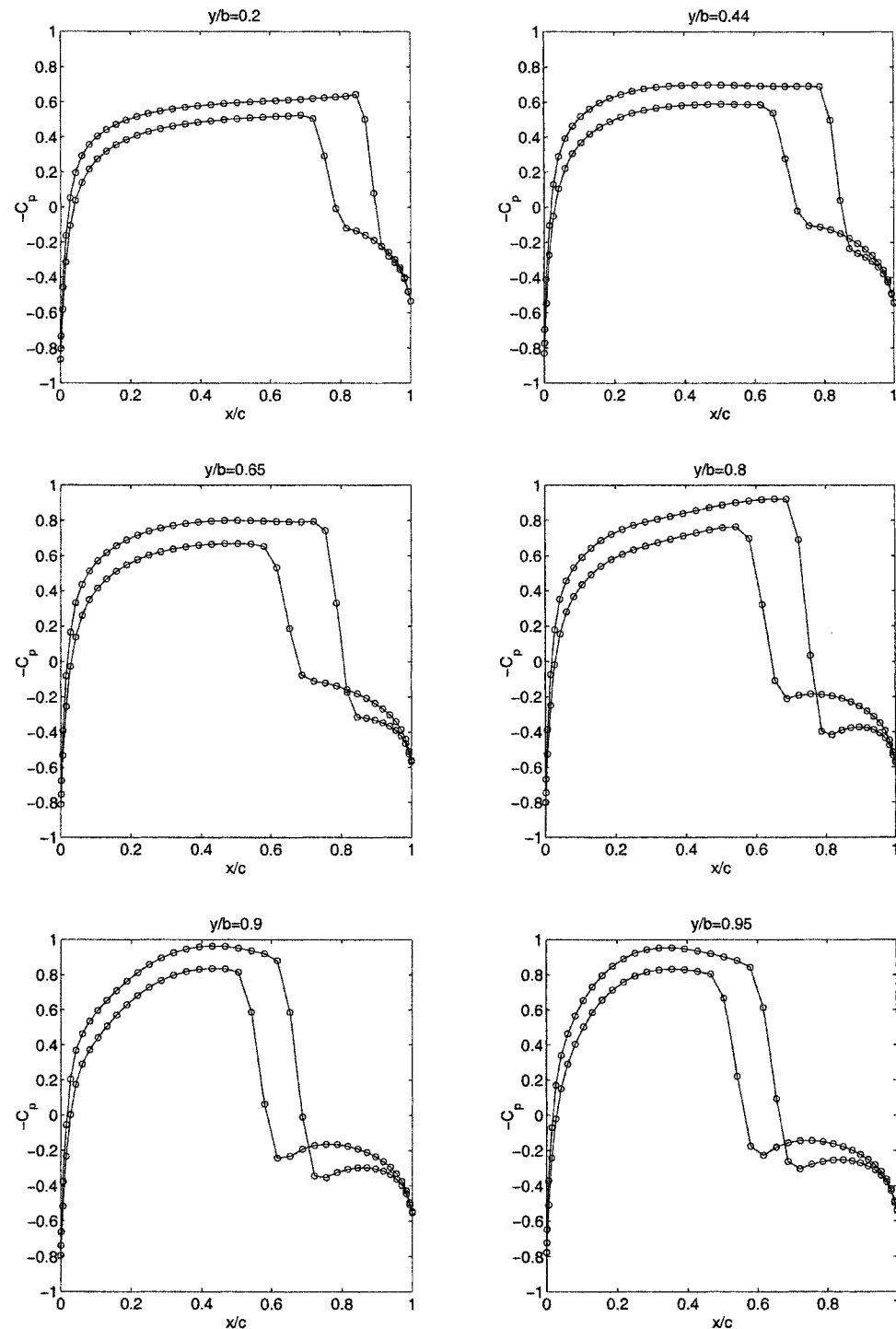


Figure 7.14: Surface pressure distributions for potential flow over NACA0012 Wing ($M_\infty = 0.9$, $\alpha = 1^\circ$)

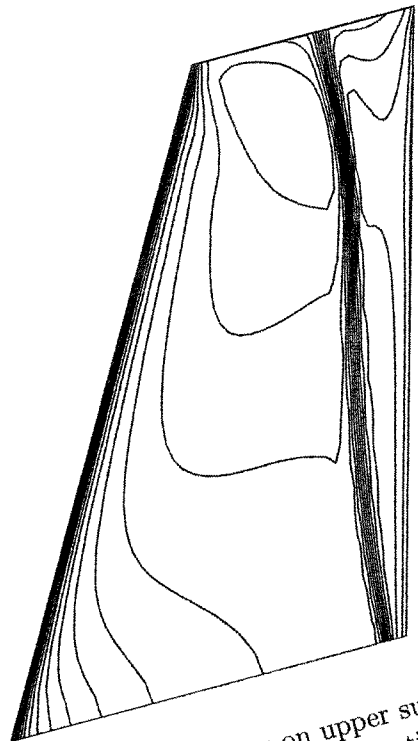


Figure 7.15: Pressure contours on upper surface of NACA0012 wing
($M_\infty = 0.9, \alpha = 1^\circ$, Potential Flow)

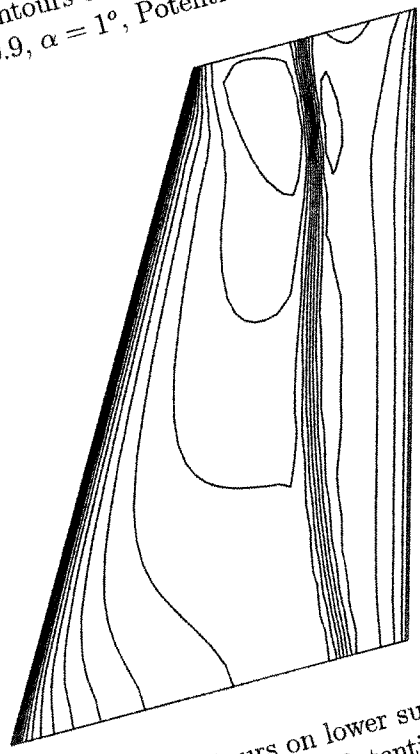


Figure 7.16: Pressure contours on lower surface of NACA0012 wing
($M_\infty = 0.9, \alpha = 1^\circ$, Potential Flow)

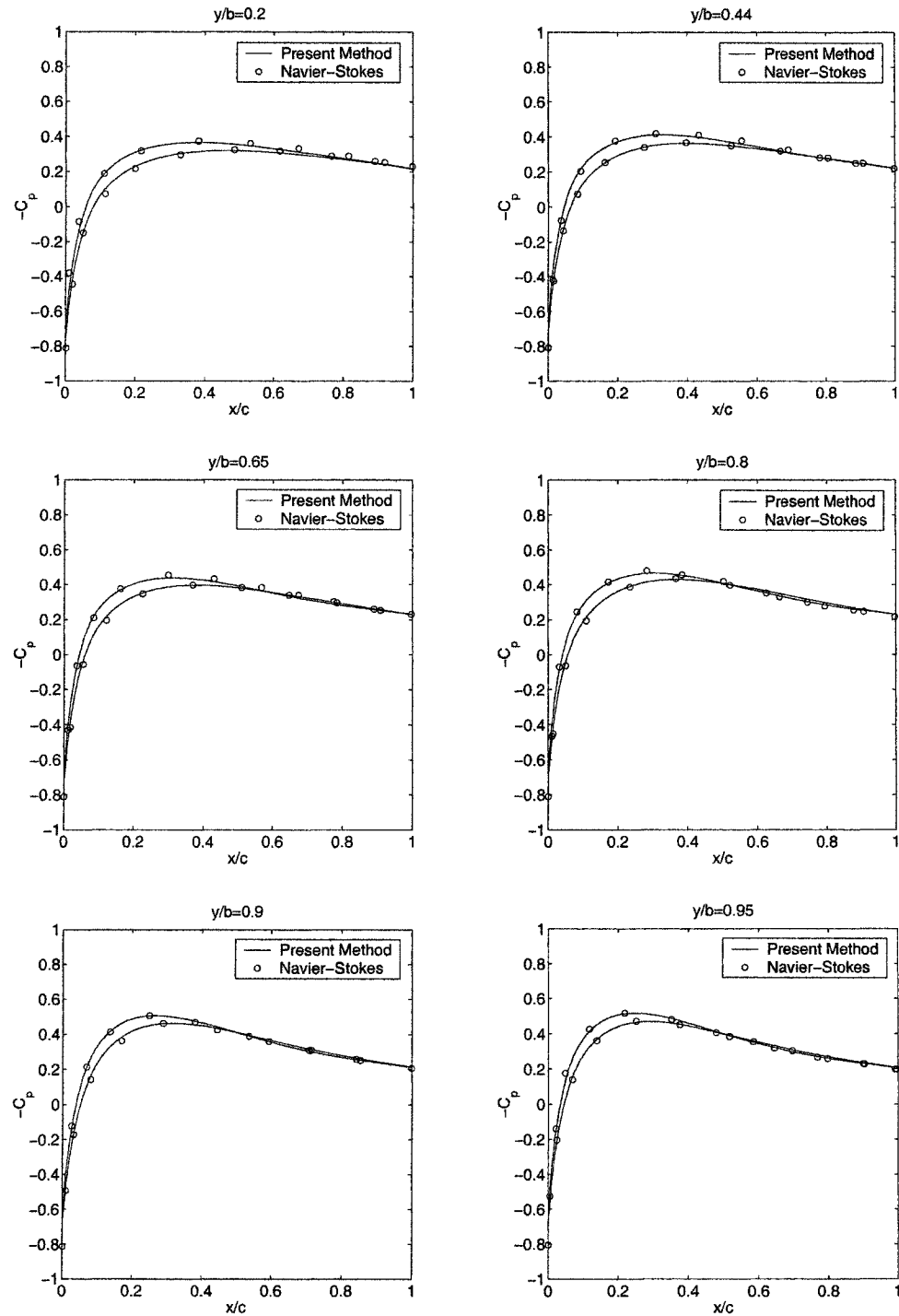


Figure 7.17: Surface pressure distributions for viscous flow over NACA 0012 wing using first approach ($M_\infty = 0.9$, $Re=1000$, $\alpha = 1^\circ$)

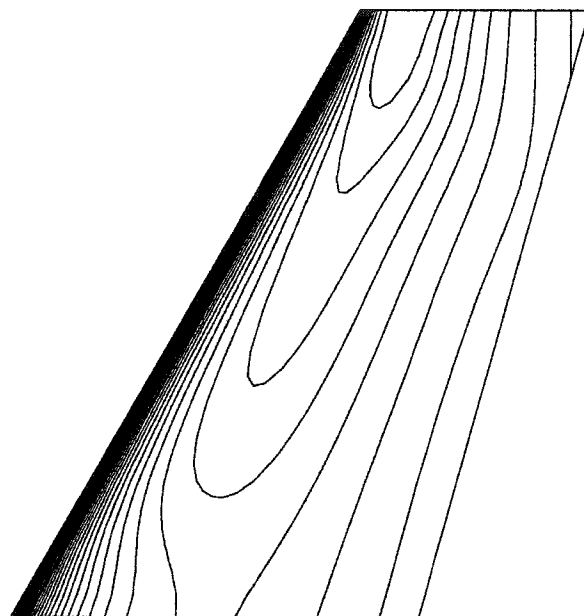


Figure 7.18: Pressure contours on upper surface of NACA0012 wing using first approach ($M_\infty = 0.9$, $Re=1000$, $\alpha = 1^\circ$)

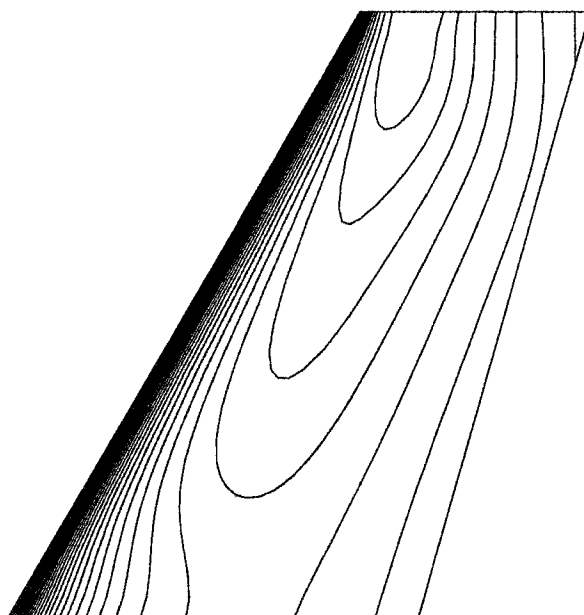


Figure 7.19: Pressure contours on lower surface of NACA0012 wing using first approach ($M_\infty = 0.9$, $Re=1000$, $\alpha = 1^\circ$)

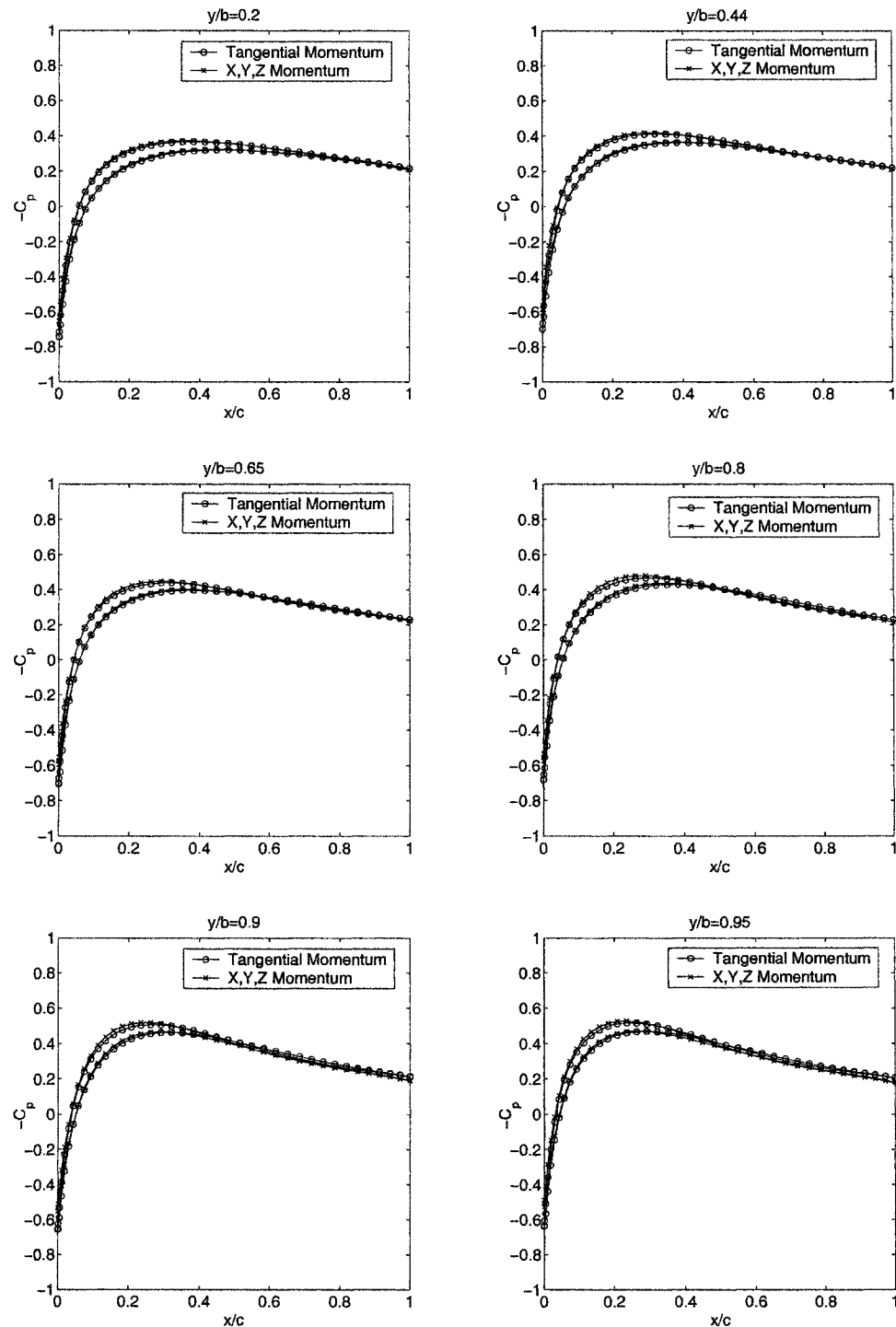


Figure 7.20: Comparison of surface pressure distributions for viscous flow over NACA0012 wing using the first and second approaches ($M_\infty = 0.9$, $Re=1000$, $\alpha = 1^\circ$)

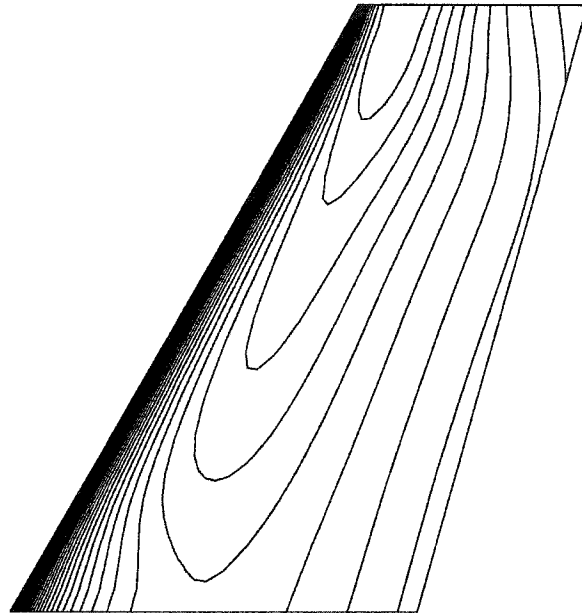


Figure 7.21: Pressure contours on upper surface of NACA0012 wing using second approach ($M_{\infty} = 0.9$, $Re=1000$, $\alpha = 1^{\circ}$)

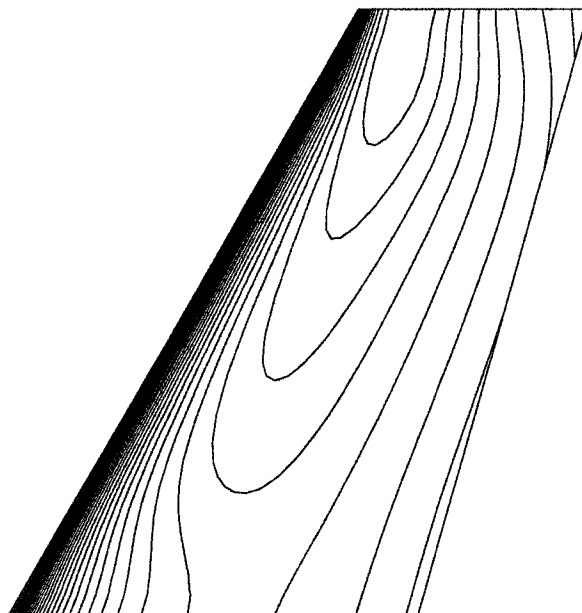


Figure 7.22: Pressure contours on lower surface of NACA0012 wing using second approach ($M_{\infty} = 0.9$, $Re=1000$, $\alpha = 1^{\circ}$)

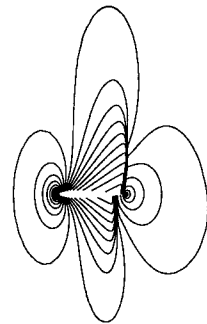


Figure 7.23: Mach contours at symmetry plane for potential flow over NACA0012 wing ($M_\infty = 0.9$, $\alpha = 1^\circ$)

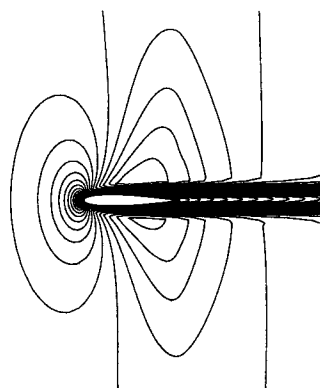


Figure 7.24: Mach contours at symmetry plane for viscous flow over NACA0012 wing using first approach ($M_\infty = 0.9$, $Re=1000$, $\alpha = 1^\circ$)

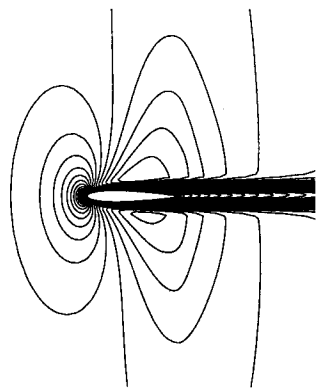


Figure 7.25: Mach contours at symmetry plane for viscous flow over NACA0012 wing using second approach ($M_\infty = 0.9$, $Re=1000$, $\alpha = 1^\circ$)

CHAPTER 8

MULTIGRID METHODS

Slow convergence rates are usually encountered by iterative methods when fine grids are used. The reason behind the slow rates of convergence is that iterative methods are efficient in removing the high frequency components of the error, while they are inefficient in removing the low frequency components. Multigrid methods remedy this problem by the efficient use of a sequence of coarser grids. Multigrid methods are considered among the most efficient tools for accelerating the convergence of iterative solvers.

Multigrid methods were first applied to elliptic equations by Fedorenko [113], [114]. Later, Brandt [115] extended multigrid methods to the equations of fluid mechanics. Recently, textbook multigrid efficiency has been obtained for flow simulations by Thomas, Diskin and Brandt [116]. Impressive convergence rates for two dimensional transonic inviscid flows are also reported by Caughey and Jameson [117]. However, there is still need for more improvement regarding the application of multigrid to viscous flow problems, specially for high Reynolds number flows where the existence of boundary layers and wakes affects the efficiency of multigrid methods.

To illustrate the multigrid process, it is useful to consider first the process with

two grids only. The multigrid scheme, described in the following section, is known as the Correction Storage (CS) scheme.

8.1 The Correction Storage (CS) Scheme

Consider the linear problem

$$A_f(\phi_f) = b_f \quad (8.1)$$

where the subscript (f) stands for the fine grid. The residual on the fine grid is defined as follows

$$R_f(\phi_f) = A_f(\phi_f) - b_f \quad (8.2)$$

Using an iterative scheme (smoother), a few iterations are performed on the fine grid to smooth out the error by removing the high frequency component relevant to this grid. Notice that over-relaxation should not be used in the smoother as it destroys the smoothing property of relaxation methods. Hence, the over-relaxation parameter should always be limited to ($\omega \leq 1$) for the smoother. The residual is then evaluated on the fine grid and restricted to the coarse grid using a restriction operator \Downarrow_c^f . The following problem is solved on the coarse grid

$$A_c(\delta\phi_c) = -\Downarrow_c^f R_f(\phi_f) \quad (8.3)$$

where the subscript (c) stands for the coarse grid. Solving eqn (8.3) to convergence

on the coarse grid efficiently removes the low frequency component of the error. The correction on the coarse grid ($\delta\phi_c$) is prolongated to the fine grid using the prolongation operator \uparrow_c^f . The values of the unknowns on the fine grid are updated using the coarse grid correction as follows

$$\phi_f^{new} = \phi_f^{old} + \uparrow_c^f \delta\phi_c \quad (8.4)$$

A few iterations are performed on the fine grid using the smoother to remove the high frequency error introduced by the prolongation operator. The previous procedure represents one cycle of the two grid process. If convergence is not yet achieved on the fine grid, more cycles are performed.

The two grid process discussed above can be extended to more grids by induction. There are different structures available for multigrid cycles, the most important of which are the V-cycle and the W-cycle shown in fig(8.1).

However, for nonlinear problems, the (CS) scheme is not suitable and a nonlinear multigrid procedure known as the Full Approximation Storage (FAS) scheme is used.

8.2 The Full Approximation Storage (FAS) Scheme

In the nonlinear (FAS) scheme, introduced by Brandt [118], the problem to be solved on the coarse grid is modified to read as follows

$$R_c(\phi_c) = R_c(\downarrow_c^f \phi_f) - \downarrow_c^f R_f(\phi_f) \quad (8.5)$$

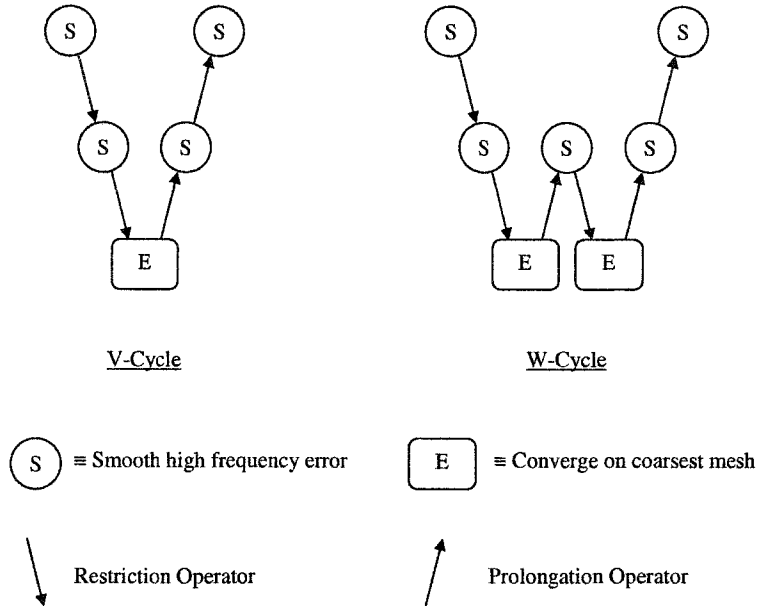


Figure 8.1: Structure of Multigrid Cycles

The right hand side of equation (8.5) is the difference between the residual on the coarse mesh, evaluated based on the restriction of the fine mesh values ϕ_f , and the restriction of the fine mesh residual to the coarse mesh. In solving equation (8.5) on the coarse mesh, the right hand side should be frozen. A correction on the coarse mesh from the solution of equation (8.5) can be calculated from

$$\delta\phi_c = \phi_c - \Downarrow_c^f \phi_f \quad (8.6)$$

Eqn (8.4) is used to obtain the new values on the fine mesh from the coarse grid correction. The efficiency of the FAS scheme can be further improved by applying it in conjunction with a full multigrid (FMG) procedure.

8.3 The Full Multigrid (FMG) Procedure

In the full multigrid procedure, the process starts by obtaining a converged solution on the coarsest grid. The solution is then prolongated to a finer grid and used as an initial guess for a multigrid cycle. After performing the multigrid cycle, the obtained solution is prolongated to a third finer grid. This process is repeated until the finest grid is reached. The finest grid now has an improved initial guess and multigrid cycles are performed starting with the improved initial guess until convergence is achieved. An example of a three grid V-cycle FMG procedure is shown in figure (8.2). In the following section, the details of the multigrid procedure applied to the augmented potential equation are given.

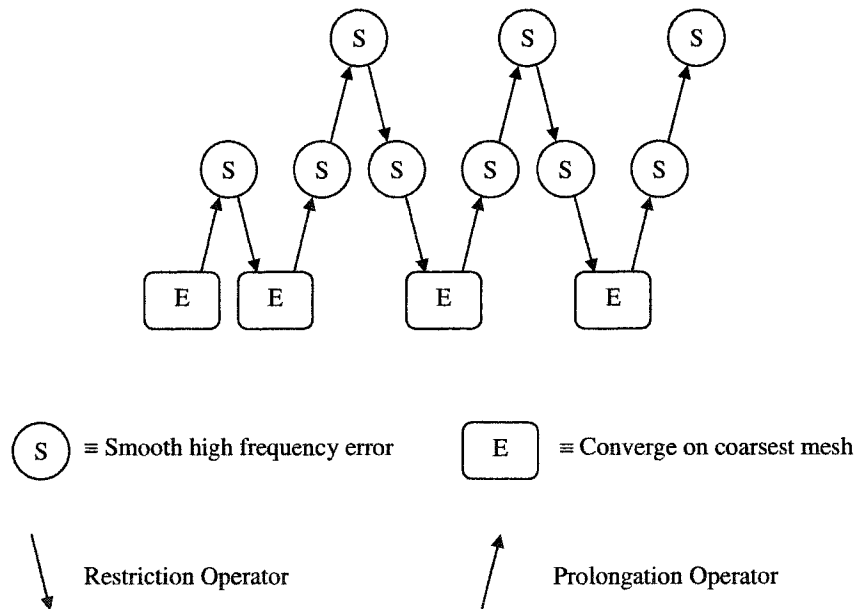


Figure 8.2: Full Multigrid Procedure

8.4 Multigrid procedure for the Augmented Potential Equation

In the present work, a nonlinear FMG-FAS multigrid scheme with a V-cycle structure is applied to the augmented potential equation

$$\nabla \cdot (\rho \nabla \phi) = -\nabla \cdot (\rho \vec{q}^*) \quad (8.7)$$

Three grids are used; coarse, intermediate and fine. The coarser grids are generated from the fine grid using a full coarsening approach, where every second point is removed along both coordinate directions. Other coarsening approaches are possible, such as the semi-coarsening procedure [119], where coarsening is performed along one coordinate direction only. However, semi-coarsening is computationally expensive and problematic in complex geometries [117].

Line relaxation is used as the smoother. Bilinear interpolation is used for the prolongation operator while full weighting is used for the restriction operator. In full weighting, the residual at a coarse mesh point is obtained from contributions of the residuals of all neighboring fine mesh points

$$R_{c_{i,j}} = \frac{4R_{f_{2i-1,2j-1}} + 2R_{f_{2i,2j-1}} + 2R_{f_{2i-2,2j-1}} + 2R_{f_{2i-1,2j}}}{16} \\ + \frac{2R_{f_{2i-1,2j-2}} + R_{f_{2i,2j}} + R_{f_{2i-2,2j-2}} + R_{f_{2i,2j-2}} + R_{f_{2i-2,2j}}}{16} \quad (8.8)$$

The weighting used in eqn(8.8) is suitable for uniform and reasonably stretched grids. In case of highly stretched grids, a weighting based on the areas of the elements is used.

The convection/diffusion equations for entropy, vorticity and total enthalpy are evaluated on the fine grid only. In the following, numerical simulations for inviscid and viscous flows over NACA0012 airfoil are performed using single and multiple grids to evaluate the efficiency of the proposed multigrid procedure.

8.5 Inviscid Flows over an airfoil

Figures (8.3) and (8.4) show the Mach contours for potential and inviscid rotational flows at $M_\infty = 0.86$ and $\alpha = 0^\circ$. The corresponding convergence histories for the augmented potential equation are plotted in figures (8.5) and (8.6). Notice that the convergence rates of the potential and rotational flows are very similar for single and multiple grids.

Similar results for $M_\infty = 1.5$ and $\alpha = 0^\circ$ are plotted in figures (8.7),(8.8),(8.9) and (8.10). The corresponding results for viscous supersonic flow calculations ($Re = 1 \times 10^4$), with and without including the entropy and the vorticity generated by curved shocks, are shown in figures (8.11),(8.12),(8.13) and (8.14).

8.6 Viscous Flows over an airfoil

In figures (8.15) and (8.16), the Mach contours are plotted for potential and viscous flows ($Re = 500$) at $M_\infty = 0.1$ and $\alpha = 0^\circ$. The corresponding residual histories are plotted in figures (8.17) and (8.18). Similar results for the case of $\alpha = 10^\circ$ are shown in figures (8.19),(8.20),(8.21) and (8.22). In these calculations, the compressibility effects are negligible.

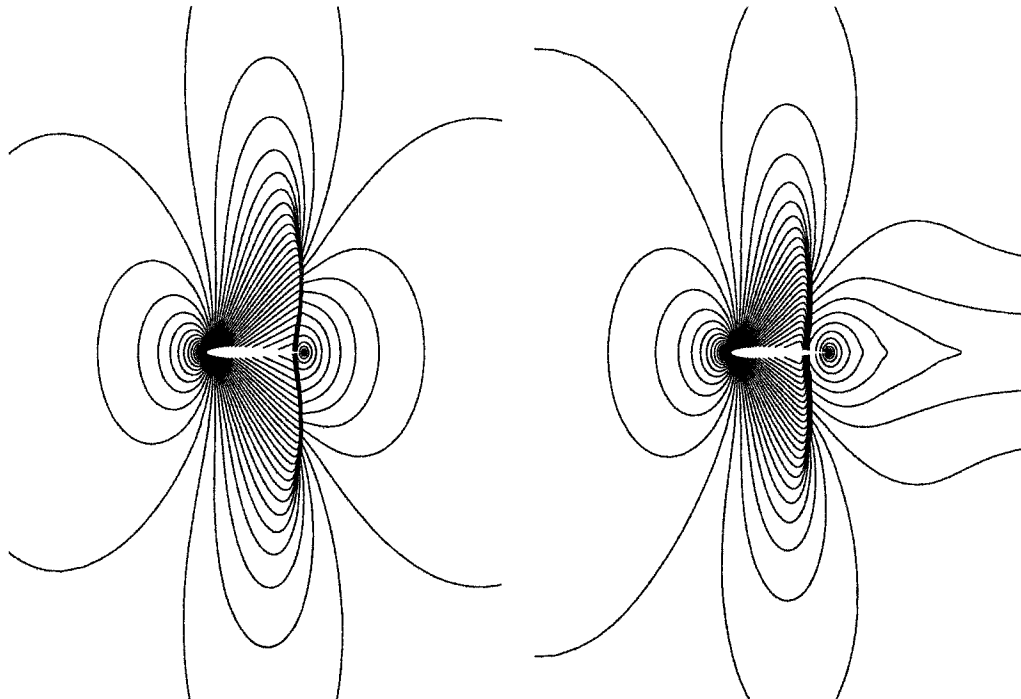


Figure 8.3: Mach contours for potential flow over NACA0012 airfoil ($M_\infty = 0.86$, $\alpha = 0^\circ$)

Figure 8.4: Mach contours for inviscid rotational flow over NACA0012 airfoil ($M_\infty = 0.86$, $\alpha = 0^\circ$)

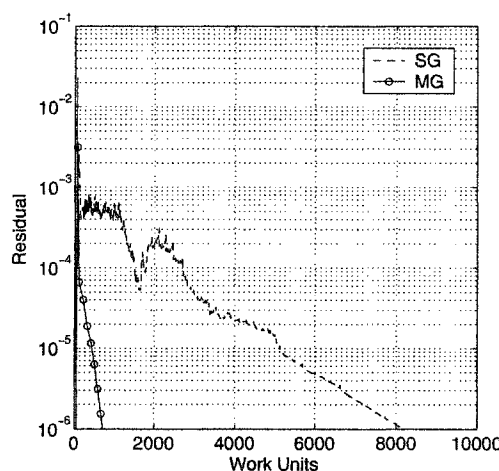


Figure 8.5: Convergence history for potential flow over NACA0012 airfoil ($M_\infty = 0.86$, $\alpha = 0^\circ$)

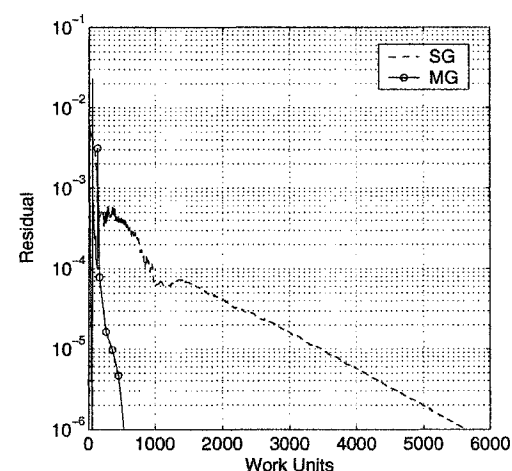


Figure 8.6: Convergence history for inviscid rotational flow over NACA0012 airfoil ($M_\infty = 0.86$, $\alpha = 0^\circ$)

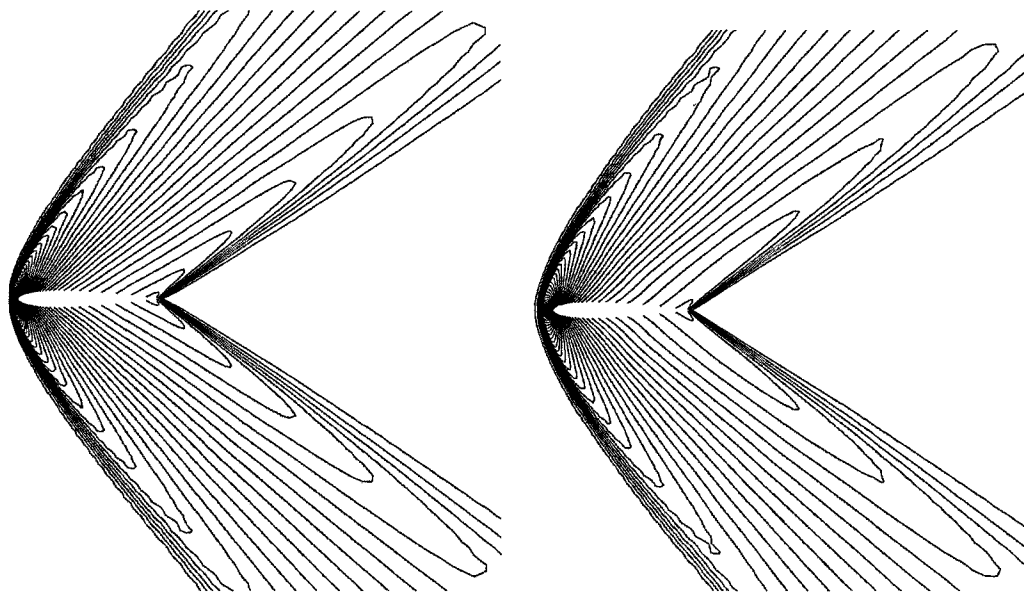


Figure 8.7: Mach contours for potential flow over NACA0012 airfoil ($M_\infty = 1.5$, $\alpha = 0^\circ$)

Figure 8.8: Mach contours for inviscid rotational flow over NACA0012 airfoil ($M_\infty = 1.5$, $\alpha = 0^\circ$)

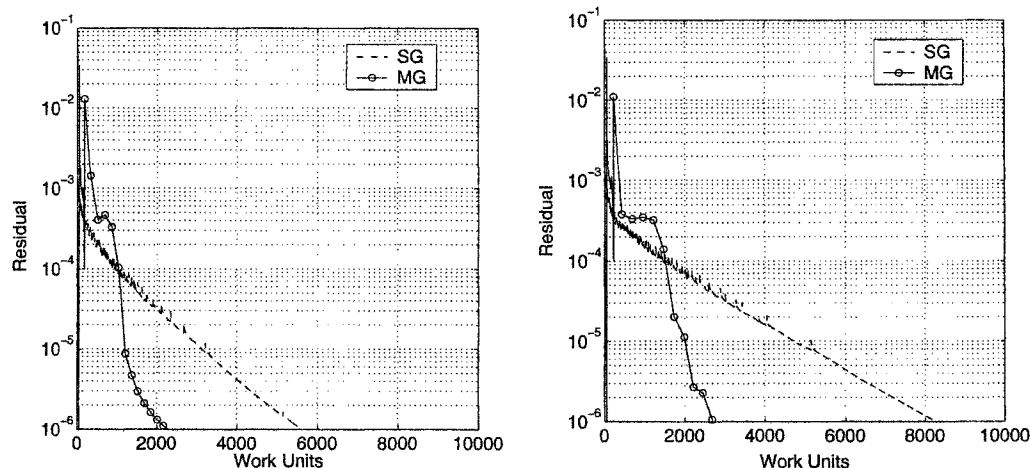


Figure 8.9: Convergence history for potential flow over NACA0012 airfoil ($M_\infty = 1.5$, $\alpha = 0^\circ$)

Figure 8.10: Convergence history for inviscid rotational flow over NACA0012 airfoil ($M_\infty = 1.5$, $\alpha = 0^\circ$)

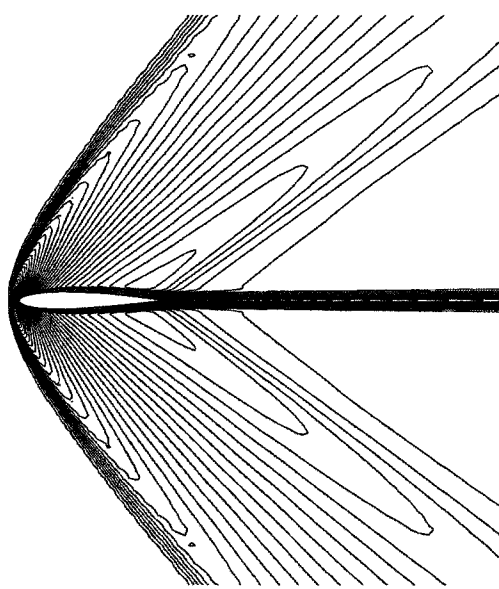


Figure 8.11: Mach contours for viscous flow over NACA0012 airfoil ($M_\infty = 1.5$, $Re = 1 \times 10^4$, $\alpha = 0^\circ$): Coupling potential flow with viscous layer

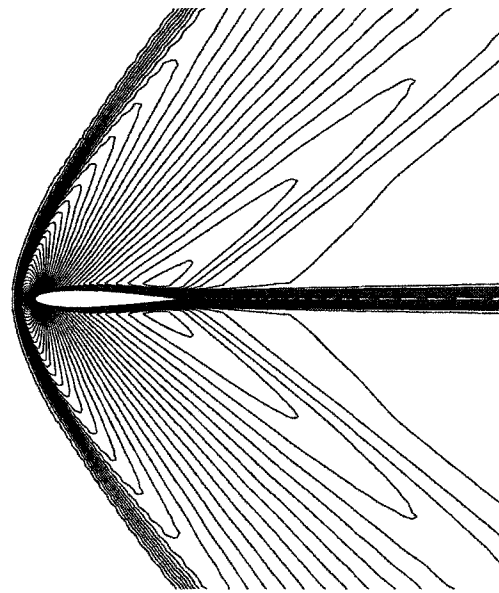


Figure 8.12: Mach contours for viscous flow over NACA0012 airfoil ($M_\infty = 1.5$, $Re = 1 \times 10^4$, $\alpha = 0^\circ$): Coupling rotational flow with viscous layer

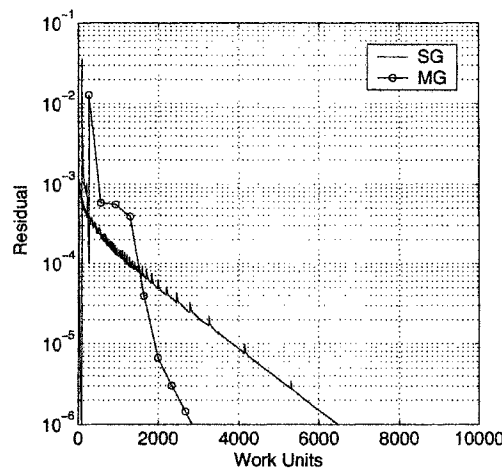


Figure 8.13: Convergence history for viscous flow over NACA0012 airfoil ($M_\infty = 1.5$, $Re = 1 \times 10^4$, $\alpha = 0^\circ$): Coupling potential flow with viscous layer

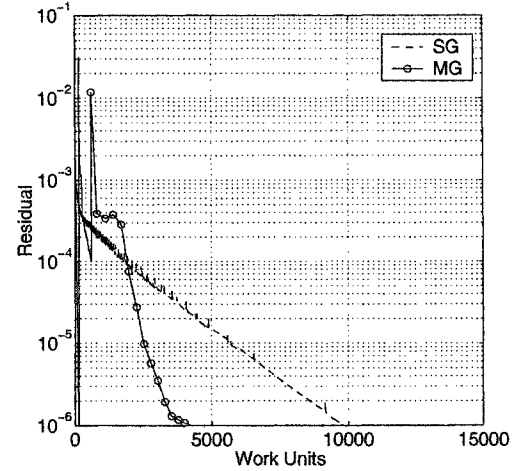


Figure 8.14: Convergence history for viscous flow over NACA0012 airfoil ($M_\infty = 1.5$, $Re = 1 \times 10^4$, $\alpha = 0^\circ$): Coupling rotational flow with viscous layer

The effect of compressibility on the performance of multigrid is examined next for $M_\infty = 0.8$ and $M_\infty = 0.9$ at $\alpha = 0^\circ$ and $\alpha = 10^\circ$ for potential and viscous flows ($Re = 500$). The results are plotted in figures (8.23)-(8.38) and show that there is no degeneration in multigrid performance, even in the presence of strong shocks.

The results for $M_\infty = 0.85$ at $\alpha = 0^\circ$ for potential and viscous flows ($Re = 2000$) are plotted in figures (8.39)-(8.42). The work unit for viscous flow simulations includes the residual evaluations of the augmented potential equation and the momentum equations on the fine mesh. The latter are updated only in the viscous layer.

Higher Reynolds number flows ($Re = 1 \times 10^4$) are calculated for $M_\infty = 0.5$ at $\alpha = 0^\circ$, see figures (8.43)-(8.46). For these cases, a highly stretched grid is used without noticeable degeneration of multigrid performance. The results of the potential flow calculations are comparable to the work of Jameson where he introduced the MAD scheme, see [120]. On the other hand, for viscous flow problems, the efficiency of the present results is comparable to that of ref. [121]. The proposed multigrid procedure results in an order of magnitude reduction in the work unit as compared to the single grid procedure for subsonic and transonic flows. However, for supersonic free streams, the gain from multigrid, when compared with the single grid procedure, is not as impressive as that for subsonic and transonic cases due to the hyperbolic nature of supersonic flows.

Finally, the extension to three-dimensional flows is straightforward, at least in each cross-section, the calculations can be treated in a quasi two-dimensional manner.

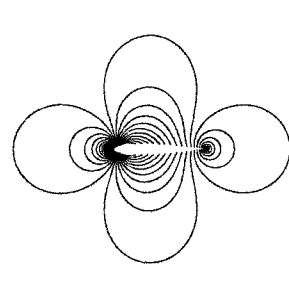


Figure 8.15: Mach contours for potential flow over NACA0012 airfoil ($M_\infty = 0.1, \alpha = 0^\circ$)

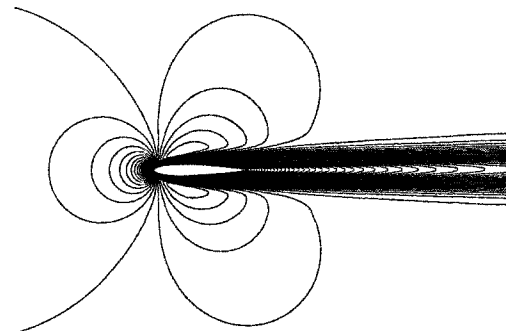


Figure 8.16: Mach contours for viscous flow over NACA0012 airfoil ($M_\infty = 0.1, Re = 500, \alpha = 0^\circ$)

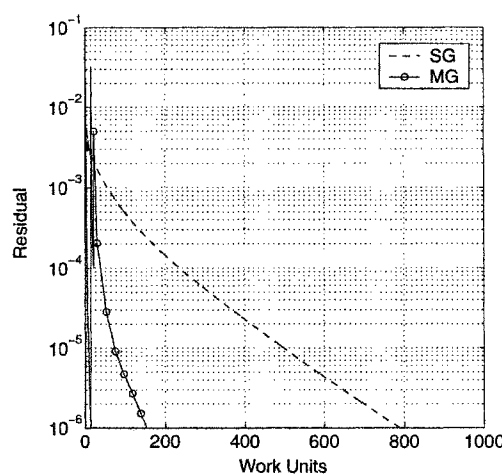


Figure 8.17: Convergence history for potential flow over NACA0012 airfoil ($M_\infty = 0.1, \alpha = 0^\circ$)

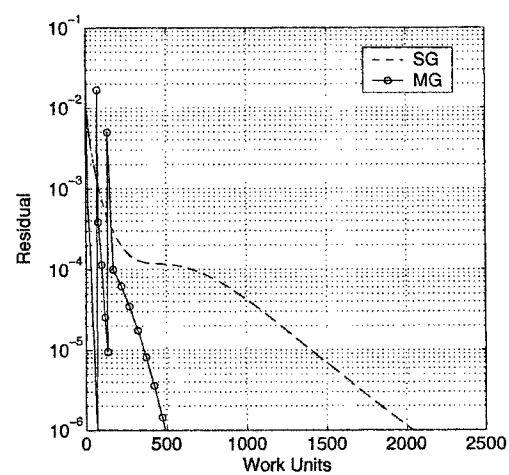


Figure 8.18: Convergence history for viscous flow over NACA0012 airfoil ($M_\infty = 0.1, Re = 500, \alpha = 0^\circ$)

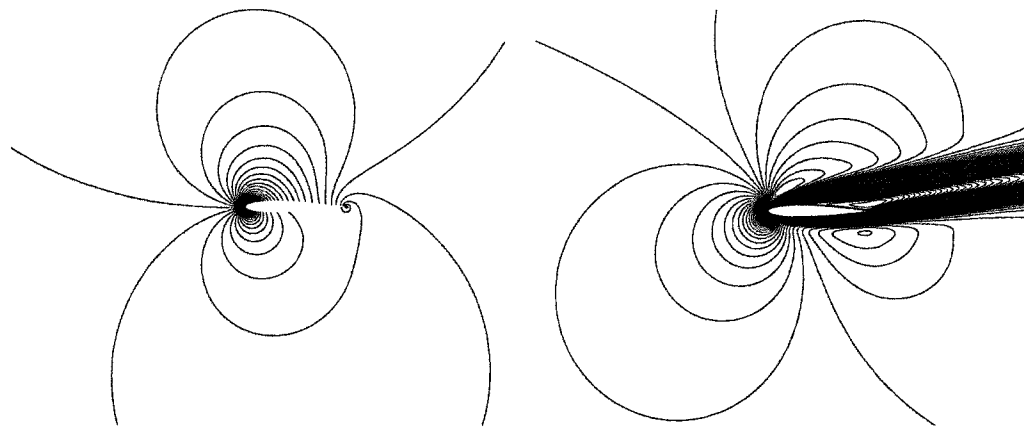


Figure 8.19: Mach contours for potential flow over NACA0012 airfoil
 $(M_\infty = 0.1, \alpha = 10^\circ)$

Figure 8.20: Mach contours for viscous flow over NACA0012 airfoil ($M_\infty = 0.1, Re = 500, \alpha = 10^\circ$)

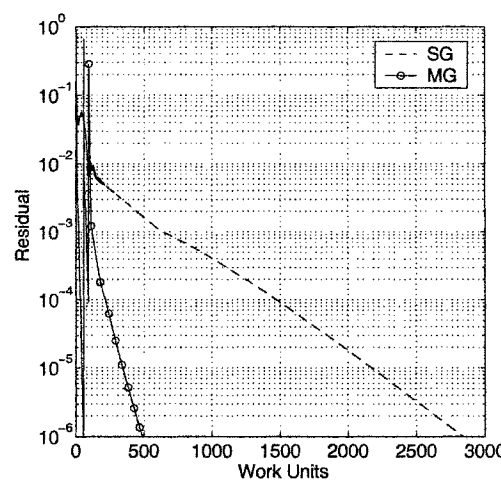


Figure 8.21: Convergence history for potential flow over NACA0012 airfoil
 $(M_\infty = 0.1, \alpha = 10^\circ)$

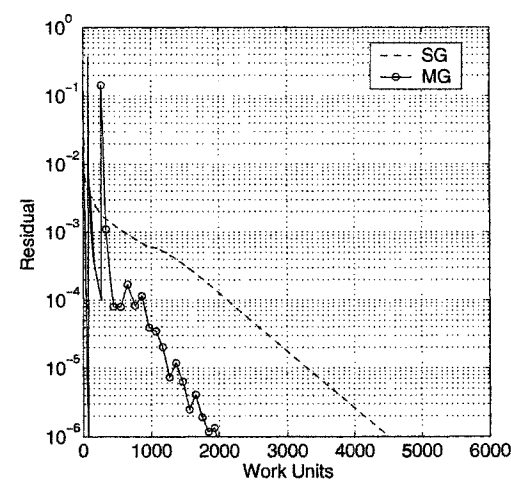


Figure 8.22: Convergence history for viscous flow over NACA0012 airfoil
 $(M_\infty = 0.1, Re = 500, \alpha = 10^\circ)$

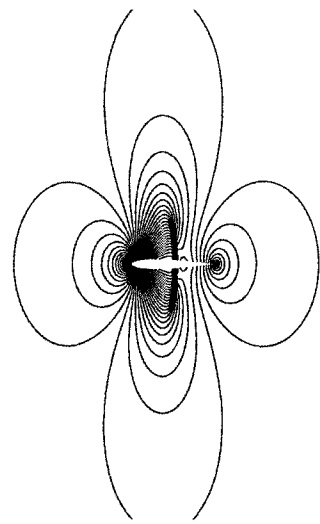


Figure 8.23: Mach contours for potential flow over NACA0012 airfoil ($M_\infty = 0.8$, $\alpha = 0^\circ$)

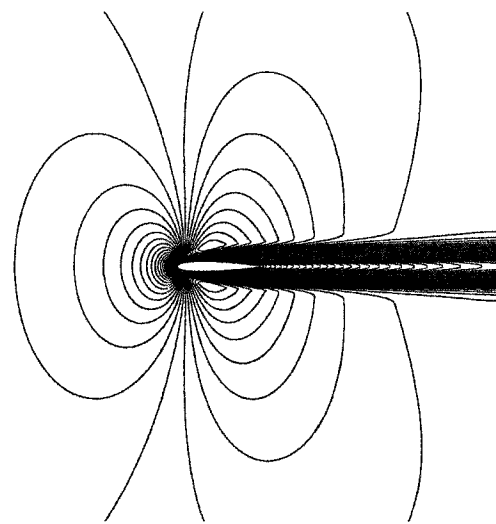


Figure 8.24: Mach contours for viscous flow over NACA0012 airfoil ($M_\infty = 0.8$, $Re = 500$, $\alpha = 0^\circ$)

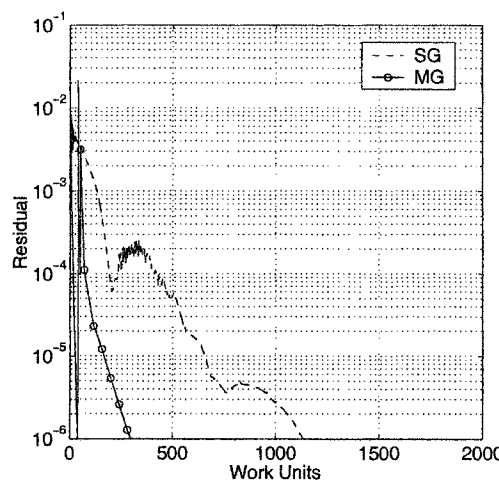


Figure 8.25: Convergence history for potential flow over NACA0012 airfoil ($M_\infty = 0.8$, $\alpha = 0^\circ$)

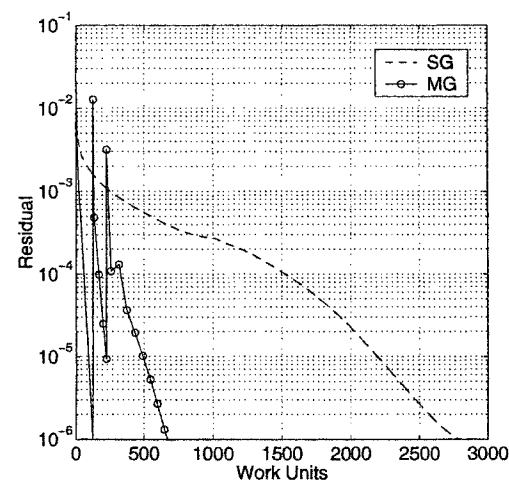


Figure 8.26: Convergence history for viscous flow over NACA0012 airfoil ($M_\infty = 0.8$, $Re = 500$, $\alpha = 0^\circ$)

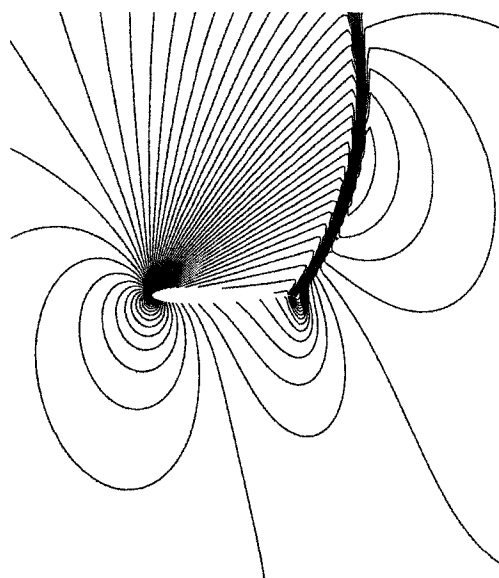


Figure 8.27: Mach contours for potential flow over NACA0012 airfoil ($M_\infty = 0.8, \alpha = 10^\circ$)

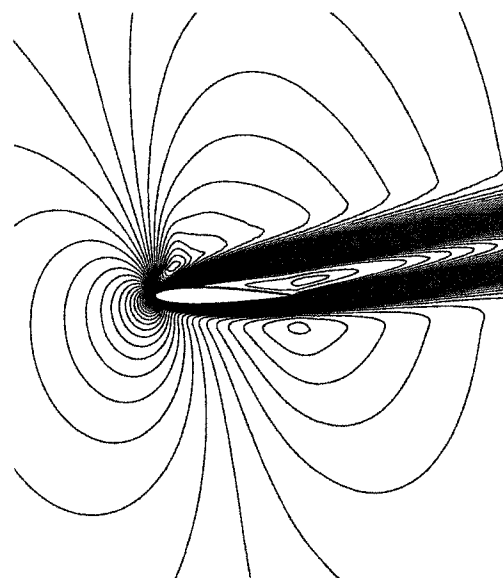


Figure 8.28: Mach contours for viscous flow over NACA0012 airfoil ($M_\infty = 0.8, Re = 500, \alpha = 10^\circ$)

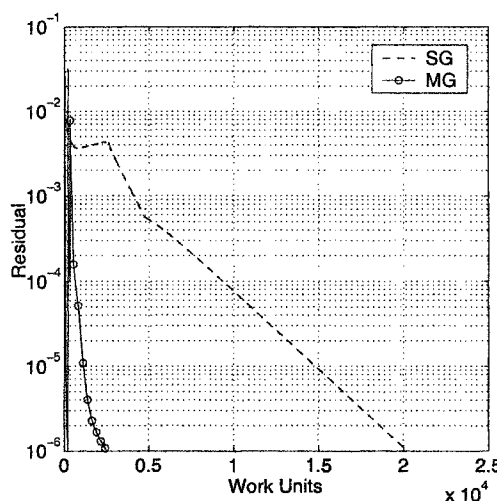


Figure 8.29: Convergence history for potential flow over NACA0012 airfoil ($M_\infty = 0.8, \alpha = 10^\circ$)

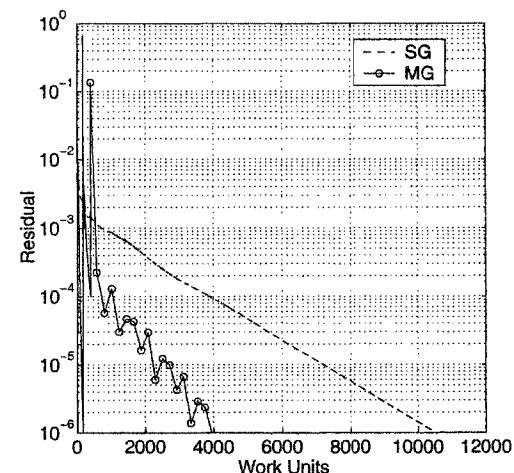


Figure 8.30: Convergence history for viscous flow over NACA0012 airfoil ($M_\infty = 0.8, Re = 500, \alpha = 10^\circ$)

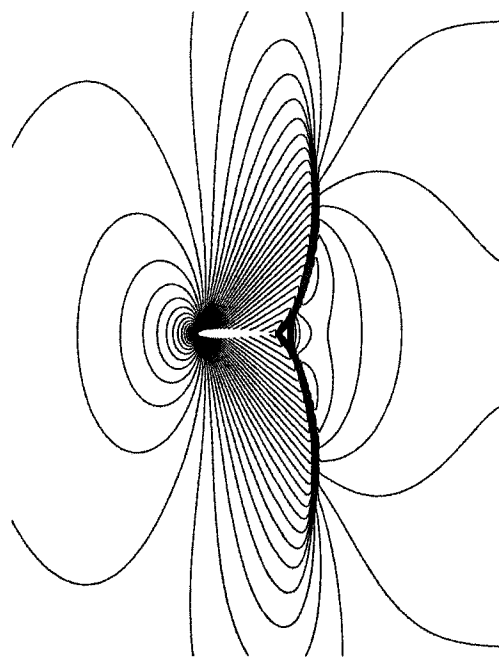


Figure 8.31: Mach contours for potential flow over NACA0012 airfoil ($M_\infty = 0.9$, $\alpha = 0^\circ$)

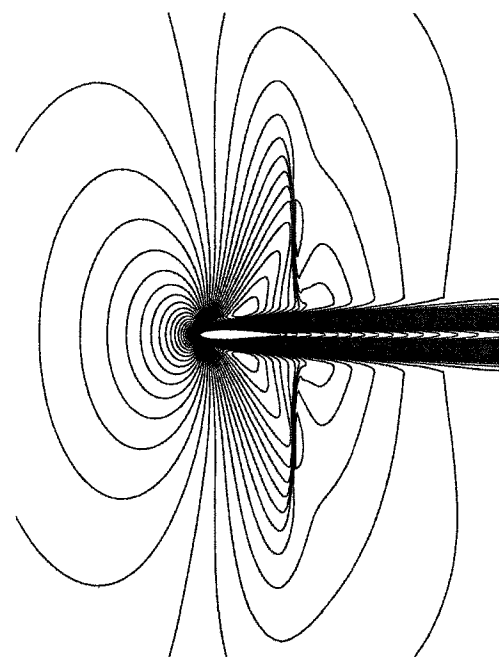


Figure 8.32: Mach contours for viscous flow over NACA0012 airfoil ($M_\infty = 0.9$, $Re = 500$, $\alpha = 0^\circ$)

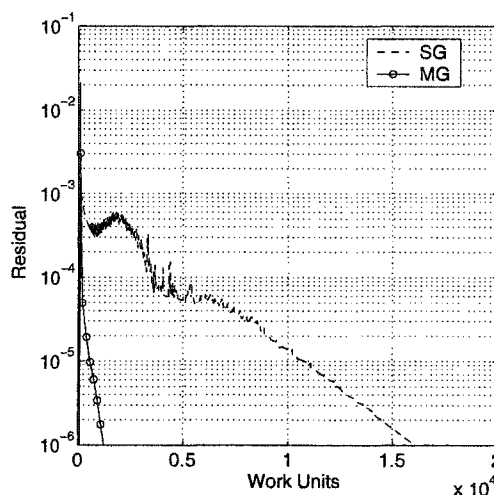


Figure 8.33: Convergence history for potential flow over NACA0012 airfoil ($M_\infty = 0.9$, $\alpha = 0^\circ$)

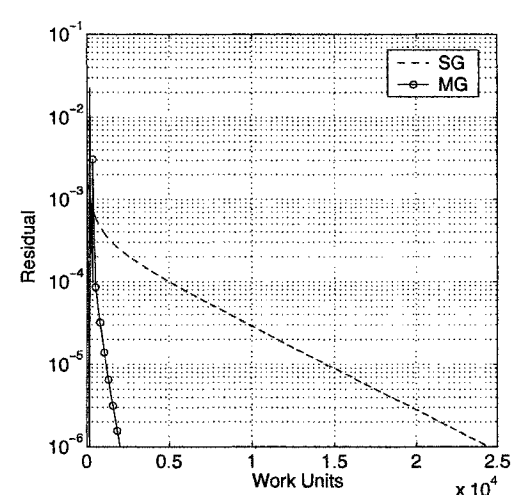


Figure 8.34: Convergence history for viscous flow over NACA0012 airfoil ($M_\infty = 0.9$, $Re = 500$, $\alpha = 0^\circ$)

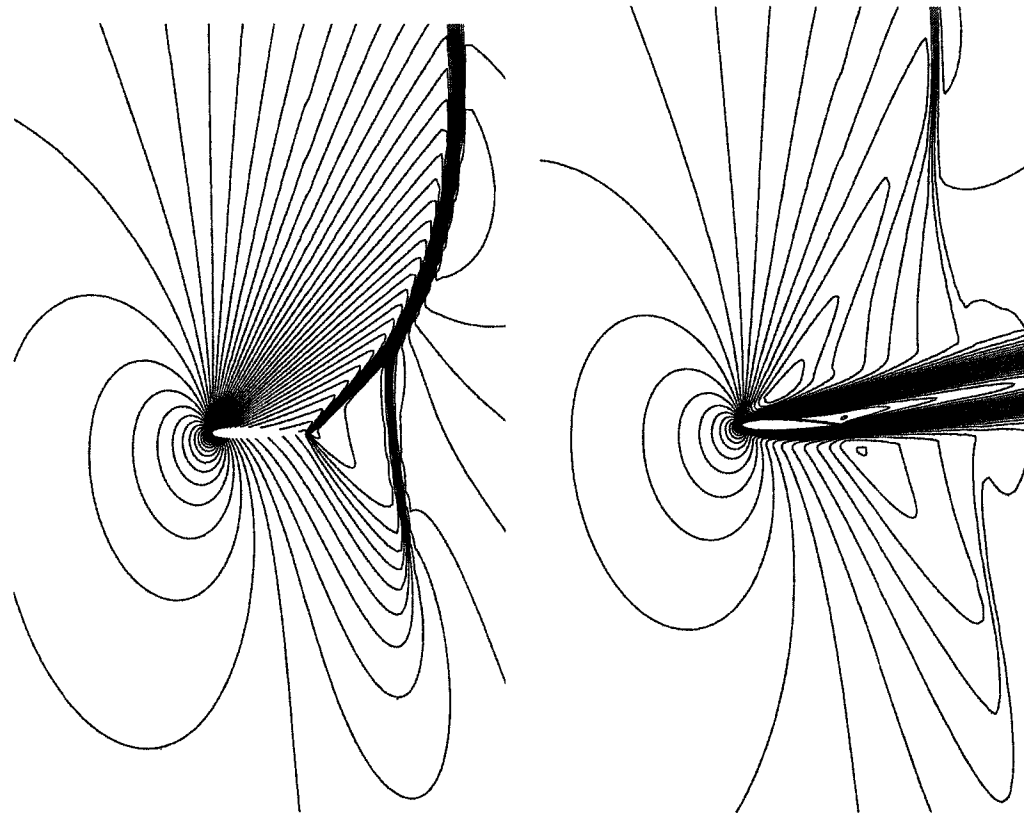


Figure 8.35: Mach contours for potential flow over NACA0012 airfoil ($M_\infty = 0.9$, $\alpha = 10^\circ$)

Figure 8.36: Mach contours for viscous flow over NACA0012 airfoil ($M_\infty = 0.9$, $Re = 500$, $\alpha = 10^\circ$)

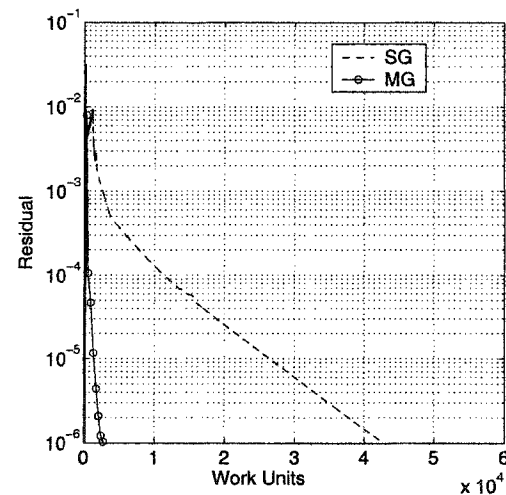


Figure 8.37: Convergence history for potential flow over NACA0012 airfoil ($M_\infty = 0.9$, $\alpha = 10^\circ$)

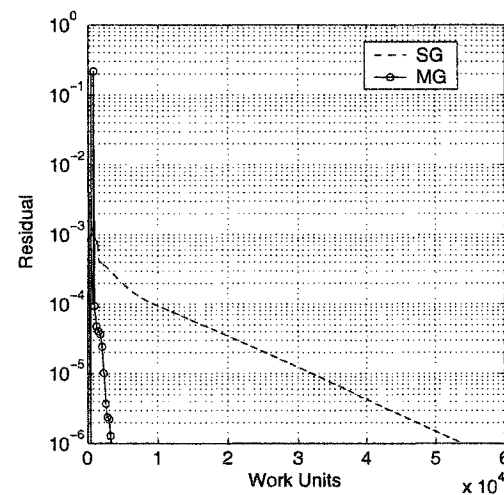


Figure 8.38: Convergence history for viscous flow over NACA0012 airfoil ($M_\infty = 0.9$, $Re = 500$, $\alpha = 10^\circ$)

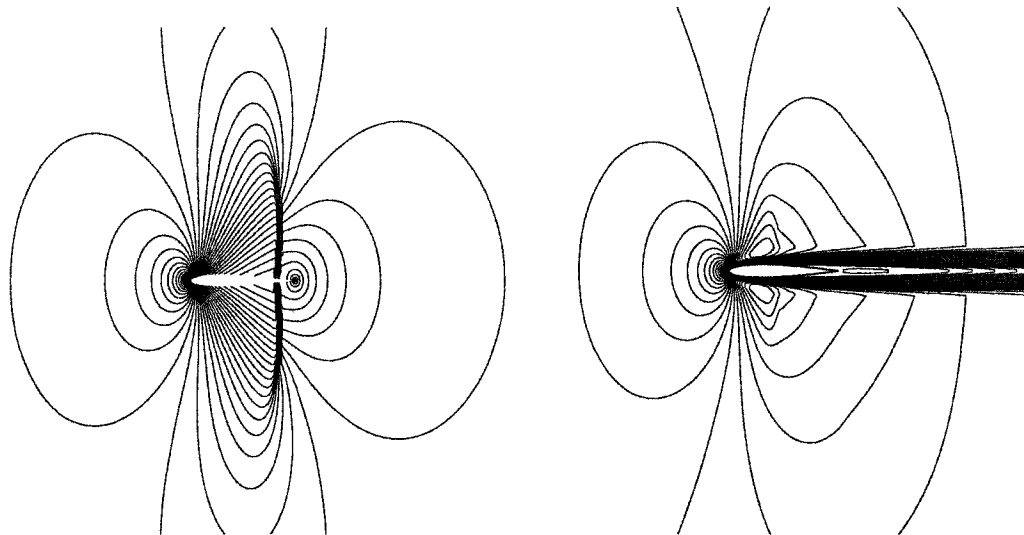


Figure 8.39: Mach contours for potential flow over NACA0012 airfoil
 $(M_\infty = 0.85, \alpha = 0^\circ)$

Figure 8.40: Mach contours for viscous flow over NACA0012 airfoil ($M_\infty = 0.85$,
 $Re = 2000, \alpha = 0^\circ$)

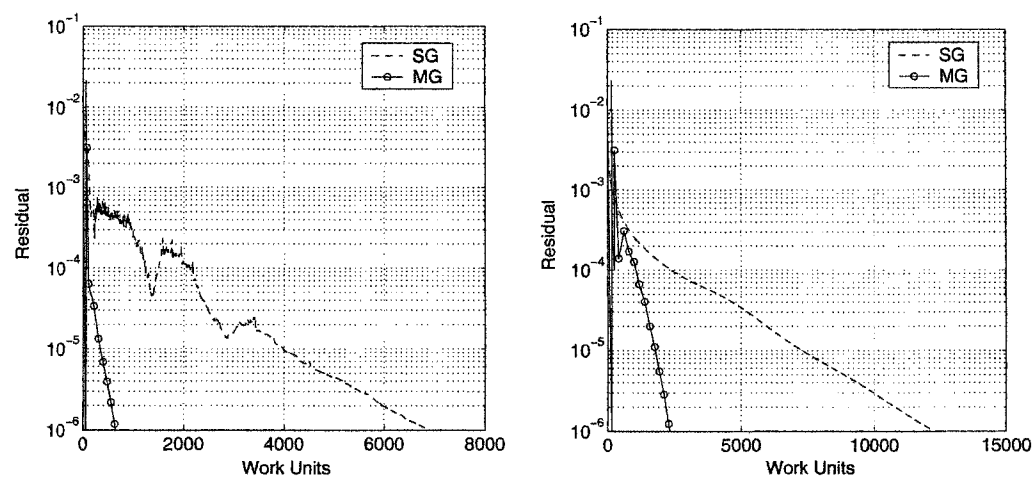


Figure 8.41: Convergence history for potential flow over NACA0012 airfoil
 $(M_\infty = 0.85, \alpha = 0^\circ)$

Figure 8.42: Convergence history for viscous flow over NACA0012 airfoil
 $(M_\infty = 0.85, Re = 2000, \alpha = 0^\circ)$

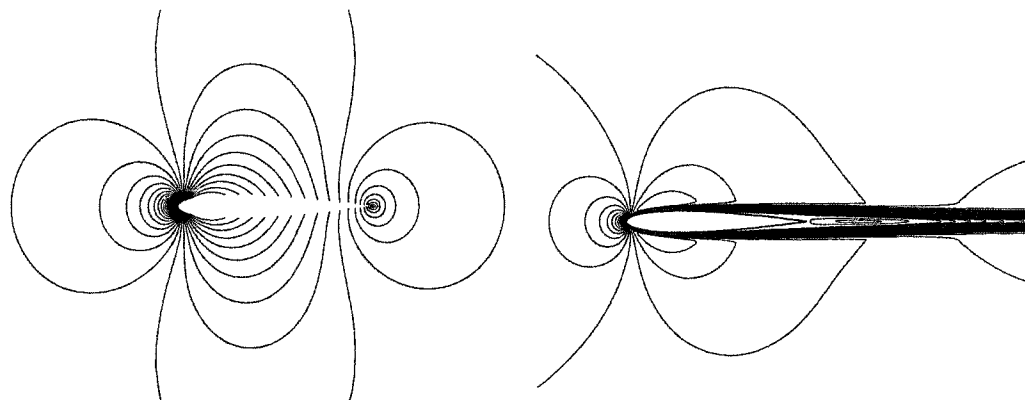


Figure 8.43: Mach contours for potential flow over NACA0012 airfoil ($M_\infty = 0.5, \alpha = 0^\circ$)

Figure 8.44: Mach contours for viscous flow over NACA0012 airfoil ($M_\infty = 0.5, Re = 1 \times 10^4, \alpha = 0^\circ$)

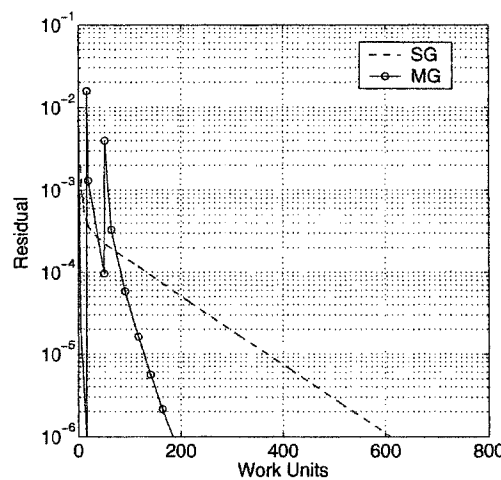


Figure 8.45: Convergence history for potential flow over NACA0012 airfoil ($M_\infty = 0.5, \alpha = 0^\circ$)

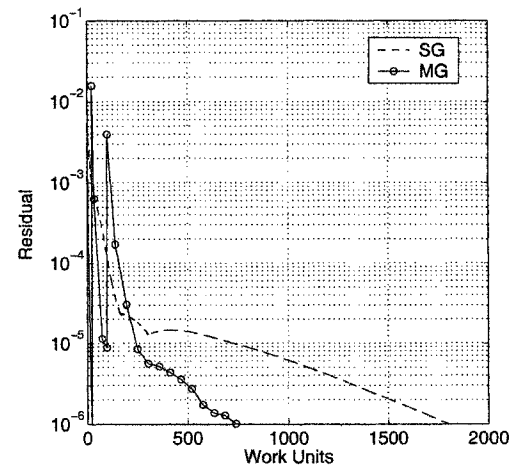


Figure 8.46: Convergence history for viscous flow over NACA0012 airfoil ($M_\infty = 0.5, Re = 1 \times 10^4, \alpha = 0^\circ$)

CHAPTER 9

CONCLUDING REMARKS

9.1 Concluding Remarks

A new formulation was developed for the equations of fluid motion based on a hierarchical approach. The new method was applied to a wide range of inviscid and viscous flow problems and proved to be an efficient and robust method for numerical flow simulations. It also offers several advantages over traditional Euler and Navier-Stokes formulations from the point of view of domain decomposition, multi-grid, upwinding and the incompressible flow limit. These advantages will be discussed briefly in the following sections.

9.1.1 Domain Decomposition

The new formulation allows the flexibility of limiting the evaluation of entropy, vorticity and total enthalpy to relatively small domains in the flow field, whereas the rest of the flow field is governed by a single variable ϕ . This results in savings in CPU time and memory requirements when compared to solving the Navier-Stokes equations everywhere in the flow field, specially in the case of high Reynolds number flows. Also, limiting entropy and vorticity evaluation to small domains results in a

more accurate far field with no artificial entropy and vorticity generation even for highly stretched grids. Furthermore, the introduction of a potential function into the formulation allows a numerically consistent implementation of asymptotic potential flow solutions as far field boundary conditions, which in turn facilitates the use of smaller computational domains without any loss of accuracy in the numerical simulation.

9.1.2 Multigrid

Multigrid methods usually encounter efficiency problems when applied to the Navier-Stokes equations due to the fact that these equations are not purely elliptic, but contain also parabolic/hyperbolic parts. Several attempts have been made to exploit the elliptic and hyperbolic parts of the Navier-Stokes equations to allow for a more efficient implementation of multigrid techniques to flow simulations. The new formulation attempts to exploit the different modes within the Navier-Stokes equations. Based on the new formulation, one can identify two modes. The first mode is an acoustic mode governed by the augmented potential equation. The second mode is represented by the convection/diffusion equations for entropy, vorticity and total enthalpy. Therefore, multigrid can be applied efficiently to the augmented potential equation, while the convergence rates for the convection/diffusion equations are accelerated using local time stepping techniques. Fast convergence rates and an order of magnitude reduction in work units were achieved using this approach which proves to be promising.

9.1.3 Upwinding

Currently, scalar upwind fluctuations splitting schemes have reached a mature stage in their development. The hierarchical formulation allows the efficient use of these multidimensional upwind schemes for the scalar convection/diffusion equations for entropy and total enthalpy. Also, the augmented potential equation doesn't need any upwinding or artificial dissipation in subsonic flow regions, thereby resulting in higher order accuracy in these regions. However, for supersonic regions, upwinding is still required in the augmented potential equation to allow for shock capturing and to maintain numerical stability for supersonic flows.

9.1.4 The Incompressible Flow Limit

Traditional compressible Euler and Navier-Stokes solvers usually suffer from accuracy and slow convergence rate problems when used for the simulation of incompressible and low Mach number flows. However, the new hierarchical formulation was used for the simulation of incompressible flows and no deterioration in accuracy or rate of convergence was observed. This is due to the presence of a built-in preconditioning within the formulation as the Mach number goes to zero, where conservation of mass is enforced through the solution of a Poisson equation for the potential function. Also, since entropy is one of the dependent variables in the new formulation, more accurate control over the problem of spurious entropy generation encountered by current Euler solvers at stagnation points is possible.

9.2 Recommendations for Future Work

Through the present work, the new hierarchical formulation was shown to be an efficient tool for the simulation of aerodynamic flows, with some advantages over traditional Euler and Navier-Stokes formulations. However, there are still some topics that require further investigations. One of these topics is the simulation of turbulent flows. All viscous flow problems considered in the present work were for laminar flows. Future work would include the use of the new formulation to simulate turbulent flows. This could be done by using the Reynolds averaged Navier-Stokes equations with a suitable turbulence model. Also, the extension of the present formulation to the simulation of unsteady flows is needed to allow the modelling of important unsteady phenomena such as vortex shedding. This would require the use of a time-accurate integration method for the unsteady terms in the augmented potential equation and in the convection/diffusion equations of entropy, vorticity and total enthalpy. Another topic to be considered is the implementation of higher order upwind schemes to allow for more efficient numerical simulations. Finally, the extension to complex geometries for practical applications using unstructured grids will be interesting.

BIBLIOGRAPHY

- [1] E.M. Murman and J.D. Cole, *Calculation of Plane Steady Transonic Flows*, AIAA J., Vol. 9, pp. 114-121 ,1971
- [2] E.M. Murman, *Analysis of Embedded Shock Waves Calculated by Relaxation Methods*, AIAA J., Vol. 12, pp. 626-633 ,1974
- [3] B. Enquist and S. Osher, *Stable and Entropy Satisfying Approximations for Transonic Flow Calculations*, Math. Comput., Vol. 34, pp. 45-75 ,1980
- [4] A. Jameson, *Transonic Potential Flow Calculation Using Conservation Form*, Second AIAA CFD Conference, pp. 148-155, 1975
- [5] A. Jameson and D.A. Caughey, *A Finite Volume Method for Transonic Potential Flow Calculations*, Third AIAA CFD Conference, pp. 35-54, 1977
- [6] D.A. Caughey and A. Jameson, *Numerical Calculation of Transonic Potential Flow around Wing-Body Combinations*, AIAA J., Vol. 17, pp. 175-181, 1979
- [7] D.A. Caughey and A. Jameson, *Progress in Finite Volume Calculations for Wing-Fuselage Combinations*, AIAA J., Vol. 18, pp. 1281-1308, 1980
- [8] M.M. Hafez, J. South and E. Murman, *Artificial Compressibility Methods for the numerical solution of the full potential equation*, AIAA J., Vol. 17, pp 838-844, 1979
- [9] M.M. Hafez, W. Whitlow and S. Osher, *Improved finite difference schemes for transonic potential calculations*, AIAA J., Vol. 25, No. 11, pp 1456-1462, 1987
- [10] M.M. Hafez and D. Lovell, *Transonic Small Disturbance Calculations Including Entropy Corrections*, Num. Phys. Aspects Aerodyn. Flows II, Springer, 1981
- [11] M.M. Hafez and D. Lovell, *Entropy and Vorticity Corrections for Transonic Flows*, AIAA paper 83-1926, 1983
- [12] C. Hirsch, *Numerical Computation of Internal and External Flows*, Vols. 1 & 2, John Wiley, 1990
- [13] T. Holst, *Transonic Flow Computations Using Nonlinear Potential Methods*, Progress in Aerospace Sciences, Vol. 36, pp. 1-61, 2000

- [14] R.M. Beam and R.F. Warming, *An Implicit Finite Difference Algorithm for Hyperbolic Systems in Conservation Law Form*, J. Comput. Phys., Vol. 22, pp. 87-110, 1976
- [15] R.W. MacCormack, *A Numerical Method for Solving the Equations of Compressible Viscous Flow*, AIAA paper 81-0110, 1981
- [16] A. Lerat, *Implicit Methods of Second Order Accuracy for the Euler Equations*, AIAA paper 83-1925, 1983
- [17] Y. Saad and M.H. Schultz, *GMRES; A Generalized Minimum Residual Algorithm for Solving Nonsymmetric Linear Systems*, SIAM J. Sci. Stat. Comput., Vol. 7, pp. 856-869 ,1986
- [18] H.O. Kreiss, *On Difference Approximations of the Dissipative Type for Hyperbolic Differential Equations*, Commun. Pure Appl. Math., Vol. 17, pp. 335-353, 1964
- [19] A. Jameson, W. Schmidt and E. Turkel, *Numerical Solutions of the Euler Equations by Finite Volume Methods using Runge-Kutta Time-Stepping Schemes*, AIAA Paper 81-1259, 1981
- [20] J.L. Steger and R.F. Warming, *Flux Vector Splitting of the Inviscid Gas Dynamic Equations with Application to Finite Difference Methods*, NASA TM D-78605, 1979
- [21] B. van Leer, *Flux Vector Splitting for the Euler Equations*, Proceedings of the 8th International Conference on Numerical Methods in Fluid Dynamics, Lect. Notes Phys., Vol. 170, Springer Verlag, pp. 507-512, 1982
- [22] S.K. Godunov, *A Difference Scheme for Numerical Computation of Discontinuous Solution of Hydrodynamic Equations*, Math. Sb., Vol. 47, pp. 271-306, 1959, in Russian, translated U.S. Joint Publications Research Service, JPRS 7226, 1969
- [23] B. van Leer, *Towards the Ultimate Conservative Difference Scheme, V: A Second Order Sequel to Godunov's Method*, J. Comput. Phys., Vol. 32, pp. 101-136, 1979
- [24] P.L. Roe, *The Use of the Riemann Problem in Finite Difference Schemes*, Lect. Notes Phys., Vol. 141, Springer Verlag, pp. 354-359, 1980
- [25] S. Osher and F. Solomon, *Upwind Difference Schemes for Hyperbolic Systems of Conservation Laws*, Math. Comp., Vol. 38, pp. 339-374 ,1982
- [26] A. Harten, *High Resolution Schemes for Hyperbolic Conservation Laws*, J. Comput. Phys., Vol. 49, pp. 357-385, 1983
- [27] A. Deconick and B. Koren, *Euler and Navier Stokes Solver Using Multi-Dimensional Upwind Schemes and Multigrid Acceleration*, Notes on Numerical Fluid Mechanics, Vol. 57, Vieweg, 1997

- [28] T.J.R. Hughes and T.E. Tezduyar, *Finite Element Methods for First-order Hyperbolic Systems with particular emphasis on the Compressible Euler Equations*, Comp. Methods in Appl. Mech. Eng. , Vol. 45, pp. 217-284, 1984
- [29] O. Pironneau, *Finite Element Methods for Fluids*, Wiley, 1989
- [30] R. Lohner, *Applied CFD Techniques*, Wiley, 2001
- [31] P.D. Lax and B. Wendroff, *Systems of Conservation Laws*, Commun. Pure Appl. Math., Vol. 13, pp. 217-237, 1960
- [32] R.W. MacCormack, *The Effect of Viscosity in Hypervelocity Impact Cratering*, AIAA paper 69-354, 1969
- [33] R.W. MacCormack and G.V. Candler, *The Solution of the Navier-Stokes Equations using Gauss-Seidel Line Relaxation*, Comput. Fluids, Vol. 17, pp. 135-150, 1989
- [34] R.M. Beam and R.F. Warming, *An Implicit Factored Scheme for the Compressible Navier-Stokes Equations*, AIAA J., Vol. 16, pp. 393-401, 1978
- [35] B. van Leer, J.L. Thomas, P.L. Roe and R.W. Newsome, *A Comparison of Numerical Flux Formulas for the Euler and Navier-Stokes Equations*, AIAA Paper 87-1104-CP, Honolulu, Hawaii, 1987
- [36] F.T. Johnson, E.N. Tinco and N.J. Yu, *Thirty Years of Development and Application of CFD at Boeing Commercial Airplanes*, Seattle, AIAA Paper 03-3439, 2003
- [37] P.L. Roe and M. Rad, *A form of the Euler equation conserving potential flow*, AIAA Paper 99-3280, 1999
- [38] E. Turkel, *Preconditioned Methods for Solving the Incompressible and Low-Speed Compressible Equations*, J. Comput. Phys., Vol. 72, pp. 277-298, 1987
- [39] B. van Leer, W.T. Lee, and P.L. Roe, *Characteristic Time Stepping or Local Preconditioning of the Euler Equations*, AIAA paper 91-1552, 1991
- [40] D.L. Darmofal and P.J. Schmid, *The Importance of Eigenvectors for Local Preconditioners of the Euler Equations*, J. Comput. Phys., Vol. 127, pp. 346-362, 1996
- [41] H. Schlichting, *Boundary Layer Theory*, McGraw-Hill, 1971
- [42] M.J. Lighthill, *On Displacement Thickness*, J. Fluid Mech., Vol. 4, pp. 383-392, 1958
- [43] S. Goldstein, *On Laminar Boundary Layer Flow Near a Position of Separation*, Quart. J. Mech. Appl. Math., Vol. 1, pp. 43-69, 1948

- [44] D. Catherall and K.W. Mangler, *The Integration of the Two-Dimensional Laminar Boundary-Layer Equations Past the Point of Vanishing Skin Friction*, J. Fluid Mech., Vol. 26 pp. 163-182, 1966
- [45] J.E. Carter and S.F. Wornom, *Solutions for Incompressible Separated Boundary Layers Including Viscous-Inviscid Interaction*, In: Aerodynamic Analysis Requiring Advanced Computers. NASA SP-347 pp. 125-150, 1975
- [46] J.C. LeBalleur, *Viscous-Inviscid Flow Matching: Analysis of problem including Separation and Shock Waves*, La Recherche Aerospatiale, pp. 349-358, 1977
- [47] J.C. LeBalleur, *Viscous-Inviscid Flow Matching: Numerical Method and Applications to 2-Dimensional Transonic and Supersonic Flows*, La Recherche Aerospatiale, pp. 65-76, 1978
- [48] J.E. Carter, *Viscous-Inviscid Interaction Analysis of Transonic Turbulent Separated Flow*, AIAA paper 81-1241, 1981
- [49] A. Veldman, *New Quasi-Simultaneous Method to calculate Interacting Boundary Layers*, AIAA J., Vol. 19, pp. 79-85, 1981
- [50] A. Veldman, J. Lindhout, E. Boer and M. Somers, *Vistrafs: a Simulation Method for Strongly Interacting Viscous Transonic Flow*, Num. and Phys. Aspects of Aerodyn. Flows IV, pp. 37-51, 1990
- [51] W. Van Dalsen and J. Steger, *The Fortified Navier-Stokes Approach*, Proceedings of the Workshop held by the Institute of Nonlinear Sciences at the University of California, Davis, 1986
- [52] J. Flores, T. Holst, U. Kaynak, K. Gunky and S. Thomas, *Transonic Navier-Stokes Wing Solution Using a Zonal Approach: Part I. Solution Methodology and Code Validation*, Technical Report, NASA TM-88248, 1986
- [53] J. Flores, *Applications of the Navier-Stokes Equations to Wings and Complex Configurations using a Zonal Approach*, NASA TM-100080, 1988
- [54] J. Flores and N. Chaderjian, *Zonal Navier-Stokes Methodology for Flow Simulations about Complete Aircraft*, J. Aircraft, 27(7):583-90, 1990
- [55] L.N. Sankar, B.K. Bharadvaj and F. Tsung, *Three Dimensional Navier-Stokes/Full Potential Coupled Analysis for Viscous Transonic Flow*, AIAA Journal, Vol. 31, No. 10, pp. 1857-1862, 1993
- [56] O.A.D. Mello and L.N. Sankar, *Computation of Unsteady Transonic Flow over a Fighter Wing using a Zonal Navier-Stokes/Full Potential Method*, Int. J. Numer. Meth. Fluids, Vol. 29, pp. 575-585, 1999

- [57] M. Paraschivoiu, X. Cai, M. Sarkis, D. P. Young and D. Keyes, *Multi-Domain Multi-Model Formulation for Compressible Flows: Conservative Interface Coupling and Parallel Implicit Solvers for 3D Unstructured Meshes*, AIAA Paper 99-0784, 1999
- [58] A. Quarteroni and A. Valli, *Domain decomposition methods for partial differential equations*, Oxford Science Publications, 1999
- [59] P.D. Lax, *Weak Solutions of Non-Linear Hyperbolic Equations and their Numerical Computation*, Commun. Pure Appl. Math., Vol. 7, pp 159-193, 1954
- [60] R.E. Gordnier and S.G. Rubin, *Transonic Flow Solutions using a Composite Velocity Procedure for Potential, Euler and RNS Equations*, Comput. Fluids, Vol. 17, pp 85-98, 1989
- [61] M.M. Hafez and W.H. Guo, *Wake Capturing in Potential Flow Calculations*, Acta Mechanica, Vol. 143, pp 47-56, 2000
- [62] A.J. Chorin, *A Numerical Method for Solving Incompressible Viscous Flow Problems*, J. Comput. Phys., Vol. 2, pp 12-26, 1967
- [63] F.H. Harlow and J.E. Welch, *Numerical Calculation of Time Dependent Viscous Incompressible Flow of Fluid with Free Surface*, Phys. of Fluids, Vol. 8, pp 2182-2189, 1965
- [64] J.C. Tannehill, D.A. Anderson and R.H. Pletcher, *Computational Fluid Mechanics and Heat Transfer*, second edition, Taylor and Francis, 1997
- [65] P.D. Lax, *Hyperbolic Systems of Conservation Laws and the Mathematical Theory of Shock Waves*, Philadelphia: SIAM Publications, 1973
- [66] H. Ashley and M. Landahl, *Aerodynamics of Wings and Bodies*, Dover Publications, 1985
- [67] S. Goldstein, *Concerning Some Solutions of the Boundary Layer Equations in Hydrodynamics*, Proc. Camb. Phil. Soc., vol 26, pp 1-30, 1930
- [68] K. Stewartson, *On the Flow Near the Trailing Edge of a Flat Plate*, Mathematika, vol 16, pp 106-121, 1969
- [69] A.F. Messiter, *Boundary Layer Flow Near the Trailing Edge of a Flat Plate*, SIAM J. Appl. Math., vol 18, pp 241-257, 1970
- [70] A.E.P. Veldman, *Matched Asymptotic Expansions and the Numerical Treatment of Viscous-Inviscid Interaction*, J. Engr. Math., vol 39, pp 189-206, 2001
- [71] S.G. Rubin and D.R. Reddy, *Analysis of Global Pressure Relaxation for Flows with Strong Interaction and Separation*, Comput. Fluids, vol 11, pp 281-306, 1983

- [72] R.T. Davis and M.J. Werle, *Progress on Interacting Boundary-Layer Computations at High Reynolds Number*, Numer. Phys. Aspects of Aerodyn. Flows, Springer, 1981
- [73] A.E.P. Veldman and A.I. van de Vooren, *Drag of a Finite Flat Plate*, 4th Intl. Conf. Numer. Methods Fluid Dyn., pp 423-430, 1974
- [74] D.R. Chapman, D.M. Kuehn and H.K. Larson, *Investigation of Separated Flows in Supersonic and Subsonic Streams with Emphasis on the Effect of Transition*, NACA Rep. 1356, 1958
- [75] R.J. Hakkinen, I. Greber, L. Trilling and S.S. Abarbanel, *The Interaction of an Oblique Shock Wave with a Laminar Boundary Layer*, NASA Memo 2-18-59W, 1959
- [76] R.W. MacCormack, *Numerical Solution of the Interaction of a Shock Wave with a Laminar Boundary Layer*, Proc. Second Intl. Conf. on Num. Methods in Fluid Dyn, Springer Verlag, pp 151-163, 1970
- [77] J.R. Amaladas and H. Kamath, *Accuracy Assessment of Upwind Algorithms for Steady-State Computations*, Comput. Fluids, vol 27, pp 941-962, 1998
- [78] M.M. Zdravkovich, *Flow around Circular Cylinders*, Vols. I & II ,Oxford Univ. Press, 2003
- [79] M. van Dyke, *An Album of Fluid Motion*, Parabolic Press, Stanford, 1982
- [80] O. Rodriguez, *The Circular Cylinder in Subsonic and Transonic Flow*, AIAA J. vol 22, pp 1713-1718, 1984
- [81] I. Imai, *Approximation Methods in Compressible Fluid Dynamics*, University of Maryland, Institute for Fluid Dynamics and Applied Mathematics, 1957
- [82] M. van Dyke, *Perturbation Methods in Fluid Dynamics*, Parabolic Press, Stanford, 1975
- [83] N. Botta, *The Inviscid Transonic Flow about a cylinder*, J. of Fluid Mechanics vol 301, pp 225-250, 1995
- [84] M. Pandolfi and F. Larocca, *Transonic Flow about a circular cylinder*, Computers and Fluids vol 17, pp 205-220, 1989
- [85] M. D. Salas, *Recent developments in transonic Euler flow over a circular cylinder*, Mathematics and Computers in Simulation (25), 1983
- [86] M.M. Hafez and A. Dimanlig, *Simulations of Compressible Inviscid flows over stationary and rotating cylinders*, Acta Mechanica, pp 241-249, 1994

- [87] M.M. Hafez and A. Dimanlig, *Some anomalies of the numerical solution of the Euler equations*, Acta Mechanica, vol 119, pp 231-139, 1996
- [88] M.M. Hafez, *Non-Uniqueness Problems in Transonic Flows*, CFD Journal, vol 11, pp 371-376, 2002
- [89] G.K. Batchelor, *An Introduction to Fluid Dynamics*, Cambridge University Press, 1967
- [90] P.K. Kundu, *Fluid Mechanics*, Academic Press, 1990
- [91] V.J. Modi, *Moving Surface Boundary-Layer Control: A Review*, J. Fluids Struct., Vol. 11, pp 627-663, 1997
- [92] S. Mittal, *Control of Flow Past Bluff Bodies Using Rotating Control Cylinders*, J. Fluids Struct., Vol. 15, pp 291-326, 2001
- [93] L.E. Fraenkel, *On corner eddies in plane inviscid shear flow*, J. of Fluid Mechanics, Vol. 11, pp 400-406, 1961
- [94] H. Liepmann and A. Roshko, *Elements of Gas Dynamics*, John Wiley, 1957
- [95] M.M. Hafez and E.M. Wahba, *Inviscid Flows over a Cylinder*, Comput. Methods Appl. Mech. Eng., vol 193, pp 1981-1995, 2004
- [96] J.L. Thomas and M.D. Salas, *Far-Field Boundary Conditions for Transonic Lifting Solutions to the Euler Equations*, AIAA J., vol 24, pp 1074-1080, 1986
- [97] D. Stojkovic, M. Breuer and F. Durst, *Effect of High Rotation Rates on the Laminar Flow around a Circular Cylinder*, Phys of Fluids, vol 14, pp 3160-3178, 2002
- [98] S. Mittal and B. Kumar, *Flow Past a Rotating Cylinder*, J. Fluid Mech., vol 476, pp 303-334, 2003
- [99] M.B. Glauert, *The Flow Past a Rapidly Rotating Circular Cylinder*, Proc. R. Lond. Soc. A, vol 242, pp 108-115, 1957
- [100] M.M. El-Refaee, *Boundary Layer Control of Separated Flow over Circular Cylinders - A BEM Parametric Study*, Engineering Analysis with Boundary elements, vol 14, pp 239-254, 1994
- [101] Y. Delaunay and L. Kaitksis, *Control of Circular Cylinder Wakes using Base Mass Transpiration*, Phys of Fluids, vol 13, pp 3285-3302, 2001
- [102] E.V. Buldakov, S.I. Chernyshenko and A.I. Ruban, *On the Uniqueness of Steady Flow past a Rotating Cylinder with Suction*, J. Fluid Mech., vol 411, pp 213-232, 2000

- [103] M.M. Hafez and W.H. Guo, *Simulation of Steady Compressible Flows Based on Cauchy/Riemann Equations and Crocco's Relation*, Int. J. Numer Meth Fluids, Vol. 27, pp 127-138, 1998
- [104] C. Tang and M.M. Hafez, *Numerical Simulation of Steady Compressible Flows using a Zonal Formulation. Part I: Inviscid Flows*, Comp. and Fluids, Vol. 30, pp 989-1001, 2001
- [105] M.M. Hafez and W.H. Guo, *Simulation of Steady Compressible Flows Based on Cauchy/Riemann Equations and Crocco's Relation, Part II: Viscous flows*, Int. J. Numer Meth Fluids, Vol. 31, pp 325-343, 1999
- [106] NASA Ames Research Center, *Overflow User's Manual*, 1995
- [107] L. Cambier, *Computation of Viscous Transonic Flows using an Unsteady Type Method and a Zonal Grid Refinement Technique*, in Numerical Simulation of Compressible Navier-Stokes Flows: GAMM Workshop, M.O. Bristeau, R. Glowinski, J. Periaux and H. Viviand (Eds.), pp 105-122, Vieweg, 1987
- [108] D. Kinney and M.M. Hafez, *Finite Element Simulation of Compressible Viscous Flows over Lifting Airfoils*, AIAA paper 92-0669, 1992
- [109] V. Schmitt and F. Charpin, *Pressure Distributions on the ONERA-M6 Wing at Transonic Mach Numbers*, Experimental Data Base for Computer Program Assessment, Report of the Fluid Dynamics Panel Working Group 04, AGARD AR 138, 1979
- [110] C. Tang and M.M. Hafez, *Numerical Simulation of Steady Compressible Flows using a Zonal Formulation. Part II: Viscous Flows*, Comp. and Fluids, Vol. 30, pp 1003-1016, 2001
- [111] M.M. Hafez and J.C. South, *Vectorization of Relaxation Methods for Solving Transonic Full Potential Equation*, in Numerical Methods for the Computation of Inviscid Transonic Flows with Shock Waves, GAMM Workshop, 1979
- [112] M.M. Hafez and D. Lovell, *Improved Relaxation Schemes for Transonic Potential Calculations*, AIAA Paper 83-0372, 1983
- [113] R.P. Fedorenko, *A Relaxation Method for Solving Elliptic Equations*, USSR Comput. Math. Math. Phys., Vol. 1, pp. 1092-1096, 1962
- [114] R.P. Fedorenko, *The Speed of Convergence of an Iterative Process*, USSR Comput. Math. Math. Phys., Vol. 4, pp. 227-235, 1964
- [115] A. Brandt, *Multigrid Techniques: 1984 Guide with Applications to Fluid Dynamics*, GMD-Studie, vol. 85. GMD-FIT, 1985

- [116] J.L. Thomas, B. Diskin and A. Brandt, *Textbook Multigrid Efficiency for Fluid Simulations*, Annu. Rev. Fluid Mech. Vol. 35, pp 317-340, 2003
- [117] D.A. Caughey and A. Jameson, *Fast Preconditioned Multigrid Solution of the Euler and Navier-Stokes equations for steady compressible flows*, Int. J. Numer. Meth. Fluids vol. 43, pp 537-553, 2003
- [118] A. Brandt, *Multi-Level Adaptive Solutions to Boundary Value Problems*, Math. Comput., vol. 31, pp 333-390, 1977
- [119] W.A. Mulder, *A New Multigrid Approach to Convection Problems*, J. Comput. Phys., vol. 83, pp 303-323, 1989
- [120] A. Jameson, *Acceleration of Transonic Potential Flow Calculations on Arbitrary Meshes by the Multiple Grid Method*, AIAA Paper 79-1458, 1979
- [121] D. Drikakis, O. Iliev and D. Vassileva, *On Multigrid Methods for the Compressible Navier-Stokes Equations*, ICLSSC 2001, Springer-Verlag, pp 344-352, 2001

VITA

Essam M. Wahba**Degrees:**

B.Sc. in Mechanical Engineering, Alexandria University, Egypt (1997)

M.Sc. in Mechanical Engineering, Alexandria University, Egypt (2000)

Special Honors and Awards:

1. Dean of Engineering Award: for ranking first over Mechanical Engineering Department, Alexandria University, Egypt (1994,1995,1996,1997)

2. Joseph L. Steger Award: for graduate achievements in CFD, University of California, Davis (2003)

3. Essam A. Salem Award: for best M.Sc. thesis in Fluid Mechanics, Alexandria University, Egypt (2004)

Academic Experience:

1. Teaching Assistant, Alexandria University, Egypt (1997-2000)

2. Assistant Lecturer, Alexandria University, Egypt (2000-present)

3. Research Assistant, University of California, Davis (2001-present)

Publications:

1. H.A. Warda, H.A. Kandil, A.A. Elmiligui and E.M. Wahba, *Modeling Pressure Transients in Viscoelastic Pipes*, PVP-Vol 431, Emerging Technologies for Fluids, Structures and Fluid-Structure Interaction, pp 305-323, ASME 2001

2. H.A. Warda, H.A. Kandil, A.A. Elmiligui and E.M. Wahba, *Modeling unsteady friction in rapid transient pipe flows*, Alexandria Engineering Journal, Vol 40, pp 783-795, 2001

3. H.A. Warda, H.A. Kandil, A.A. Elmiligui and E.M. Wahba, *Modeling Pressure Transients in Viscoelastic Pipes*, Alexandria Engineering Journal, Vol 40, pp 797-809, 2001

4. H.A. Warda, H.A. Kandil, A.A. Elmiligui and E.M. Wahba, *Column Separation with the effect of Air Release in Viscoelastic Pipes*, Alexandria Engineering Journal, Vol 41, pp 189-203, 2002
5. M.M. Hafez and E.M. Wahba, *Numerical Simulations of Sonic Booms in Non-uniform Flows*, Proceedings of Second International Conference on Computational Fluid Dynamics (ICCFD2), Australia 2002
6. M.M. Hafez and E.M. Wahba, *Hierarchical Formulations for Transonic Flow Simulations*, Proceedings for Symposium Transsonicum IV, Germany 2002, also appeared in Computational Fluid Dynamics Journal, vol.11 no.4, pp 377-382, 2003
7. M.M. Hafez and E.M. Wahba, *Inviscid Flows over a Cylinder*, Computer Methods in Applied Mechanics and Engineering, vol.193, pp 1981-1995, 2004
8. M.M. Hafez and E.M. Wahba, *Numerical Simulations of Transonic Aerodynamic Flows based on a Hierarchical Formulation*, AIAA Paper 03-3564, 2003, also to appear in International Journal for Numerical Methods in Fluids
9. M.M. Hafez and E.M. Wahba, *Multigrid Acceleration of Transonic Aerodynamic Flow Simulations based on a Hierarchical Formulation*, Proceedings of Third International Conference on Computational Fluid Dynamics (ICCFD3), Toronto, Canada 2004, also to appear in International Journal for Numerical Methods in Fluids
10. M.M. Hafez, A. Shatalov and E.M. Wahba, *Numerical Simulations of Incompressible Aerodynamic Flows using Viscous/Inviscid Interaction Procedures*, To appear in Computer Methods in Applied Mechanics and Engineering
11. M.M. Hafez and E.M. Wahba, *Viscous/Inviscid Interaction Procedures for Compressible Aerodynamic Flow Simulations*, To appear in Computers and Fluids
12. M.M. Hafez and E.M. Wahba, *Incompressible Viscous Steady Flows over Finite Flat Plate and Rotating Cylinder with Suction*, to appear in Computational Fluid Dynamics Journal